Time-resolved measurements of collective effects in quantum conductors

Everton Arrighi

Université Grenoble Alpes

THÈSE

Pour obtenir le grade de

DOCTEUR DE L'UNIVERSITÉ GRENOBLE ALPES

Spécialité : **Nanophysique**

Arrêté ministériel : 25 mai 2016

Présentée par

Everton Arrighi

Thèse dirigée par **Christopher Bäuerle**

préparée au sein **Laboratoire Institut Néel - CNRS**
et de **l'École doctorale de Physique**

Time-resolved measurements of collective effects in quantum conductors

Thèse soutenue publiquement le **7 février 2020**,
devant le jury composé de :

Gwendal Fève
Professeur, LPENS, Sorbonne Université, Rapporteur

Masaya Kataoka
Principal Research scientist, National Physical Laboratory, Rapporteur

Anne Anthore
Maîtresse de conférence, C2N-CNRS, Université Paris Diderot, Examinatrice

Serge Florens
Directeurs de recherche, Institut Néel-CNRS, Communauté Université Grenoble Alpes, Président

Xavier Waintal
Directeur de recherche, IRIG-CEA Grenoble, Examinateur

Christopher Bäuerle
Directeur de recherche, Institut Néel-CNRS, Communauté Université Grenoble Alpes, Directeur de thèse

Abstract

Quantum dynamics is very sensitive to dimensionality. While two-dimensional electronic systems form Fermi liquids, one-dimensional systems – Tomonaga–Luttinger liquids – are described by purely bosonic excitations, even though they are initially made of fermions. With the advent of coherent single-electron sources, the quantum dynamics of such a liquid is now accessible at the single-electron level.

In this PhD work, we study the most general case where the system can be tuned continuously from a clean one-channel Tomonaga–Luttinger liquid to a multi-channel Fermi liquid in a non-chiral system. We use time-resolved measurement techniques to determine the time of flight of a single-electron voltage pulse and extract the collective charge excitation velocity. Analysing the propagation velocity allows to reveal the collective effects that govern the physics in our quasi one-dimensional system. Our detailed modelling of the electrostatics of the sample allows us to construct and understand the excitations of the system in a parameter-free theory. We show that our self-consistent calculations capture well the results of the measurements, validating the construction of the bosonic collective modes from the fermionic degrees of freedom.

The presented time control of single-electron pulses at the picosecond level will also be important for the implementation of waveguide architectures for flying qubits using single electrons. Integrating a leviton source into a waveguide interferometer would allow to realise single-electron flying qubit architectures similar to those employed in linear quantum optics. Furthermore, our studies pave the way for studying real-time dynamics of a quantum nanoelectronic device such as the measurement of the time spreading or the charge fractionalisation dynamics of the electron wave packet during propagation.

Contents

CHAPTER 1

Introduction

The beginning of the 20th century was a prosperous period when it comes to progress in science, inventions and technology. However, many of the ideas were not believed to be possible at the end of the previous century. An example is a famous statement from Lord Kelvin: "Heavier-than-air flying machines are impossible" [1] in 1895. One year later, he said: "I have not the smallest molecule of faith in aerial navigation other than ballooning" [1]. Despite the lack of faith from Lord Kelvin, the Brazilian Albert Santos-Dumont realized the first public demonstration of a powered, heavier-than-air aircraft in 1906 at the Bagatelle field [2] [1]. More than a hundred years later, there are not as many balloons as aeroplanes in the sky.

Lord Kelvin shared his "optimism" also about physics. In 1900, he stated "There is nothing new to be discovered in physics now. All that remains is more and more precise measurements" [1]. The one who had a similar opinion was Philipp Von Jolly, a physicist and mathematician, professor at the University of Munich. He advised one of his students not to go into physics, saying: "In this field, almost everything is already discovered, and all the remains is to fill a few unimportant holes" [4]. This quote dates from 1878 and it ends up as a big destiny's irony because the student that he had advised was Max Planck, whose work is at the origin of the field of quantum theory.

In 1901, to solve the ultraviolet catastrophe problem [5], Planck considered that the black-body radiation is emitted in discrete energy packets named quanta, recovering the corpuscular theory of light proposed by Newton. Further studies have followed Planck's approach, such as the study from Albert Einstein explaining the photoelectric effect in 1905, for which he got the Nobel Prize in 1921.

Proper treatment of the quantization of the light came in 1927, with a seminal work from Paul Dirac of the quantum theory of radiation [6]. Roy J. Glauber, Leonard Madel and George Sudarshan have made use of the quantum theory to the electromagnetic field in the '50s and '60s, achieving a better understanding of the statistics of light [7]. They have created several important concepts such as coherent states. It was predicted that quantum states of light with features different from classical states, such as squeezed light.

1 The flight of the 14-Bis (Dumont's aeroplane) was the first aviation activity to be homologated by the Fédération aéronautique internationale (FAI), with self-propelled take-off. Years later, it was recognized by the FAI that the Wright brothers had accomplished this feat in 1905. The FAI recognizes the first flight happened in 1903. However, the Wright brothers' aeroplane did not have a self-propelled take-off at the time. It might be that the french Clément Ader achieved the self-propelled take-off in 1890, at the south-west of Paris. Nevertheless, the only witnesses were his employees [3].

This field that deals with the phenomena that cannot be understood by considering light as an electromagnetic wave is called quantum optics. The light is treated as a stream of photons (quanta of light).

1.1 Quantum optics

A milestone in quantum optics happened in 1956, with the work of Hanbury Brown and Twiss [8]. Their experiment consisted in measuring the correlation in the light intensities received by two detectors, of a light source split by a half-silvered mirror. They have observed positive correlation between the light beams, and their scheme become a famous experiment to test the statistics of particles. Furthermore, the confirmation of non-classical properties of light was given by Kimble, Dagenais and Mandel measuring the photon anti-bunching [9]. This work developed the first single-photon source.

Quantum optics was also useful in clarifying the mysteries of quantum mechanics. A work from Einstein, Podolsky and Rosen raised the possibility that quantum mechanics was not complete [10], and it was proposed the existence of local hidden-variables to explain the behaviour of entanglement. Based on correlations, Bell derived an inequality that could bring to a conclusion about the existence of local-variables [11]. In 1981, with the help of quantum optics, the violation of Bell's inequality was measured for the first time [12], discarding the possibility of hidden-local variables in quantum mechanics.

The subject of quantum optics has become a vast field and is now related to subjects that go from quantum information processing to the study of light-matter interactions [13]. Despite all the famous effects of quantum mechanics unveiled with quantum optics experiments, as photons are bosons, it is very difficult to make them interact.

Electrons, which are fermions, are strongly interacting particles due to the existing Coulomb interaction. One could also think to probe the statistics of electrons, with the experiments realised with photons. The possibility to create single electrons on-demand and to investigate such physics with electrons instead of photons opened up an entirely new field often referred to as *electron quantum optics*.

1.2 Electron quantum optics

Recent advances in nanofabrication and measurement techniques have made it possible to be able to control and manipulate single electrons. These advances allowed envisioning quantum-optics-like experiments with single electrons. This field is still in its infancy, even though a few pioneering experiments have been realised over the last decade. With faster and faster time control of the electron wave packet, such an approach should also allow to use single electrons to implement flying qubit architectures.

In this section, we will describe the building blocks needed to perform the electron counterpart of quantum optics. First, we describe the basics of high mobility two-dimensional electron gases (2DEG) based on a GaAs/AlGaAs heterostructure, which are the workhorse of our studies and we review very briefly the main discoveries which have been made with such systems.

Then we review some recent advances in the field of electronic quantum-optics. In particular, we discuss the different single-electron sources that have been developed, giving

particular emphasis to the Leviton source. In the last part, we review the different methods used to characterise the propagation velocity of electrons in semiconductors.

1.3 Two-Dimensional electron gas

To investigate electronics properties, we use AlGaAs/GaAs heterostructures. These two semiconductors have different energy band gaps (energy separation between the valence band and conduction band). Donors are introduced on the AlGaAs layer, which is represented in figure 1.1**a** as n-AlGaAs. The electrons diffuse from the n-AlGaAs to the lower energy GaAs layer, leaving positively charged donors at the n-AlGaAs which is balanced by the electrons confined at the heterointercace. Due to the electrostatic potential generated, the band bends as shown in figure 1.1**b** and a triangular well is formed. The electron energies are increased due to the small space where the electrons are confined, around 8 nm [14]. Thus discrete quantum-electric subbands are formed. At low temperatures, only the first level (subband) is occupied, since the gap energy between the first and the second level (subband) is on the order of 300 K [15–17]. The dopant layer is put at a relatively far distance (40 nm) from the interface of AlGaAs, to avoid any scattering between the donors with electrons in the 2DEG, which helps to achieve high mobility. The density of electrons for the 2DEG used in our experiments is $n_s = 2.11 \times 10^{-11}\,\mathrm{cm}^{-2}$ and the mobility is of $\mu = 1.89 \times 10^{6}\,\mathrm{cm}^{2}\mathrm{V}^{-1}\mathrm{s}^{-1}$, measured in dark and at 4.2 K. The high-mobility heterostructures used during my thesis were grown by molecular beam epitaxy, allowing to reach very clean and stable structures. They were provided by our collaborator Prof. Andreas Wieck from the University of Bochum.

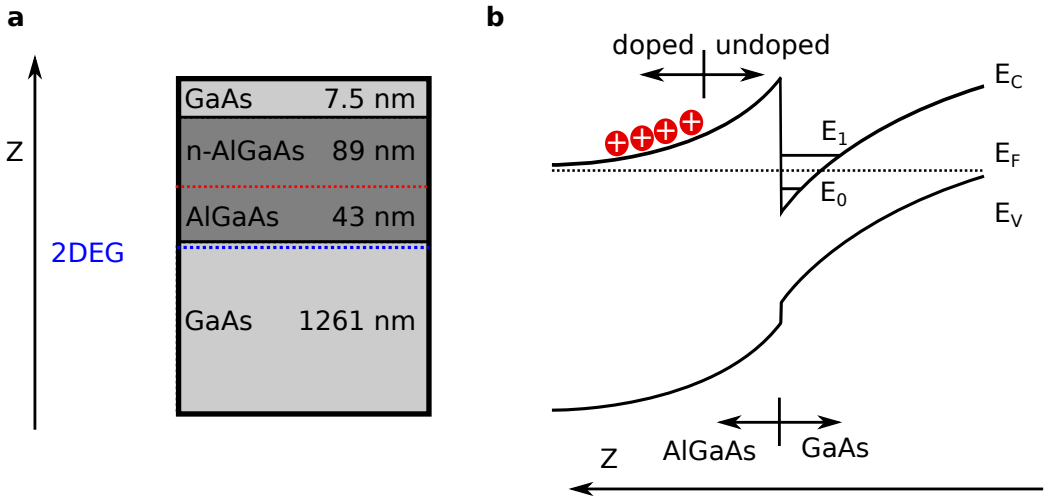

Figure 1.1: 2DEG and band structure. a, Vertical cut of the AlGaAs/GaAs heterostructure used in this thesis. **b,** Qualitative drawing of the energy of valance band and conduction band along the vertical growth direction. A triangular quantum well is formed at the interface between AlGaAs and GaAs. Figure adapted from [17] and [14].

From the density of the high-mobility heterostructure and the mobility of the material,

we can estimate the mean free path from [18]:

$$L_m = \frac{\hbar\mu}{\mid e \mid}\sqrt{2\pi n_s} \approx 14\,\mu\text{m} \tag{1.1}$$

Another relevant length scale is the coherence length l_ϕ. It corresponds to the length over which the phase of the electron wave function stays well defined. At low temperature this length is typically of the order of a few tens µm [19–21]. More recently this length-scale has been pushed to more than 100 µm [22] by careful engineering of the quantum device. Thanks to sophisticated nanofabrication techniques we can engineer quantum interferometers by gate patterning of the heterostructure that are smaller than the coherence length in the 2DEG.

Using electron beam lithography it is possible to create the desired quantum circuit. This can be done by depositing metallic gates on the surface of the heterostructure. There is a Schottky barrier at the metal-semiconductor interface, which allows to apply a negative voltage to the metallic gates without having current flowing to the 2DEG. In fact, this negative voltage will deplete the electrons underneath the surface gate, that means we can design and engineer a quantum circuit by simply changing the shape of the gates on the top of the sample. With present state-of-the-art equipment, we can fabricate gates in the order of tens of nanometers. To perform transport measurements, we add ohmic contacts to the 2DEG, such that we can apply a voltage and collect the current going through.

1.4 Quantization of conductance

Mesoscopic physics is the domain that lies between the microscopic and the macroscopic world. With the invention of the two-dimensional electron gas [23], we have a convenient tool to investigate the behaviour of electrons in the mesoscopic regime. One pioneering experiment in this field was the discovery of the quantization of the conductance. The first measurements of this effect were done by B.J. van Wees et al. in Delft [24] and almost at the same time by Wharam et al. [25] at the University of Cambridge. To observe quantized conductance one deposits two metallic Schottky gates in a split geometry (see inset of Figure 1.2) and applies a bias voltage to the Ohmic contact in order to pass a current going through the 2DEG. Increasing the negative voltage on these two gates, it is possible to deplete more and more the electrons underneath, arriving at a situation where the width of the slit is on the same order as the Fermi wavelength. This results in the occurrence of plateaus of conductance as a function of the applied gate voltage, as shown in figure 1.2.

The constriction created by the two gates on the 2DEG makes that the electron wave functions form 1D subbands. Ideally, the total conductance depends only on the number of available channels in the QPC region. By treating each subband as an independent 1D system, the density of states is simply the sum of the density of states for each subband [26]. The conductance for a one-dimensional ballistic system under an applied bias can be derived by calculating the current flow, which is proportional to the density of states times the velocity. For one-dimensional system, the density of states times the velocity gives a constant, which implies that the conductance is quantized and equal to $2e^2/h$ [26, 27], when the spin degeneracy is not lifted. Spin degeneracy can be lifted by applying a

magnetic field [25].

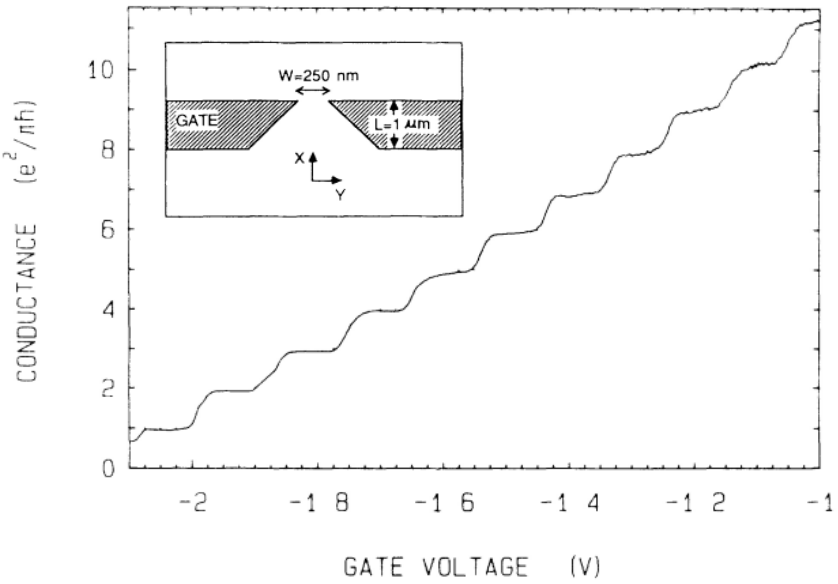

Figure 1.2: Quantization of conductance. The conductance of the Quantum point contact versus the applied gate voltage. One observes plateaus of conductance with multiples of $2.e^2/h$. Figure adapted from [24].

The design of the Schottky gates shown in the inset of the figure 1.2 is known as a quantum point contact (QPC), and we will describe several applications using this gate structure. One of these applications is to build a beam splitter since we can set the transmission simply by changing the gate voltages applied to the Schottky gates. Thus we can set the values to one plateau of conductance (full transmission of one channel of conductance) or half of this value (one channel being transmitted with 50% of probability).

Implementing such beam splitters allowed the realization of different quantum interferometers, such as the Young's double-slit [28], Mach-Zehnder [29, 30] or Hong-Ou-Mandel interferometer [31] with electrons.

1.5 Quantum Hall effect

Another breakthrough experiment in the field of mesoscopic physics has been the observation of the Quantum Hall Effect (QHE) by V. Klitzing, Dorda and Pepper in 1980 [32]. Measuring the Hall voltage of a two-dimensional electron gas at liquid helium temperatures and under a high magnetic field, they were the first to measure the quantisation in the Hall resistance.

To explain this effect semi-classically, we can think that by applying a very high magnetic field, the electrons in the bulk start to follow a circular motion due to the Lorentz force, and they form closed trajectories, which is known as cyclotron motion. Thus the electrons in the bulk do not participate to the transport. However, the electrons close to the edges are forced on skipping orbits and only the edge will contribute to the transport. The chirality imposed by the magnetic field makes the electrons that are propagating in opposite edges

travel in opposed direction.

By changing the magnetic field, one can achieve a situation where there are quantised levels of conductance flowing along the edge of the sample and contributing actively to the transport. The number of these edge channels is usually related to the filling factor ν. It can take integer values, and one usually refers to the integer quantum Hall effect (IQHE) while for very high purity samples, fractional numbers can be attained, known as the fractional quantum Hall effect [33]. Here we will not go in further details of the QHE, because all the experiments of my thesis were taken at zero magnetic field. For further details, we address the reader to the following references [18, 34].

The edge channels have the remarkable property that backscattering is strongly suppressed [35] due to the chirality of the system. This makes it possible to reach a long coherence length of several tens of µm [19–21] and it has been shown that with a smart design it is possible to keep the coherence for more than 200 µm [22].

1.5.1 Electronic Mach-Zehnder interferometer

We described so far how to build an electronic beam splitter and how one can make the electrons propagate along edge channels.

Let us now discuss some experiments made with these tools. The optical Mach-Zehnder interferometer (MZI) is the device that first allowed to demonstrate the phase shift between two optical beams, due to the change in the path length of one of the beams. In figure 1.3 **a**, we show a schematic drawing of the optical interferometer. S stands for the optical source, and then the beam is split in two at beam splitter 1 (BS1). The beams propagate in separated paths, and are recombined in beam splitter BS2. They are then collected at the detector D1 and D2. D1 measures maximum (zero) signal and D2 measures zero (maximum) signal depending whether the phase difference is 0 (π) between the two beams. The sum of the measured signals is equal to the input signal if there is no loss on propagation.

The first Mach-Zehnder interferometer that used as a guide for the electrons an edge channel and as beam splitters QPCs, has been realized by the Weizmann team in 2003 [29]. In figure 1.3, we can see the schematic of the experiment, where a magnetic field is applied such that there is only one edge channel ($\nu = 1$).

Similar to the optical counterpart, we have conservation of the current injected in the source leading to $I_S = I_{D1} + I_{D2}$. Considering the probabilities of transmission and reflection on the QPC as $|r_i|^2 + |t_i|^2 = 1$, and considering the phase difference between the two interfering path as φ, the current is then given by $I_{D1} \propto T_{D1} = |t_1.t_2|^2 + |r_1.r_2|^2 + 2\,|t_1.t_2.r_1.r_2|\cos(\varphi)$.

To modify the relative phase φ between the two different paths, one can explore the Aharonov-Bohm effect, which is a spectacular and fundamental phenomenon of quantum mechanics. The electrons will pick a phase corresponding to the magnetic flux going through the area formed by the two different paths. This originates from the coupling between the vector potential and the complex phase in the wavefunction of the electrons. Thus, by varying the magnetic field, one can control the phase difference between the electrons in the different arms, as displayed in figure 1.3 **c**. The phase difference between the electrons passing through the two branches induced by the AB effect is equal to:

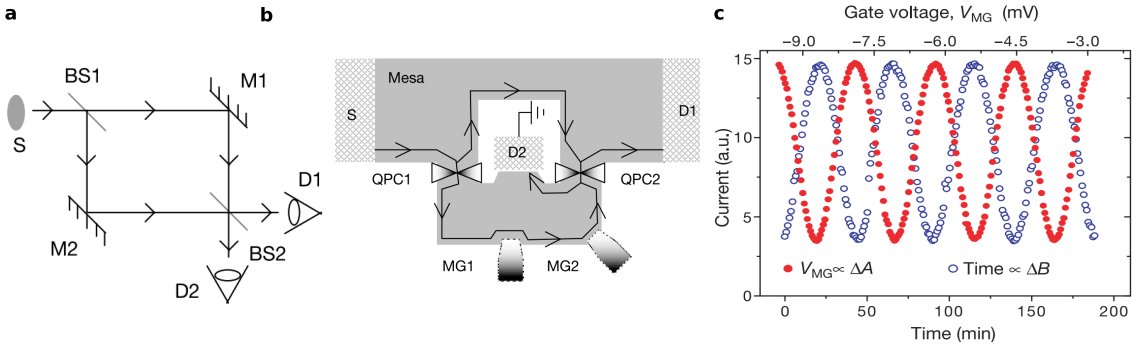

Figure 1.3: Optical MZI interferometer and the electronic analogue. a, Schematic of an optical Mach-Zehnder interferometer, where S is the source, BS1 and BS2 are the beam-splitters, M1 and M2 are mirrors, and D1 and D2 are detectors. **b,** The electronic version of the MZI, where S in an ohmic contact, to inject current into the 2DEG, the QPCs act as beam splitters, the edge channel works as the waveguide for the electrons, MG1 and MG2 are two Schottky gates that can be used as phase shifters, D1 and D2 are also ohmic contacts, the first placed there to collect current and the second is connected to the ground, to avoid that electron scattered at the second beam splitter interact with electrons entering in the interferometer. **c,** Plot of the current measured in D1, varying the phase φ between the different paths in two different ways: with the magnetic field (AB effect) or with the Schottky gate. Figure adapted from [29].

$$\Delta\varphi = \frac{eBA}{\hbar} \tag{1.2}$$

Where e is the elementary charge, B is the magnetic field, and A is the area enclosed by the two different arms. It is also possible to control the phase by altering the electron path. This can be done by applying a negative gate voltage to one of the surface gates MG1 and MG2. This will induce an increase of the length of the electron path of the lower interferometer branch, as depicted in figure 1.3**b** by MG1 and MG2.

In reference [29], the authors have controlled the phase between the two arms using the gate and the magnetic field, as presented in figure 1.3**c**. One observes similar current oscillations for both types of control. From the oscillation amplitude, one can determine the visibility which is defined as $\nu = \frac{I_{max}-I_{min}}{I_{max}+I_{min}}$. From measuring its dependence on different parameters (temperature, interferometer size, bias etc.) one can quantify the coherence length of the system. For the case of reference [29], with an electronic temperature of 20 mK they have obtained a visibility of 60%. They observed a decrease in visibility when they increased the bias. The same effect is detected with temperature. A direct way to determine the coherence length is by changing the size of the interferometer. This has been done in reference [19] and a coherence length of $l_\varphi \sim 20\,\mu$m at 20 mK has been obtained.

1.6 Flying qubits

The ultimate goal of our research is to realize electronic flying qubits using single-electron wave packets. This requires efficient single-electron sources, quantum interferometers to manipulate the quantum state of the propagating electron and a single-electron detector.

Besides building a flying qubit, it is essential to understand first the propagation of a single-electron wave packet, and this has been the central part of this PhD work.

The flying qubit has some intrinsic advantages over static qubits in its architecture. First, we can create entangled states on the flight and separate them afterwards, thus with this architecture, the transferring of entangled states from different places appears naturally. Second, ideally one would be able to decouple the hardware with the number of qubits, being able to create qubits on-demand, without the need to add new devices. For this purpose, we could follow the proposal described in [36] where they consider a loop structure, where one could insert flying excitations on-demand, and apply quantum gates at will, as shown in figure 1.4. This architecture is a theorist view for the moment, however, the goal in our research group is to develop each of the elementary bricks of this machine and to explore how far one can go to realise such a flying-qubit architecture with single-electron wave packets.

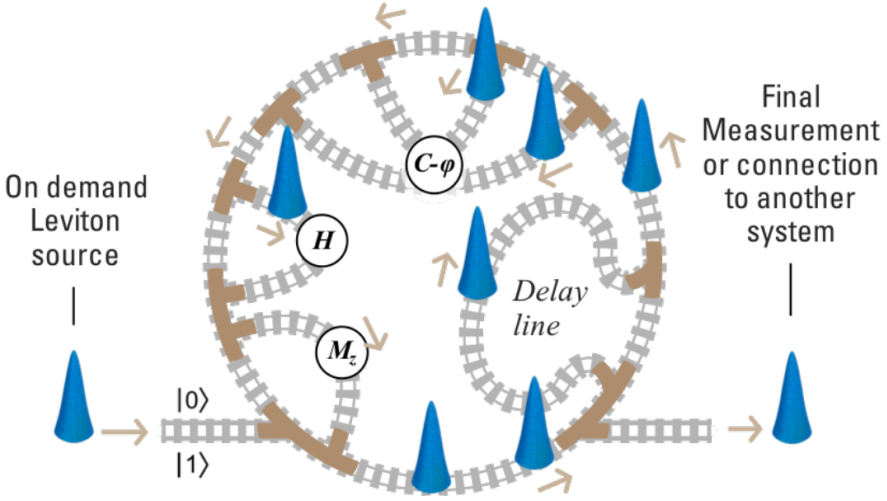

Figure 1.4: Hypothetical architecture of a flying qubit. From left to right: A single electron wave packet (Leviton), enters the loop. Upon propagation the desired quantum gates are applied. After performing the quantum operation the final state can be either measured or transferred to another system. Figure taken from ref [36].

To realise such a flying qubit architecture requires several ingredients such as single-electron sources, the ability to perform quantum manipulations in flight as well as single-electron detection. These issues will be discussed in the following by highlighting the progress which has been done over the last ten years.

1.7 Single electron sources

In the following, we will briefly review the present state of the art of single-electron sources which are compatible with electron quantum optics experiments. Initially, single-electron sources have been developed to realise a current standard. The first single-electron sources were developed at the beginning of the '90s using individual tunnel junctions [37]. Although for metrology purpose, the source should emit a current in the order of several hundreds of

pA [38], to reach the precision needed. For further information about the development of single-electron sources with different materials and structures, we address the reader to the review [38].

Since we have mentioned the use of electron sources for metrological purposes, it is worth noting that the redefinition of the SI base units occurred in 2019. The electron charge is now a defining constant. The definition of ampere has also changed, where before the ampere standard was based on finding the current to have a certain electric force (2×10^{-7} N/m) between two parallel wires of infinite length placed at a fixed distance (1 m) in vacuum [39]. The old definition was problematic because the ampere could not be realized by its definition considering infinity wires in vacuum are generally not available. .

The new definition of ampere is calculated by dividing the charge of an elementary charge (defining constant) by one second. In this case, the ampere is calculated only with the defining constants or base units, the second, which is defined based on the ground-state hyperfine transition frequency of the caesium 133 atom [39].

1.7.1 Controlled emission of single-electron in a dynamic quantum dot

This single-electron source is an electron pump structure, developed for metrology purpose. It consists of a dynamic quantum dot (QD), that is formed by parallel electrostatic gates deposited at the surface of a heterostructure (AlGaAs/GaAs). In the original version [40], multiple gate structures have been used. In an optimized version [41, 42], it consists of two parallel gates with an opening between the two gates, where the electrons are trapped. Only one gate is swept to load and eject electrons as shown in figure 1.5.

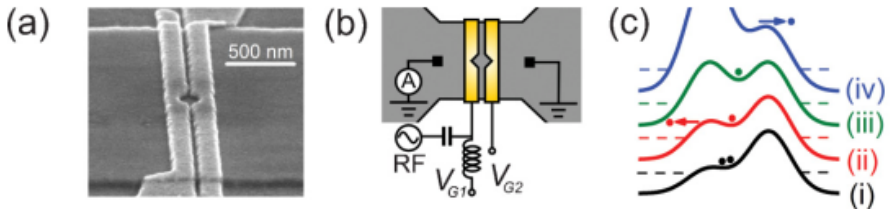

Figure 1.5: Non-adiabatic single electron pump. **a,** Scanning electron microscope (SEM) image of the device. The parallel Schottky gates are in light-grey. The empty circle between the gates is where the electrons are trapped. **b,** Schematic of electrical connections. The left gate is swept in order to load electrons and expel them from the quantum dot. The electrons are loaded from the left side and sent to the right side. **c,** Potential in the quantum dot due to the electrostatic gates. (i) load position, (ii) back-tunnelling to leave just one electron in the dot, (iii) single-electron trapped, (iv) ejection of a single-electron. Figure reproduced from [42].

This single-electron source works as follows. The right gate voltage is fixed to the emission energy, typically around 100 meV [43], well above the Fermi energy. Electrons are then loaded into the quantum dot by lowering the electrostatic potential of the left gate (i). Then, the potential of the left gate is raised, removing all the extra electrons - they tunnel back to reservoir on the left side (ii). The potential on the left gate is further increased, isolating few electrons from the Fermi sea. This process can be adjusted to isolate a single-electron (iii). Once the potential on the left gate is raised above the one of the right gate, an electron is emitted form the source (iv). These experiments are generally

performed with a high magnetic field, working in the quantum hall regime, to make the electrons propagate on the edge, minimizing scattering process.

The current generated with the pump is equal to $I_P = nef$. Considering that a single electron is emitted, the current is proportional to the electron charge times the repetition frequency which the electron is emitted. By engineering the voltage pulse applied in the left gate, it is possible to increase the frequency up to 1 GHz, generate a current up to 150 pA and at the same time having a high experimentally accuracy (better than 1.2 parts per million) [41]. Even better accuracy has been achieve in recent works [44, 45] (lower than 1 p.p.m.).

One way to study transport in this system is to add another barrier and do a energy-resolved detection. The energy spectroscopy indicates that with a high magnetic field the emitted electrons can propagate over several microns with small inelastic electron-phonon scattering [43, 46]. Another interesting point is the use of this energy barrier as a gate to partition electrons one by one [47].

1.7.2 An on-demand coherent single-electron source

The first coherent single-electron source has been realised by the ENS group [48]. It was originally designed to demonstrate the quantum capacitance theoretically proposed in reference [49] The principle is shown in figure 1.6, and the system is operated under a strong magnetic field in order to work in the quantum Hall regime with no spin degeneracy. The idea is to realize a time-controlled single-electron source, which emits electrons suitable for coherent manipulation, having a specific quantum state. The source is made from one quantum-dot defined by one electrostatic gate, used to define the capacitive coupling to the dot and one QPC (2 gates), used to set the tunnel coupling to the conductor.

It is possible to control the levels of the quantum dot, by polarising the gate that is capacitively coupled to it. If one applies a gate voltage such that one energy level filled with 1 electrons lies above the Fermi level, this electron is expected to escape from the dot with an average time of $\tau = h/(D.\Delta)$, where Δ is the energy-level spacing of the quantum dot. When one removes the extra voltage applied, the energy level from where the electron has escaped, will be again lower than the Fermi energy, therefore it will be repopulated with one electron from the Fermi sea. That means, that one hole will be injected into the lead.

Since the electron and the hole are separated in time, this is still a viable source to investigate the electron behaviour in a ballistic medium. This source was used afterwards for a Hanbury Brown-Twiss interferometer [50], followed by an electronic analogue of the Hong-Ou-Mandel interferometer [31].

1.7.3 Moving quantum dot as a single-electron source

Another way to build a single-electron source using quantum-dots can be done in the following way: an electron is isolated in a quantum dot and by launching a surface acoustic wave, this electron is dragged away by the generated mechanical surface wave. Hereby one uses the fact that GaAs is a piezoelectric material; in other words, a mechanical wave propagating at the surface of the substrate is accompanied by a moving electric field which carries away the electron.

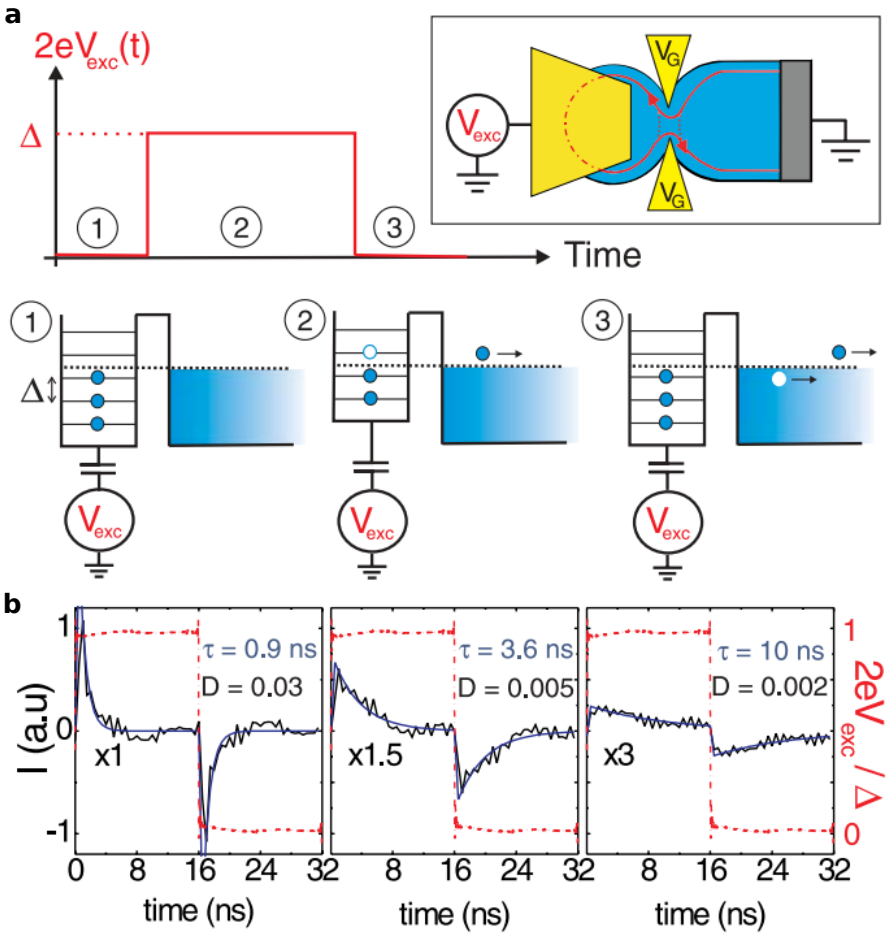

Figure 1.6: The mesoscopic capacitor as a single-electron source. **a,** The single-charge injection is demonstrated. Step 1: the quantum dot is set to a situation where the Fermi energy of the reservoir is between two energy levels of the quantum dot (Coulomb blockade). Step 2: the potential at the dot is increased by Δ, such that one occupied level has energy higher than the Fermi sea. One electron will leave the dot on the escape time τ. Step 3: when the potential at the dot is lowered again, the empty level will be filled with an electron, injecting a hole into the system. **b,** Time-domain measurement, where the red curve corresponds to the applied signal applied at the large gate and the black curve is the average current. The relaxation time is deduced from an exponential fit (blue curves). D corresponds to the transmission, changed with the voltage V_G. Figure reproduced from [48].

To generate a surface acoustic wave, one can use an interdigital transducer (IDT) deposited on top of the substrate. The IDT consist of interleaved metallic fingers and the wavelength of the surface acoustic wave (SAW) can be defined by the distance between the fingers. The velocity of propagation of the SAW is about 3000 m/s [51], that is roughly two orders of magnitude smaller than the Fermi velocity in GaAs. Since the electron propagates with a much smaller velocity, this, in theory, should make it easier to manipulate the

electron in flight, considering the time-of-flight of few ns.

The procedure to realize a single electron emission is the following: The gate voltage V_b of the reservoir gate is lowered to load an electron (see figure 1.7). One then increases the potential on the QD by keeping a single-electron. By setting the tunnelling barrier very high, one can make the electron confined in a QD for a few hundreds of ms [52]. Next, one launches the SAW towards the sample, the potential on the dot can be set in a way that the electron will be picked up and be transported in one of the minima of the SAW. One can use the electrostatic gates to define a depleted channel, where the electron will propagate [53, 54]. The electric potential during the steps of the transfer protocol is exemplified in figure 1.7. An advantage of this approach is that one can detect the single-electron once it is trapped in a QD. The detection of the electron can be done in a single-shot way with a QPC close to the each QD and which is used as an electrometer [55, 56]. The success rate of the transfer of electrons in a recent experiment is well above 99% over a channel of 20 µm [57]. One can also use this quantum dot to prepare a spin state [58] and coherent electron spin transfer has been recently demonstrated in our group [59]. One can also use this platform to engineer flying qubits as presently developed in our group [57].

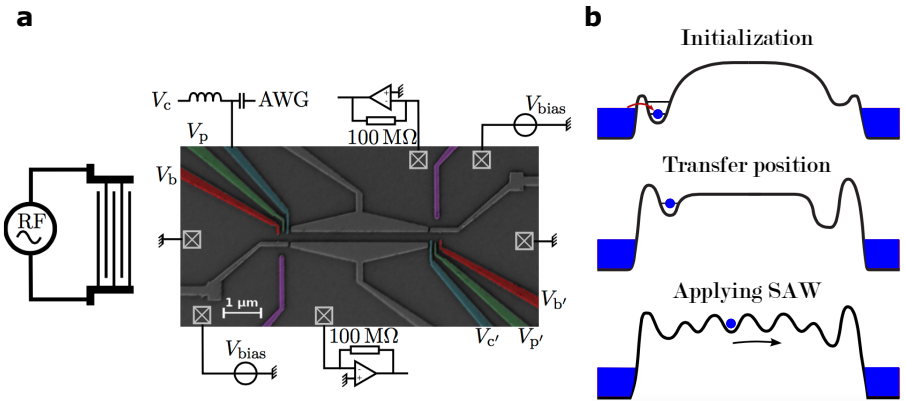

Figure 1.7: Moving quantum dot as a single-electron source. a, SEM image of the sample used as a single-electron transfer device in ref [55]. The two large gates define the 3 µm-long 1D channel. The purple gates are the QPCs used as an electrometer. Applying a microwave burst to the IDT generates the SAW that will pick up the electron from one QD and transports it to the other QD. **b,** Sketch of the electrostatic potential during the steps of the transfer protocol. For the initialization, the potential on the QD is lowered to allow one electron to enter. The potential on the QD is then increased to isolate the dot from the reservoir. The applied SAW catches the electron and transports it to the second QD. The figures are adapted from [55, 60].

1.7.4 Leviton source

The single electron source described in this section is directly related to this PhD work and we will present it in more detail compared to the other single-electron sources we have so far reviewed. The idea is to generate a single electron excitation right at the Fermi sea.

The excitation generated by the mesoscopic capacitor has a defined energy, but it is not well defined in time since it depends on the tunnelling process to leave the capacitor.

In our work we use a different approach, where we apply a voltage pulse directly to the Fermi sea (via the Ohmic contact) creating almost immediately a perturbation on it. If we consider a device containing exactly a single-channel of conductance, the voltage should create a current of $I(t) = (e^2/h)V(t)$, which gives the average charge:

$$\tilde{n} = \int \frac{eV(t)}{h} dt \tag{1.3}$$

One should make the difference between the average number of charges transmitted and the number of quasi-particles excited. For instance, one could have an average current transmitted which corresponds to the transfer a single electron charge, but which is accompanied by several neutral excitations (electron-hole pairs).

Levitov *et al.* [61] proposed a way to minimise the creation of quasi-particles by choosing an optimum shape for the voltage pulse. They also developed an approach [62] to be able to compare the statistics of quasi-particles generated for voltage pulses with different shapes. It turns out that the optimum shape is a Lorentzian pulse, with quantised flux ($\tilde{n}$ of equation 1.3 equals an integer). Another requirement is related to the energy scales. The electronic temperature should be smaller than the energy associated with the duration (time extension) of the pulse and also from the height of the pulse (voltage amplitude) [63–65]. Following Leviton's proposal, the pulse that meets all these conditions become known as the *Leviton*. To test these requirements, one could engineer an interferometer to measure the noise generated for different pulses, frequencies and amplitudes.

A breakthrough in that field happened when Dubois et al.[66] published the first experimental study with Levitons. By sending a Leviton over a ballistic channel, the number of extra excitations can be detected measuring the low-frequency current noise, after the partition of the excitation by a quantum point contact (with transmission smaller than 1). In their experiment, the shortest Lorentzian pulses have widths of 30 ps with a repetition frequency of 6 GHz. In this case, these values are larger in energy in comparison with the electronic temperature, 35 mK. A schematic of this experiment is shown in figure 1.8.

Let us consider the stationary wave function describing the Fermi sea as a plane wave $\Psi(x,t) = e^{ikx-iEt}$ [64]. After we apply a voltage pulse, considering that it is applied very locally, the phase of the Fermi sea will be shifted as follows:

$$\Psi(x,t) = e^{i\phi(t)+ikx-iEt/\hbar} \tag{1.4}$$

where $\phi(t)$ is the extra phase introduced by the voltage pulse and is equal to:

$$\phi(t) = \int_{-\infty}^{t} \frac{eV(u)}{\hbar} du \tag{1.5}$$

If this quantity is not an integer, the final state of the Fermi sea will strongly differ from the initial one, and it will generate a diverging number of electron-hole excitations, below and above the Fermi sea. This result is known as the orthogonality catastrophe, where the number of particle-hole pairs should diverge [61]. If we consider a voltage pulse with a

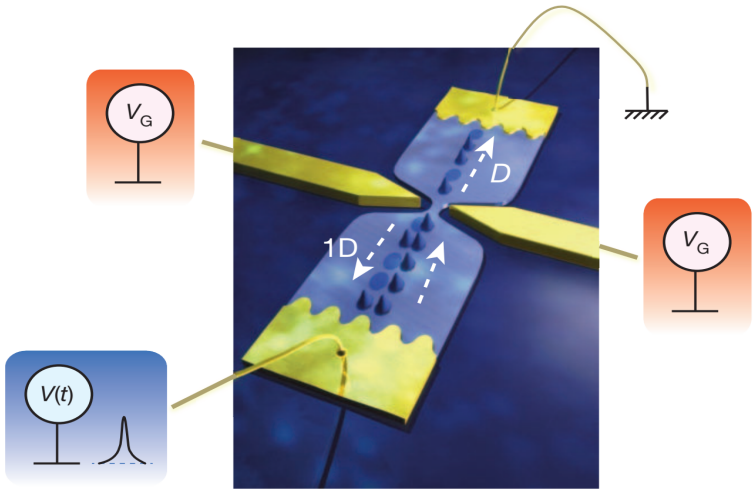

Figure 1.8: Sample design used to measure the low-frequency current noise. Levitons are created at the bottom gold contact and propagate until the QPC where part of the excitation is transmitted (reflected), going to the ohmic contact on the top (bottom). The low-frequency current noise is measured by converting them into voltage fluctuations and by calculating the cross-correlation between the signals. Figure extracted from [66].

Lorentizan shape of width $2w$, the equation would be equal to:

$$eV(t) = \frac{2\hbar w}{w^2 + t^2} \tag{1.6}$$

Due to the variation in time of the voltage pulse, the electrons are scattered in a superposition of states, with different energies. The probability of having an electron with energy ε to have the energy displaced to $\varepsilon + \Delta\varepsilon$ is given by:

$$P(\Delta\varepsilon) = \left| \int_{-\infty}^{\infty} e^{-i\phi(t)} e^{i\Delta\varepsilon t/\hbar} / dt / \sqrt{2\pi\hbar} \right|^2 \tag{1.7}$$

This result is based on the Floquet scattering theory, developed for periodic sources in mesoscopic conductors [67]. The integral of equation 1.7 is solvable for positive and negative values of $\Delta\varepsilon$. However, if we consider a Lorentzian pulse (eq. 1.6), $e^{i\phi(t)} = (t+iw)/(t-iw)$, which has no poles in the lower complex plane, this leads to simply adding probabilities at energies above the Fermi sea. If we consider the case of zero temperature, the number of electrons N_e and holes N_h would be [68]:

$$N_e = \int_0^{\infty} \Delta\varepsilon P(\Delta\varepsilon) d(\Delta\varepsilon) \tag{1.8}$$

$$N_h = \int_{-\infty}^{0} -\Delta\varepsilon P(\Delta\varepsilon) d(\Delta\varepsilon) \tag{1.9}$$

Since equation 1.7 is equal to zero for negative values of $\Delta\varepsilon$, thus $N_h = 0$, minimizing the number of excitations ($N_{\text{excitations}} = N_h + N_e$). One could complain that we are using a theory for periodic pulses and applying it for a single Lorentzian. The generalization of the pulse used here can be made considering a sum of Lorentzian equally spaced in time, as developed in [63, 69]. For this case, the $e^{i\phi}$ will be the product of similar functions to the one written above. Therefore it still has no poles in the lower complex plane, arriving at the same conclusion.

In figure 1.9, we show the effect of a Leviton on the Fermi sea and the associated energy spectrum excited above the Fermi level.

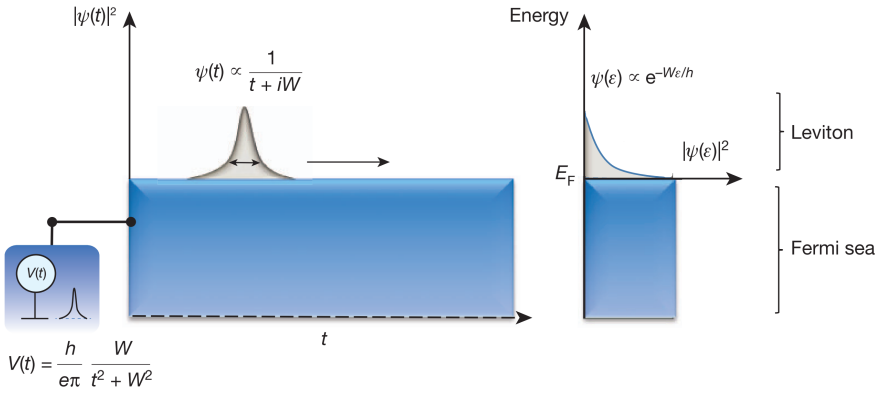

Figure 1.9: Fermi sea and a Leviton excitation. Schematic picture of the Fermi level and the Leviton wavefunction in time domain. **right,** Plot of the Leviton wavefunction in energy space showing the exponential decay due to the Lorentzian pulse shape. Figure adapted from [66].

It has been shown in reference [66] that the partition noise of a Leviton pulse is reduced in comparison to other pulses (sinus or square pulse). The partition noise does not give directly the number of extra quasiparticles (electrons and holes) when working with finite temperatures, due to thermal effects. Another thing that happens when working at finite temperature is that applying a pulse with an integer number of charge does not give the minimum noise, as shown in figure 1.10. The minimum noise is shifted for $q = 1.4$, which is related to the overlapping of the thermal excitations around E_F and the exponential decay in the energy of the Leviton pulse. The effect of temperature on the purity of the Leviton pulse has been investigated recently [70].

This single-electron source is very convenient for the following reasons. The first reason is that the excitation is well defined in the time domain. The second reason is the reduced complexity in nanofabrication, considering that we need only one ohmic contact and not multiple gates as for all the other cases. On the other hand, the propagation velocity should be at least at the Fermi velocity, which increases the difficulty to manipulate the excitation on-the-fly, as we will discuss in the next section. For the electron emitted with a dynamic quantum dot, the emission energy is way above the Fermi energy, and the electron could relax during the propagation, due to electron-phonon interaction [43]. Nevertheless, it is a promising source for metrology studies. The mesoscopic capacitor emits an electron with

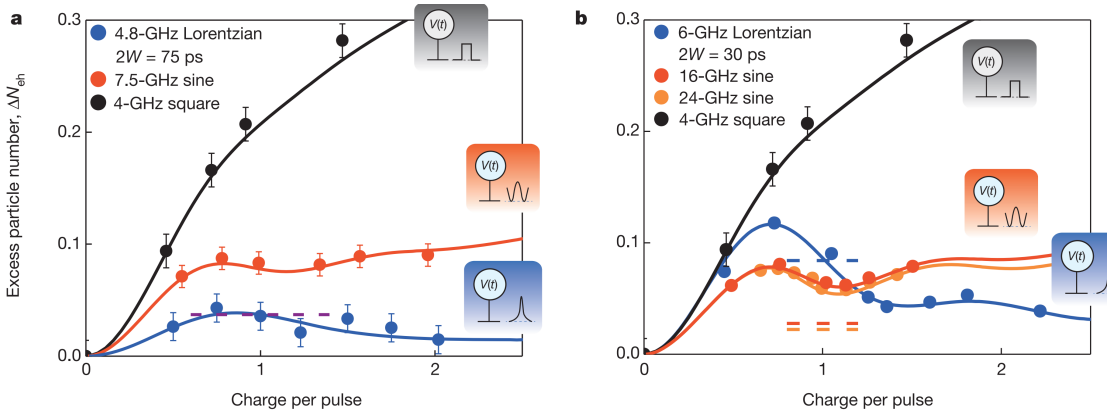

Figure 1.10: Noise measured for different pulse shapes. **a,** Excess particle number measured for different amount of charge per pulse. The blue, red and black circles are measuring applying a Lorentzian, sine and square voltage signals, respectively. The lines are theoretical predictions including small heating effects [66]. **b,** Same as **a** but using higher frequency pulses. The minimum noise for the Lorentzian is shifted to $q = 1.4$, due to the thermal fluctuations, as shown by the blue curve. Figure adapted from [66].

defined energy, 100 times smaller than the electron emitted with the dynamic quantum dot. The presence of two edge-channels can induce decoherence due to Coulomb interactions [31]. The electron emitted using a moving quantum dot (SAW) propagates over a depleted path; that means, there is no Fermi sea. This should reduce the energy relaxation over the same length. At the same time, the electron gets more sensitive to external perturbations, since the screening induced by the electrons of the Fermi sea is reduced. The decoherence process needs to be studied in detail, before deciding which of these systems is the best for building a flying qubit.

1.7.5 Manipulation of the quantum state of a flying electron

In the previous section, we have discussed the different approaches to generate a single-electron excitation. We have seen the advantages of using the Leviton source, and we will investigate how to proceed towards a flying qubit with this source.

In the following we will describe how one could use single electrons to realise an electronic flying qubit and how one can create a universal set of quantum gates with such a system.

Benjamin Schumacher created the term qubit [71], thinking about encoding information in a two-level system, the spin of an electron. The essential build block here is a two-level system, and not necessarily the spin.

Here we will consider an electron-charge based system, where there are two different waveguides (rails), and the location of the electron defines the state of the qubit. Thus, if the electron is in the upper rail, we consider that the system is in the logical state $|0\rangle$. However, if the electron is on the lower rail, the logical state is $|1\rangle$, as represented in figure 1.11**a**. One of the advantages of this architecture is the double degeneracy of the ground state [72] for the electron in $|0\rangle$ or $|1\rangle$ rails. We can think that the electron placed in one of the rails has energy ε. If the rails are well separated, there is no tunnelling from one

state to the other.

Let us discuss how we can perform quantum manipulations with the state of our qubit. One can engineer waveguides that are very close, such that one can induce a tunnel-coupling between them for a certain length L_T. When the electron arrives at the tunnel barrier, it will experience a coupling potential, and there is a probability that the electron tunnels from one rail into the other. One can set the tunnelling to have a 50% of probability in each output. In this case the system works as a beam splitter.

The tunnel coupling gives rise to hybridisation between the two initial states, thus we have new eigenstates, the symmetric $|S\rangle$ and antisymmetric state $|A\rangle$ [52, 72–78], where $|S\rangle = \frac{1}{\sqrt{2}}(|0\rangle + |1\rangle)$ and $|A\rangle = \frac{1}{\sqrt{2}}(|0\rangle - |1\rangle)$. After the electron has reached the end of the interaction region, the waveguides are separated again. This leads to a projection of the antisymmetric / symmetric states back to the base $|0\rangle$ / $|1\rangle$. We can rewrite the logical states $|0\rangle$ and $|1\rangle$ in the new eigenbasis as:

$$|0\rangle = \frac{1}{\sqrt{2}}\left(|S\rangle + |A\rangle\right) \tag{1.10}$$

$$|1\rangle = \frac{1}{\sqrt{2}}\left(|S\rangle - |A\rangle\right) \tag{1.11}$$

Considering the initial energy of the states $|0\rangle$ and $|1\rangle$ equal to ε and the energy due to the tunnelling barrier as t_c then the energy of the antisymmetric (symmetric) state is: $\mathrm{E_{A(S)}} = \varepsilon - (+)\, t_c$ and wave vector $k_{A(S)}$. The wave function picks up a phase $e^{i\Theta_{A(S)}}$ inside the tunnelling region and considering the WKB approximation $\Theta_{A(S)} = \int_0^{L_T} dx k_{A(S)} \approx k_{A(S)} L_T$ [79], the wave function after the tunnel region will be:

$$|0\rangle = \frac{1}{\sqrt{2}}\left(e^{ik_S L_T}|S\rangle + e^{ik_A L_T}|A\rangle\right) \tag{1.12}$$

$$|1\rangle = \frac{1}{\sqrt{2}}\left(e^{ik_S L_T}|S\rangle - e^{ik_A L_T}|A\rangle\right) \tag{1.13}$$

One can derive the transmission matrix considering that the initial state is $|0\rangle$ or $|1\rangle$ and the phase shifts due to the tunnel barrier, described in equations 1.11 and 1.13. We have detailed how to derive this matrix in appendix B. The final result is:

$$S_T = \exp\left(\frac{i(k_S + k_A)L_T}{2}\right)\begin{pmatrix} \cos\left(\frac{(k_S - k_A)L_T}{2}\right) & i\sin\left(\frac{(k_S - k_A)L_T}{2}\right) \\ i\sin\left(\frac{(k_S - k_A)L_T}{2}\right) & \cos\left(\frac{(k_S - k_A)L_T}{2}\right) \end{pmatrix} \tag{1.14}$$

The matrix corresponds to a rotation around the x-axis in the Bloch sphere formalism [52] of $\Delta\Theta = (k_S - k_A)L_T$. Therefore, we can tune the angle of the rotation, changing the momentum of the electrons or the length of the tunnel barrier structure. It is possible to vary the height of the tunnel barrier to change the momentum. To change the effective length of the tunnel barrier is more difficult as the length is set by the geometry of the device. One could try to design the tunnel barrier with several gate segments in order to be able to change *in-situ* the length of the tunnelling interaction, but this requires

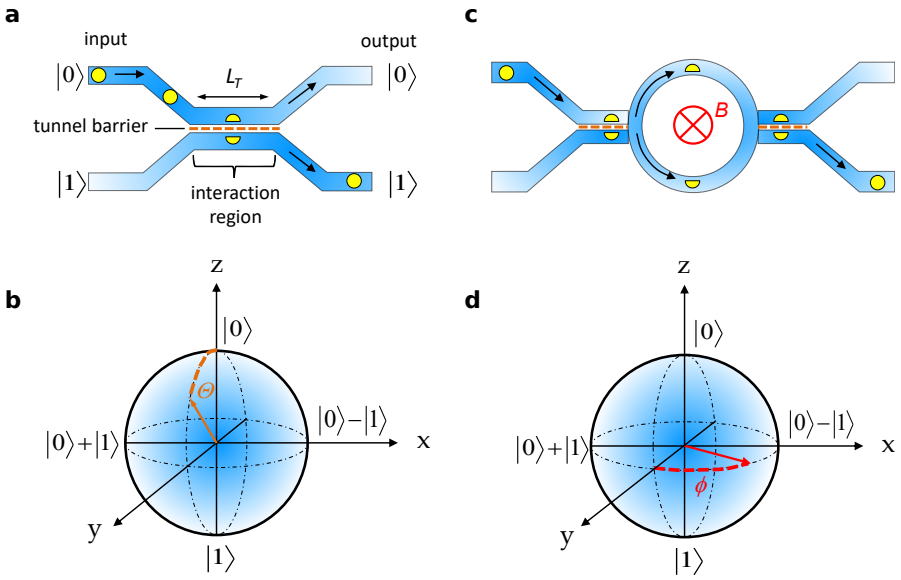

Figure 1.11: Schematic of electron waveguides and how to perform operations in the Block-sphere of a flying-qubit. a, Two electron waveguides are used as the two qubits states of the flying qubit. The tunnel barrier (orange dashed line) is used to induce hybrid states between the two waveguides. **b,** Bloch-sphere representation of the phase acquired by the qubit in the presence of the tunnel barrier. **c,** AB ring used to induce a relative phase between the two paths. There is also a tunnel barrier before and after the AB ring to have access to the full Bloch sphere. **d,** Phase accumulated on the Bloch sphere due to the AB ring. Figure adapted from reference [52].

more sophisticated nanofabrication as bridge connections would be required. Another possibility is to induce a tunnel barrier with a time-dependent control. This approach is currently pursued in the group by J.L. Wang to realize a electronic flying qubit using surface acoustic waves. This approach could also be transposed to our system, however, one needs to know the velocity of the electron that propagates on the rails, in order to determine the time scales on which the tunnel barrier needs to be varied. For the reader interested in time-resolved simulation of such a quantum system, we address the reader to the references [78–81].

We still need to generate a rotation around another axis to have full control of the Bloch sphere in our system. This control can be done via the Aharonov-Bohm effect, in a similar way that we have explained when we introduced the Mach-Zehnder interferometer 1.5.1. To make a similar structure, we can separate the two rails and apply a magnetic flux on the encircled area between the two paths. One big difference here is that we defined the waveguides with electrostatic gates. The phase difference is $\Delta\varphi = \int \mathbf{k} \cdot d\mathbf{l} - \frac{eBA}{\hbar}$ [52], where $\mathbf{k}$ is the wave vector of the electrons in the paths, $d\mathbf{l}$ is the enclosed area A defined by the waveguides, e is the electron charge, and B is the magnetic field. Here, we can control the phase of the electrons by sweeping the magnetic field, but this is a slow operation to perform - in the most optimistic case in the order of µs. To compare with the time-of-flight

of the electron over the interferometer, taking the Fermi velocity of roughly $2 \times 10^5\,\mathrm{m\,s^{-1}}$, and length of 5 µm, this gives a time-of-flight of 25 ps. Thus it would be impossible to adjust the magnetic field during the flight of the electronic excitation. Once more, the knowledge of the electron velocity in such a system is of fundamental importance to envision precise quantum manipulations of the qubit state.

Another way to control the phase is by changing the term $\mathbf{k} \cdot d\mathbf{l}$. In the case of the MZI interferometer using edge channels as waveguides for the electrons (see figure 1.3), we have seen the use of electrostatic gates to vary the length of the path, which can be performed in a fast time scale of few ps. In our case, we use electrostatic gates to define the waveguides. Thus we cannot vary the length adding a Schottky gate as it has been done in figure 1.3. However, by changing the potential of the gates, we can vary the wave vector $\mathbf{k}$, by changing the potential energy defined with the electrostatic gates. Hence, we will affect the kinetic energy of the electrons. The transmission matrix for this case is [30, 52, 72]:

$$S_{AB} = \begin{pmatrix} 1 & 0 \\ 0 & e^{i\varphi} \end{pmatrix} \tag{1.15}$$

Here we do not have off-diagonal terms, because there is no tunnelling permitted, just a relative phase between the paths. The matrix 1.15 corresponds to a rotation around the z-axis of the Bloch sphere [30, 52]. Therefore, we can combine a tunnel-coupled-wire system with the AB interferometer and another tunnel-coupled-wire system to achieve a universal control of the state of the qubit with the universal transformation defined as [80, 82]:

$$U(\alpha, \beta, \theta) = S_T\left(\alpha - \frac{\pi}{2}\right) S_{AB}(\theta) S_T\left(\beta + \frac{\pi}{2}\right) \tag{1.16}$$

We show a schematic version of an interferometer made to perform a universal transformation in 1.11**c,d**, together with the equivalent rotation in the Bloch sphere of each operation.

The authors of ref. [30] have realized an experimental version of the concepts mentioned above. We show in figure 1.12 the SEM picture of the sample used in this experiment. A DC bias is injected in the upper waveguide on the left. The two waveguides are separated by a very thin gate (V_{T2}) that works as a tunnel barrier. Next, the two waveguides go to a region where there is a wide gate separating the paths (V_{T1}), and this defines the AB ring. Another tunnel-coupled wire defined by (V_{T1}) is connected to the AB ring. Two ohmic contacts allow to measure the current of each waveguide. Ideally, one could perform a universal transformation as written by equation 1.16, since this structure allows rotation around the x-axis, then one can perform a rotation around the z-axis, and finally do another rotation around the x-axis.

Coherent oscillations (see figure 1.12) are observed which correspond to the operation of the tunnel-coupled wire (TCW) of figure 1.11 **b**. The electrons are injected in the upper branch by applying a voltage to the upper left ohmic contact. Polarizing V_{T2} such that there is no tunnelling before the AB ring and sweeping the TCW V_{T1}, it is possible to achieve a situation where the channels in the different waveguides hybridize. By changing the energy of the tunnel barrier one observes coherent tunnel oscillations. Smoothed

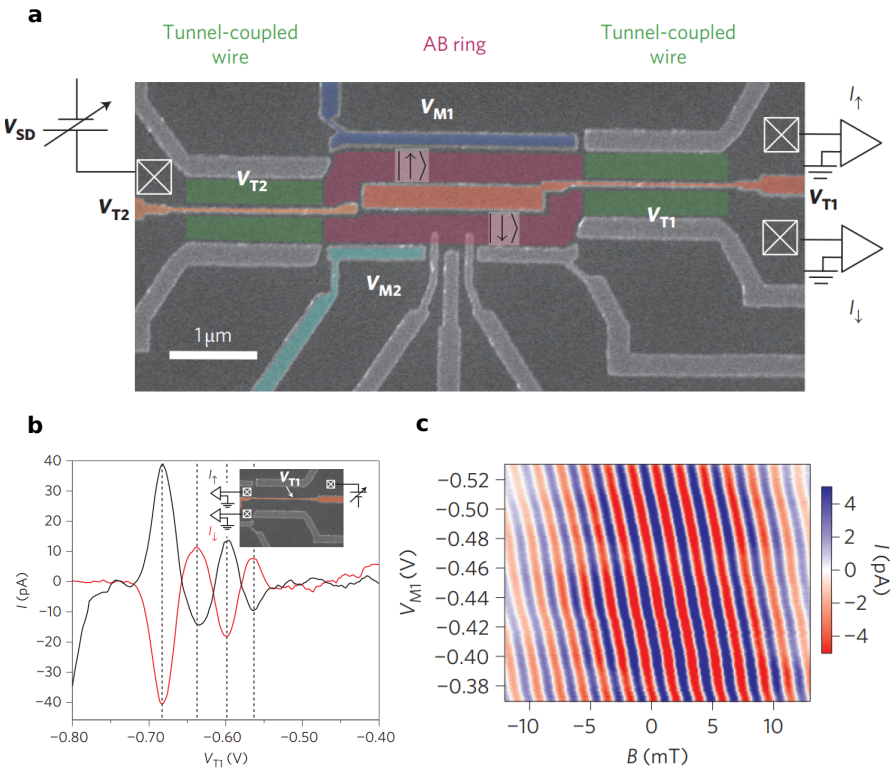

Figure 1.12: Electronic flying qubit using ballistic electrons. **a,** SEM image of the device. A DC voltage is applied to the left ohmic contact and the current is collected on the right ohmic contacts. **b,** Coherent tunnel-oscillations as a function of the tunnel- barrier-gate voltage V_{T1}. **c,** Current oscillations measured in the upper contact when sweeping the magnetic field or the upper side gate (V_{M1}). Figure adapted from reference [30].

background from the current at the upper and lower waveguides are subtracted, to present only the oscillating part.

The AB ring is defined by polarising the gate V_{T1}, in the red region of figure 1.12. As discussed before, one can change the relative phase between the paths by sweeping the magnetic field, or by changing the **k** vector of different branches by sweeping V_{M1} or V_{M2}. This control of the relative phase is shown in figure 1.12 **c**, where the current measured in the upper wire is displayed. Conductance oscillations are observed when setting the two tunnel-coupled wires to perform a rotation of $S_T(\pi/2)$ varying the magnetic field or the voltage on the gate V_{T1}.

The visibility of the oscillations was rather low, for the tunnel-coupling wire is of $\sim 1.4\%$ at $V_{T1} = -0.6\,V$. This low value might be related to the high temperature (2.2 K) of the experiment and the presence of a few transmitting channels [30]. The visibility of the AB oscillation is of $\sim 0.3\%$ [30]. This visibility has been improved to $\sim 10-15\%$ in a more recent experiment [83, 84] by simply improving the gate geometry. For the ensemble of operations ($S_T - S_{AB} - S_T$), it has been found that the oscillations are maximized when

the TCW are adjusted to perform a rotation of $\pi/2$. The coherence length of the system is estimated to be $l_\varphi = 86\,\mu\text{m}$ at 70 mK.

It is important to emphasise that this experiment was performed using a DC bias, that means with a continuous stream of electrons and is far from the single-electron regime that we have discussed earlier. Nevertheless the basic concept of a electronic flying qubit has been realized. Further investigations are needed to have a better understanding of the individual components of the system. In addition, it would be desirable to realise such experiments at the single-electron level by integrating single-electron sources. This will require a detailed investigation of coherence properties of such a system when operated with a single electron source. These investigations are an on-going project in our research group.

1.8 Detection of a flying-electron

We already discussed how to create an electronic excitation and how to manipulate the electron on the fly. To finish the description of the main challenges of developing an electronic flying qubit, we need to discuss how to detect the flying electron.

The detection of a single-charge is needed to achieve all the requirements for a qubit [85]. Moreover, it should be made in a single-shot way, to envision a fast cycle operation (creation, manipulation and detection) of the flying qubit. The single-shot detection might be applied to characterise quantum-coherent conductor, via the distribution of waiting times between charge pulses [86, 87]. This part is by far, the most complicated task in this architecture — many things need to be addressed to manage this challenge. For the moment, the state-of-the-art in single-electron detection on-chip is two orders of magnitude above the precision needed to detect a single *flying* electron. [88, 89]. The idea which we are pursuing in our research group is the following. We will couple a spin qubit capacitively to the propagating electron [90]. We will exploit the extreme sensitivity of such a system to charge fluctuations and store the information in the spin degrees of freedom which can be kept over a sufficiently long time for read out. An important time scale for the realisation of such a detector is the interaction time of the propagation wave packet with the detector. Time-resolved measurements of the wave packet are hence required to characterise the widths and velocity of the pulse across the detector.

The operation principle of the spin-qubit detector is the following. To operate in the singlet-triplet regime, we place one electron in each dot, with antiparallel spins. The potential detuning between the quantum dots and their tunnel coupling determines the energy separation between the ground state and the first excited state. This separation can be controlled over a large range, extending from almost zero until a few gigahertz for quantum dots in GaAs [91]. Therefore, this is a promising candidate for an electrometer. The singlet-triplet system can be prepared in a way that the system is oscillating between the singlet and the triplet state. The flying electron passing by the double-quantum dot would change the electrostatic environment around the dots, what would change the frequency of the Rabi oscillations. The system needs to be optimised and calibrated such that we have an accumulated phase that differs from π if an electron passed by the detector.

We show in figure 1.13 **a** a schematic of an S-T_0 system, where we have a double quantum

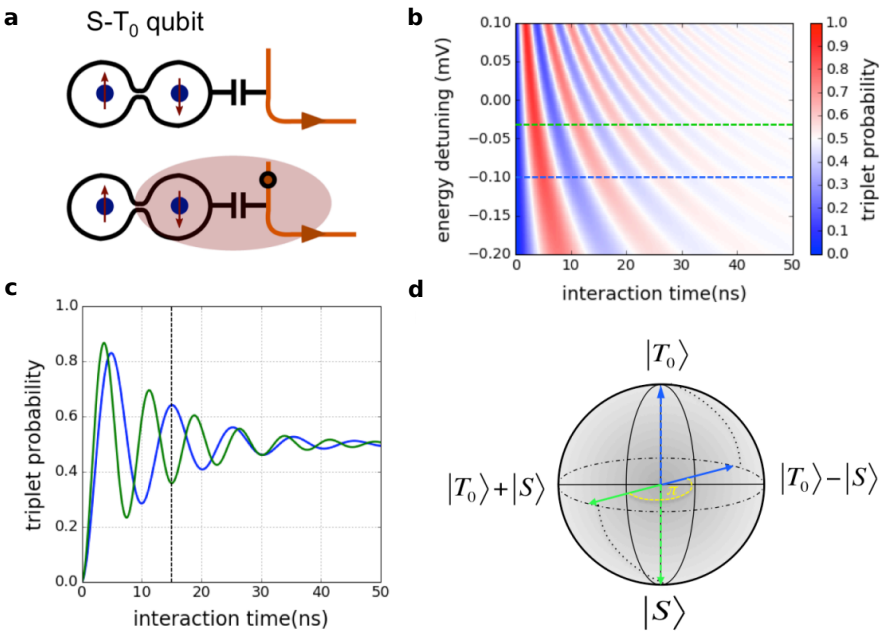

Figure 1.13: Operation of the S-T_0 detector. **a,** Schematic of a double quantum dot capacitively coupled to an electron waveguide. **b,** Simulation of the Rabi oscillations, giving the triplet probability as a function of the energy detuning of the quantum dots and the interaction time. **c,** Triplet probability versus interaction time, for the energy detunings highlighted by the coloured dashed lines in **b**. **d,** Bloch sphere representation of the spin-qubit, where a π shift is shown between the green and blue arrows, representing the black dashed line in c. The figure is reproduced from [52].

dot with one electron placed on each dot. This system can be placed close to one waveguide, and due to Coulomb interactions, it will be sensitive to charge variations on it. The system can be prepared to oscillate between the singlet state and the T_0 triplet state by bringing the system non-adiabatically to a spin state that is not one of the eigenstates of the system [92]. Depending on the energy detuning between the dots, and the interaction time with the passing single-electron wave packet, the probability of the system to be in the triplet state will change 1.13 **b**. The final goal of this scheme is to have enough sensitivity to determine whether an electron went through the waveguide with a single shot measurement. In figure 1.13 **c**, we take as example different energy detunings **b** (dashed lines) that could be induced due to the presence of an electron going through the waveguide. For this energy detuning, if the interaction time is as long as 15 ns, the accumulated phase difference between the presence (or absence) of the electron is π and could hence be measure in a single shot measurement.

The first attempt to create this sensor was made by [90], coupling an electron pulse propagating in an edge channel, created at QHE $\nu = 16$. A shift of π change in the accumulated phase is reported for a pulse of 80 electrons. Improved geometry and faster detection should increase the sensitivity of this detector, allowing the detection of a

single-electron on the fly.

1.9 Characterization of the velocity of a voltage pulse in an interacting system

In the preceding section, we have described how one can build a flying qubit based on propagating single electrons, and we have seen that there are many obstacles to tackle. A critical problem in this respect that we discussed in almost all the main structure of the flying qubit is the need to understand the propagation of electronic excitations in a coherent quantum conductor. Such a study is also exciting from a fundamental research point of view. There is a theoretical proposal [64] that describes unrevealed effects due to the dynamics of a quantum conductor. However, to achieve a regime where we could see these effects, we need to be able to generate a wave packet whose width is much shorter than the time-of-flight.

To give a clear idea of this challenge, considering that the pulse propagates at the Fermi velocity in gallium arsenide ($2 \times 10^5\,\mathrm{m\,s^{-1}}$) and a path with the length of 10 µm, this gives already a time of flight of 50 ps. However, first, we need to make sure about the velocity of propagation of electrons in quasi-1D systems, that also depends on the strength of the electron-electron interaction.

We will describe in the next subsections how experiments using the tunnelling of electrons between quantum wires, were able to determine indirectly the velocity of the electrons in DC measurements. Then, we will discuss how to perform time-resolved measurements that allows us to have direct access to the time-of-flight of the wave packets, thus the velocity.

1.9.1 Single electron tunnelling experiments

In the last two decades, with the advent of sophisticated nanofabrication techniques, it was possible to perform experimental studies about the interaction between electrons in 1D. As we will see in chapter 2, a convenient way to probe electron-electron interactions is to measure the propagation speed of an electron wave packet. This can be done either in DC measurements by measuring the dispersion relation or by time-resolved measurements. The former has been addressed by Auslaender *et al.* [93] while in my PhD work I have addressed the latter.

In a pioneering experiment by Auslaender *et al.* [93], they studied the tunnelling of electrons between two long, parallel and ballistic wires to obtain information on the electron-electron interactions. The two parallel wires are separated by a distance d, such that the electrons can tunnelling from one wire to the other. A bias is applied to one of the wires, and the resulting tunnelling current is measured. By biasing the wire one can control its Fermi energy while applying a magnetic field allows to change the momentum of the electrons. The momentum and energy of the electrons are conserved during the tunnelling. Therefore, by varying the bias and the magnetic field, it is possible to map the dispersion relation of the system. A scheme of their system is shown in figure 1.14.

The constraints implied by the conservation of the energy and momentum to permit the tunnelling of electrons between two wires can be illustrated by the dispersion relation, as shown in figure 1.15. The dispersion relation has the form of a parabola since the energy is proportional to the square of the momentum. An offset in the dispersion relation (E_0) appears due to the difference in electron density. In the left part of the figure 1.15, we

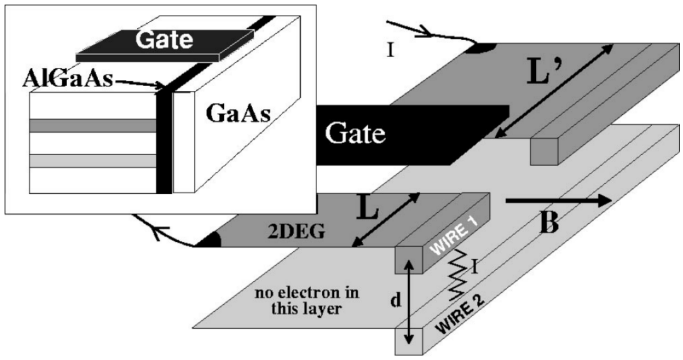

Figure 1.14: 1D wire tunnelling experiment. Schematic of the sample used to measure the tunnelling between two quantum wires. The upper quantum wire is connected via 2DEG. The Schottky gate is used to define the length of the quantum wire, deplete the 2DEG underneath. The figure is reproduced from [94].

show the dispersion relations for each quantum wire. However, the curves are not crossing such that it is impossible to have one electron tunnelling from one wire to another due to energy and momentum conservation. Therefore, the tunnelling is forbidden, and the measured current is zero. Applying a bias, one can shift the dispersion relation such that they overlap and the tunnelling is allowed, having a finite current, as shown in figure 1.15 **middle**. Another way to have an overlap between the dispersion relations is by applying a magnetic field, as exemplified in 1.15 **right**.

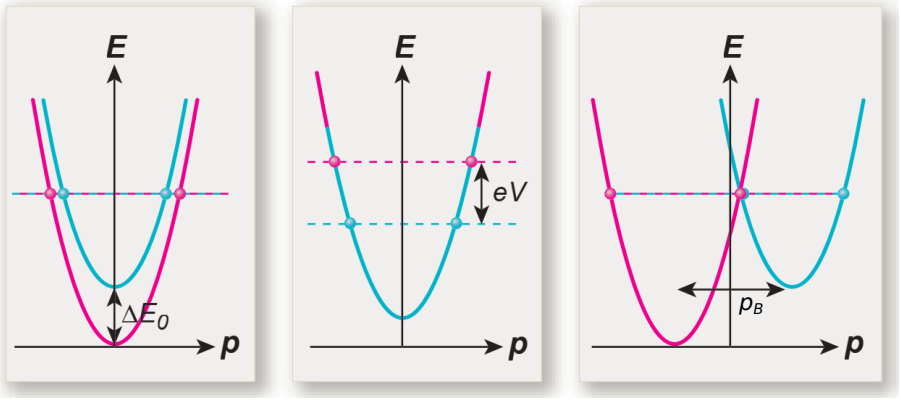

Figure 1.15: Dispersion relation of two parallel quantum wires. The dashed lines represent the Fermi energy in each wire. **Left,** The case when there is no crossing between the different dispersion relation. **Middle,** The pink dispersion relation is shifted by the amount ΔE_0 due to an applied bias $V_{bias} = eV$. **Right,** The dispersion relation is shifted of p_B due to application of a magnetic field. The figure is reproduced from [95].

Therefore, sweeping the voltage bias or the magnetic field and measuring the tunnelling current, one can get information about the dispersion relation of this system which indirectly gives information about the velocity. From the relation $v = \Delta E/\Delta k$ they deduced the propagation velocity, and they observed an incompatibility with the velocity expected from

a non-interacting system [96]. They find the velocity being on the order of 30% faster than the Fermi velocity. In a follow-up work, they observed the long-predicted spin-charge separation [97], due to intra-wire interactions. It is possible to verify from the dispersion relation that one branch corresponds to a velocity faster than the Fermi velocity, while another goes with the velocity close to the Fermi velocity. This prediction agrees well with their experimental data, although the theory also predicts that due to inter-wire interactions, it should exist a branch that propagates with a velocity much higher than the Fermi velocity, but this branch was not detected experimentally. We will give further details about these different velocities, which is referred to as spin-charge separation in section 1.9.2, also often named as charge fractionalisation.

1.9.2 Time-resolved measurements

To obtain a direct measurement of the velocity of an electron pulse propagating in a Fermi sea, one could think about applying a voltage pulse directly to the Fermi sea and measure the time-dependent current $I(t)$ directly. However, this is very hard for ultra-high-frequency signals. Some measurements using this approach were made detecting the current going through edge channels and measure it in a time-resolved manner with the help of a fast sampling oscilloscope [98–100]. To overcome this hurdle, we use a similar approach to what has been developed in Fujisawa's group [101]. In this experiment, an electronic excitation is injected by applying a voltage pulse at the ohmic contact. This excitation propagates over the edge channel until it reaches the switch position. The current crosses the switch depending on whether the switch is ON or OFF. The switch, in this case, is a QPC. By applying a voltage pulse at the QPC, this switch can be opened (ON) for a short time. The current traversing the switch depends on the overlap between the excitation arriving at the QPC position and the QPC opening due to the voltage pulse. By adding a delay between the voltage pulses, it is possible to measure the average current traversing the switch as a function of the delay, thus being able to reconstruct the applied excitation. We describe this technique in more detail in section 3.5 of chapter 3.

The advantage of this method is to measure the average current $I \equiv \langle I(t) \rangle$, instead of the time-dependent one.

This approach for time-resolved measurements developed by *Kamata et al.* [101] was later applied to characterize the time-of-flight of edge magnetoplasmons (EMP) [102], in the quantum Hall regime, where one has only ballistic channels flowing around the edges of the sample. They have edge channels defined by metallic gates, where they can activate different gates to change the length of the edge channels (filling factor $\nu = 2$), as shown in figure 1.16. Due to the different lengths, it is possible to extract the velocity. They also observed an increase in the velocity with the potential of the metallic gates (making it more negative). This increase is related to the reduction of the screening of the metallic gates since the edge magnetoplasmon will propagate further away from the metallic gates, as shown in figure 1.16.

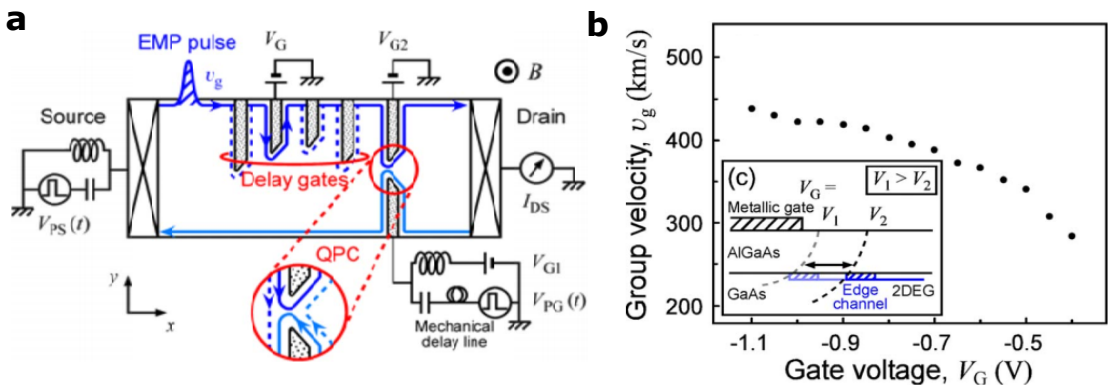

Figure 1.16: Velocity of the EMP. a, schematic of the sample. A voltage pulse is applied to the left ohmic contact (the square with cross) that will propagate towards the right. By polarizing the delay gates, one can change the length of the path that the excitation propagates. The QPC is used as a fast switch to do the time-resolved measurements. The current is measured on the right side, via another ohmic contact. **b** Group velocity as a function of the gate potential V_G.

Separation of the charge mode and neutral mode

Electron-electron interactions in 3D and 2D systems that are well captured by the Landau's Fermi liquid description, where the electrons have low-energy excitations named as quasi-particles [103, 104]. Their behaviour is similar to weakly interacting fermions, where many features can be understood considering the electric charge as free-quasi-particles that respect Fermi statistics.

However, this picture is entirely changed when dealing with 1D systems. The low dimensionality, together with the Coulomb interactions make the electrons to have a collective behaviour. This effect happens because of the movement of electrons is restricted to one dimension – the particles can only move to the left or the right. Therefore any disturbance in the system will make the particles to push their neighbour, affecting all particles in the system, inducing a collective displacement. This collective displacement can be regarded as a superposition of harmonic waves [104]. The quantization of these waves has a bosonic statistic. Considering low-energy excitations, we can neglect the interaction among the different waves, resulting in a system of free bosons [104].

The representation of a 1D system considering many-fermions with low energy excitation is called Luttinger liquid. The Hamiltonian of a 1D interacting system is composed of a kinetic term and a potential term, where the interactions are included. One can linearise the dispersion relation close to the Fermi energy, considering that the excitations are small. Doing so, the Hamiltonian has an exact solution, and it is known as the Tomonaga-Luttinger. This problem is solved using a method called bosonization, where one writes the fermionic theory in terms of bosonic operators. The advantage is to derive a Hamiltonian of interacting electrons in the form of non-interacting particles. The price to pay is that the creation of an electron in a determined place requires operators that involve the dislocation of a high number of particles, that is, highly non-local [104]. The mathematical details of

this derivation is presented in references [105–108] for interested readers. We will focus on the main consequences of such a model.

One of the outstanding results of this model is the occurrence of spin and charge waves. The Hamiltonian considering all interactions in one-dimensional separates in terms that involve just the charge and terms that considers just the spin [108]. Therefore, the charge and the spin component can have different velocities [108]. The different velocities give rise to the phenomena called spin-charge separation. The electron tunnelling experiments could probe this separation [97] since to accommodate an extra electron requires charge and spin displacements [104]. The repulsive interactions among the electrons increase the velocity of the charge waves in comparison to the Fermi velocity. On the other hand, the velocity of the spin waves is hardly affected by weak but long-range charge-charge interactions [104].

Furthermore, we can think of coupling two 1D systems, considering two quantum wires in parallel where the Coulomb interaction mediates the coupling between them. The coupling gives rise to new propagating eigenmodes for the charge waves along each wire [97, 109]. These modes have different velocities, such that one will propagate much faster than the other. The faster mode is called *charge* mode, and the polarity of the charges propagating in each wire is the same. The other mode will have roughly the Fermi velocity, and the charge distribution will have opposed polarity in each wire. This mode is called the *neutral* mode [110] because summing the charge in the two different waves for a fixed position one obtains approximately a zero net charge. Sometimes this is referred to the *spin* mode [111], which can be misleading since the spin is playing no role here. In figure 1.17, we show how these two modes would appear separated in time and space. The separation of the different modes is also known as the charge fractionalization.

One can use a system similar to quantum wires to study these collective effects. For instance, one can use the quantum Hall effect and set a 2DEG to have only two co-propagating edge channels. Therefore, forming a system similar to having two parallel quantum wires. It is possible to inject a charge in one edge channels and measure the current induced in a second edge channel. One can compare the ratio of the transmitted current by the second edge channel, in comparison to the measured current transmitted by both channels. A study conducted by Fève's group [112] has done this experiment, varying the frequency of the charges injected in the edge channel. The creation of the charges is done by driving a mesoscopic capacitor coupled to the first edge channel. They have obtained a good agreement between experiments and simulations of the high-frequency admittance, considering the existence of charge and neutral modes [112].

Other studies investigated the fractionalization effect measuring the partition noise on a second edge channel and found a good agreement between experiments [113] and theory [114].

The charge fractionalization was also observed with the electronic version of the Hong-Ou-Mandel interferometer [115]. This interferometer consists of the collision of indistinguishable particles going into a beam splitter. Depending on the statistics of the particles, they will bunch (bosons) and go together to one of the detectors. For fermions, due to the Pauli principle, the particles should anti-bunch and will be detected in separated detectors, as observed by [31]. Changing the delay between the charge launched into the edge channels, the (anti)bunching effect can be probed between the charge and neutral modes in the

different channels, as nicely demonstrated by [115].

A very beautiful experiment has been realised recently by the Fujisawa group [111] where they have been able to measure in a time-resolved way the separation of charge and neutral modes in one-dimensional chiral edge channels. The experiment is executed once more using two co-propagating ballistic channels (filling factor 2) with opposite spins. The theoretical expectation is that, due to the Coulomb interactions, the two co-propagating channels are coupled, thus having new propagating eigenmodes. This coupling should give rise to the charge and neutral modes.

As depicted in figure 1.17, injecting an electron wave packet in one of the channels, the wave packet will fractionalize and will split into two, due to Coulomb interactions. The wave packet on the right (iii) is the one where the charge has the same signal on both channels. The wave packet on the left (iv) is the neutral mode, which is composed of one positive charge pulse in one channel and a negative charge pulse in the other channel, propagating together. The different modes propagate with different velocities, so that after some length, the modes are spatially separated.

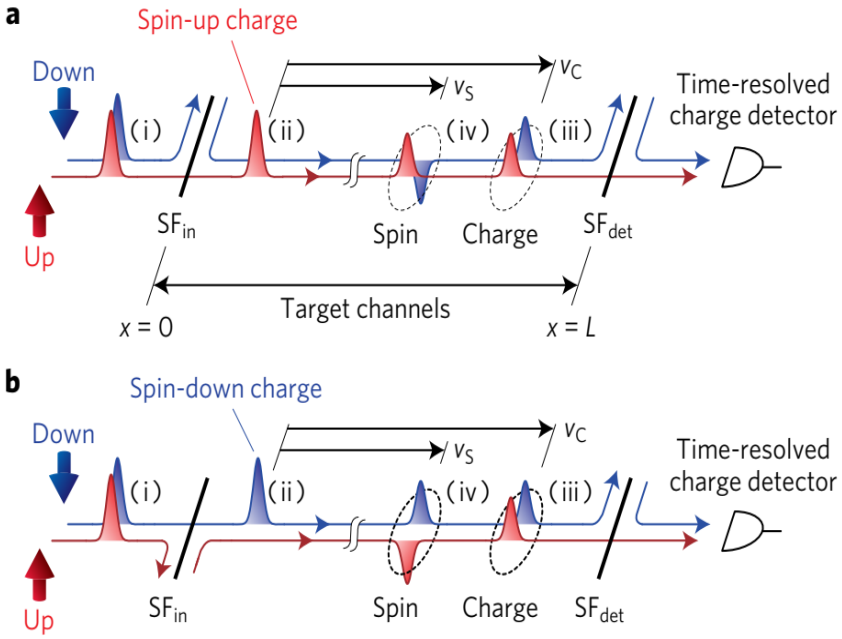

Figure 1.17: Separation of charge and neutral modes. An excitation is created at the upper and lower co-propagating channels (i), applying a square pulse on a metallic gate. The co-propagating channels are then filtered using the gate (SF_{in}) and subsequently the channels are put back together, such that there is an initial excitation in a single channel (ii) **a** lower channel; **b** upper channel. Due to Coulomb interactions, the charge mode that propagates faster (iii), and the neutral mode (spin) that arrives later (iv) are separated in space. Figure adapted from [111].

In this experiment [111], due to the sample architecture, the time-resolved charge detector works only for the lower channel. Exchanging the edge channel where the electron excitation enters gives the possibility to do time-resolved measurements to investigate what happens

in both channels. One can then determine whether the neutral mode has a positive charge pulse in one of the channels and a negative one in the other. Their results are plotted in figure 1.18, where the dashed black line corresponds to the case when the charge pulse is applied to both channels. As the charge mode is an eigenmode of the system, a single-peak is observed, and fractionalization does not happen. However, injecting the charge pulse into a single edge channel, fractionalization takes place, and it is possible to see separated pulses in the time-resolved current, corresponding to the charge mode (two positive wave-packets) and the neutral mode (wave-packet of opposite signals in each channel).

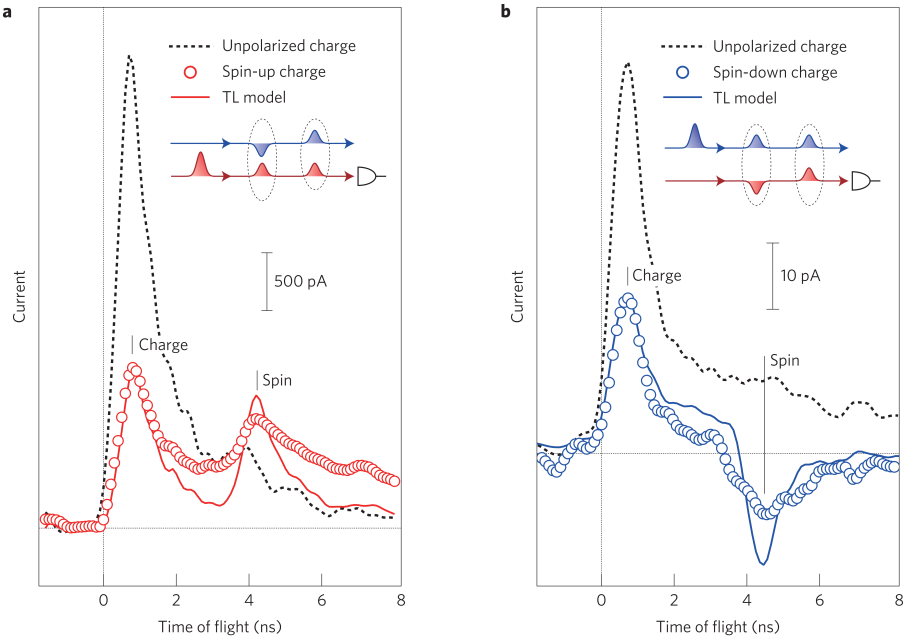

Figure 1.18: Measuring the separation of charge and neutral modes. Time-of-flight of the pulses along the channels. The dashed line corresponds to the measurement when the excitation is injected in both channels, with no filter applied. **a, (b)** The red (blue) circles corresponds to the time-resolved measurements when the excitation has been prepared with the filter-gate in the red (blue) channel. The first peak corresponds to the charge mode and the second one to the neutral mode. The red (blue) line corresponds to simulated curves. Figure adapted from [111].

One can calculate the velocity of the different modes, taking into account the length between the electron injection and detection, and the time-of-flight. The results are shown in figure 1.19. A critical parameter in this system is the Coulomb interaction which controls the inter-channel interaction, responsible for the coupling between the different channels and also the intra-channel which renormalizes the group velocity [111]. One way to play with the Coulomb interaction is to have a Schottky gate close to the edge channels. The closer the edge channels are to the gate, the more the Coulomb interactions will be screened and the velocity of the charge mode is strongly reduced. This reduction is experimentally confirmed, as shown in figure 1.19. The higher the voltage, the closer the edge channels are propagating to the gate, reducing the velocity.

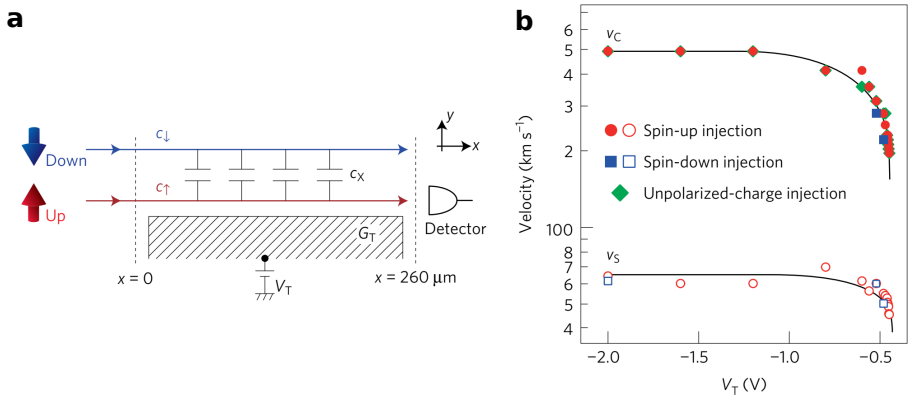

Figure 1.19: Velocity versus the depletion gate. **a,** Representation of the two co-propagating channels. $c_\uparrow$ and $c_\downarrow$ are the capacitive coupling to the gate V_T and c_x is the capacitance between the two channels. **b,** The velocity of the charge and spin mode injected in the upper (red) or lower (blue) channel. Data in green show the case when the excitation is propagating in both channels (no filtering applied), when varying the potential V_T. Figure adapted from [111].

Similarly to the experiment that we just mentioned, the core of this PhD work is about the study of the propagation of electron wave packets in a system of reduced dimension, and the spectacular effects induced by the Coulomb interaction.

1.10 Conclusion

The recent advances in nanofabrication gave birth to an entirely new field of studies, namely *electron-quantum-optics*. We have seen quantum effects discovered in the '80s as the quantum Hall effect and the quantisation of the conductance as well as the first realization of interferometers that use electrons instead of photons. The progress in the field over the last 10 years has been such that one can now envision to use propagating electrons as flying qubits. For the manipulation and detection purposes, it is vital that we first understand the propagation of the electron in quasi-1D systems, which is the core of this PhD study. In the next chapter, we will discuss the theory behind the use of voltage pulses applied to a 2DEG. In chapter 3, we will focus on the experimental setup. This includes the samples that have been used and fabricated during this thesis, the electronic setup and the sample characterisation. In the last chapter, I present my main experimental results of the electron propagation in a quasi-1D system.

CHAPTER 2

Plasmon theory

In this chapter, we describe the physics behind the use of voltage pulses in a two-dimensional electron gas. Naively speaking, the velocity of propagation for a non-interacting system is the Fermi velocity. The material that we use has an electronic density of $n_s = 2.11 \times 10^{11}\,\mathrm{cm}^{-2}$, which gives a Fermi velocity of $\approx 2 \times 10^5\,\mathrm{m/s}$.

As we will see later on, the velocity we measure for an electron wave packet turns out to be much higher than the Fermi velocity. This led us conclude that a simple non-interaction model is not sufficient to explain the physics of our system.

The Tomonaga-Luttinger liquid is a theoretical model that describes interacting particles in a 1D system [104]. One of the hallmarks of this model is the appearance of charge and spin waves. To imagine these waves, we can think of a one-dimensional system where exactly one particle is allowed per site. Adding a new particle in the middle of the system, it will displace other particles by one site in total, leading to a collective effect.

Moreover, one can think about the collective effect that may arise when injecting an electron in a slightly different system, composed of not just one, but several 1D coupled systems. The coupling can be done by Coulomb interactions, for example. In this PhD work, we address the study of such effects, performing time-resolved measurements of single-electron wave packets injected into quasi-1D conductors. These measurements allow us to calculate the velocity of propagation of an electron wave packet in a quasi-one-dimensional system, which gives important information about the excitation itself. We will discuss the experimental way to determine the velocity in the next chapters.

To form a quasi-1D system, we can use Schottky gates deposited on the surface of a 2DEG to define an electron wave guide. By applying a voltage pulse directly to a two-dimensional electron gas we locally perturb the electronic density. This modulation of the density creates the collective excitation, called plasmon. Matveev and Glazman derived a solution of the velocity of the propagation of the plasmon propagating over an arbitrary number of interacting conductance channels [109]. They have tackled this problem applying the bosonization formalism in the Hamiltonian of free electrons in the presence of screened Coulomb interactions. The velocities found using the screened Coulomb potential do not quantitatively explain our experimental results. Hence, a realistic description of the electrostatic environment has to be taken into account. This description has been done in collaboration with the group of Xavier Waintal, and we will see that such an approach satisfactorily describes our experimental data in chapter 4.

We will present in the next sections a complete theoretical description of the plasmonic problem, although we will follow a slightly different approach than the one used by Matveev

and Glazman [109]. We follow the steps presented in reference [36], who performed the numerical simulations presented in this PhD work.

This chapter is structured in the following way: First, we will solve a general problem of the electrostatics of a two-dimensional conductor in the presence of a metallic gate. Then, using a semi-classical theory, the kinetic Boltzmann equation, we will find the out-of-equilibrium partition density. Afterwards, we calculate the variation of the density, arriving at a self-consistent problem. Putting together the new densities and the quantum solutions for the 2D problem, we can calculate the renormalised velocities in the presence of the Coulomb interactions. We discuss how to adapt the 2D problem to the quasi-1D system. Reference [116] was the first who obtained the solution of the quasi-1D problem. Finally we apply the solution of the quasi-1D problem for the simplest case, with the presence of two channels, to to show in a clear way how the renormalisation mechanism works.

2.1 Electrostatic problem

We start considering the electron density of our system as:

$$n = n_0 + n_1(\vec{x},t), \tag{2.1}$$

where n_0 is the electron density in equilibrium and $n_1(\vec{x},t)$ is the modulation of the Fermi sea generated due to the voltage pulses on the plane $\vec{x} = (x,y)$. We are considering the electron gas placed at z=0. The voltage induced due to the modulation can be calculated with the Poisson equation,

$$\nabla^2 V = s\frac{en_1(\vec{x},t)}{\varepsilon}, \tag{2.2}$$

where $s = 2$ is due to the spin degeneracy, meaning that at every site we have two spins with different orientation. ε corresponds to the dielectric constant of the surrounding material. We consider as the ansatz that the modulation behaves like a plane wave in (x,y),

$$n_1(\vec{x},t) = n_1 e^{i(\vec{q}\cdot\vec{x}-\omega t)}, \tag{2.3}$$

where $\vec{q}$ is the momentum of the plasmon. Considering the induced voltage due to the modulation as:

$$V(\vec{x},t) = V.u(z)e^{i(\vec{q}\cdot\vec{x}-\omega t)}, \tag{2.4}$$

where $u(z)$ is the solution in the z-direction. We assume the presence of metallic gates above and below the 2D electron gas ($z = 0$) at positions $z = \pm d$, which imposes the boundary condition $u(\pm d) = 0$.

To find the induced potential, we can use the fact that the electric field has a discontinuity at $z = 0$ equals to:

$$[\vec{E}(z = 0^+) - \vec{E}(z = 0^-)].\hat{z} = -s.\frac{en_1(\vec{x},t)}{\varepsilon}. \tag{2.5}$$

Since $\vec{E} = -\nabla V$, we have:

$$V\left[\frac{du}{dz}(z=0^+) - \frac{du}{dz}(z=0^-)\right] = s.\frac{en_1}{\varepsilon}. \tag{2.6}$$

Now, let us solve the Poisson equation for $z \neq 0$:

$$-q^2Vu + Vu'' = 0. \tag{2.7}$$

The solution $u(z) = A\sinh(qz) + B\cosh(qz)$ satisfies equation 2.7 and considering the boundary conditions $u(\pm d) = 0$, we have:

$$u(z) = B_+\big(-\frac{\cosh(qd)}{\sinh(qd)}\sinh(qz) + \cosh(qz)\big) = -B_+\frac{\sinh(qz-qd)}{\sinh(qd)} \text{ for } z > 0, \tag{2.8a}$$

$$u(z) = B_-\big(\frac{\cosh(qd)}{\sinh(qd)}\sinh(qz) + \cosh(qz)\big) = B_-\frac{\sinh(qz+qd)}{\sinh(qd)} \text{ for } z < 0. \tag{2.8b}$$

Considering the continuity of the potential at $z = 0$, we obtain the relation between B_+ and B_-, which implies that $B_+ = B_-$. We adopt a new $\tilde{V} = VB_+$. Considering the boundary condition of equation 2.6, we have:

$$\frac{\tilde{V}q}{\sinh(qd)}[-\cosh(-qd) - \cosh(qd)] = s\frac{en_1(\vec{x},t)}{\varepsilon}$$

$$\implies \tilde{V} = -s\frac{en_1}{2q\varepsilon}\tanh(qd). \tag{2.9}$$

Combining the equations 2.4 and 2.9 give us the induced potential at $z = 0$:

$$V(x,y) = -s\frac{en_1}{2q\varepsilon}\tanh(qd)e^{i(\vec{q}\cdot\vec{x}-\omega t)}. \tag{2.10}$$

We can use the fact that $\vec{E} = -\nabla V$ to calculate the electric field at $z = 0$:

$$\vec{E} = is\frac{\vec{q}}{q}\frac{en_1(\vec{x},t)}{2\varepsilon}\tanh(qd). \tag{2.11}$$

This equation can be generalized for metallic gates placed at different distances from the 2DEG, simply by changing $2/\tanh(qd)$ by $1/\tanh(qd_1) + 1/\tanh(qd_2)$, where d_1 and d_2 are the different distances.

To study the dynamics of our system, we use a semi-classical approach, considering the probability distribution $f(\vec{x},\vec{k},t)$ for the electrons to be at position $\vec{x}$ with momentum $\vec{k}$ at time t. Assuming that:

$$f = f_0(\epsilon(\vec{k})) + f_1(\vec{x},\vec{k},t), \tag{2.12}$$

here, the term $f_0(\epsilon(\vec{k})) = [1/\left(e^{(\epsilon-\epsilon_F)}+1\right)]$ is the Fermi distribution and f_1 is the out-of-equilibrium distribution and $f_1(\vec{x},\vec{k},t) \ll f_0$. It is important to stress the difference

between $\vec{k}$ and $\vec{q}$. $\vec{k}$ is the usual wave-vector of the electron wave-function and $\vec{q}$ is related to the wave-vector of the plasmon, the local change in charge density that propagates. To evaluate f_1 we assume a ballistic system, using the collisionless Boltzmann equation [117–119]:

$$\frac{\partial f}{\partial t} = -\vec{v}_{\vec{k}} \cdot \vec{\nabla}_{\vec{x}} f - \frac{\vec{F}}{\hbar} \cdot \vec{\nabla}_{\vec{k}} f, \tag{2.13}$$

here $\vec{F}$ is the electric force and $\vec{v}_{\vec{k}}$ is the group velocity derived from the non-interacting dispersion relation of the electrons $\vec{v}_{\vec{k}} \equiv (1/\hbar)\vec{\nabla}_{\vec{k}}\epsilon(k)$. We are looking for solutions of the probability distribution with the form $f_1(\vec{x},\vec{k},t) = f_1(\vec{k})e^{i\vec{q}-\omega t}$. Injecting this solution, the force $\vec{F} = -e\vec{E}$ and the general distribution 2.12 into the kinetic Boltzmann equation 2.13, we find:

$$-i\omega f_1(\vec{k}) = -i\vec{q}\cdot\vec{v}_{\vec{k}} f_1 + \frac{e\vec{E}}{\hbar}\cdot\left(\frac{\partial f_0}{\partial \vec{k}} + \frac{\partial f_1}{\partial \vec{k}}\right)$$

$$\implies f_1(\vec{k}).\left(-i\omega + i\vec{q}\cdot\vec{v}_{\vec{k}}\right) = \frac{e\vec{E}}{\hbar}\cdot\left(\frac{\partial f_0}{\partial \epsilon}\frac{\partial \epsilon}{\partial \vec{k}} + \frac{\partial f_1}{\partial \vec{k}}\right). \tag{2.14a}$$

We assume that the variation of f_1 with $\vec{k}$ is much smaller than the change of f_0 with $\vec{k}$, which results:

$$f_1(\vec{k}) = \frac{ie\vec{E}\cdot\vec{v}_{\vec{k}}}{\omega - \vec{q}\cdot\vec{v}_{\vec{k}}}\left(\frac{\partial f_0}{\partial \epsilon}\right). \tag{2.15}$$

We can obtain the out-of-equilibrium density n_1 by integrating f_1 over $\vec{k}$ space. The electron density per spin is defined by

$$n_1(\vec{x},t) = \int \frac{d^2k}{(2\pi)^2} f_1(\vec{x},\vec{k},t). \tag{2.16}$$

The integral is performed on the two-dimensional k space. Now, we arrive at a self-consistent problem, where the electric field depends on the electron density 2.11, and the density depends on the electric field, as shown in equation 2.16. At zero temperature, $\partial f_0/\partial\epsilon$ becomes $-\delta(\epsilon_F - \epsilon)$. For an isotropic band dispersion and assuming θ as the angle between $\vec{k}$ and $\vec{q}$, from equation 2.16 in polar coordinates,we find:

$$\begin{aligned} n_1 &= \frac{ie}{4\pi^2}\int_0^{2\pi}\int_0^{\infty} k\frac{Ev_k\cos(\theta)}{\omega - v_k q\cos(\theta)}(-\delta(\epsilon_F - \epsilon(k))dkd\theta \\ &= -\frac{ieE}{(2\pi)^2}\frac{m}{\hbar^2}\frac{1}{q}\int_0^{2\pi}\frac{\frac{v_F q}{\omega}cos(\theta)}{1-\frac{v_F q}{\omega}cos(\theta)}d\theta \end{aligned}$$

$$\implies n_1 = -\frac{ieEm}{(2\pi q\hbar^2)}\left(-1+\frac{1}{\sqrt{1-(\frac{v_F q}{\omega})^2}}\right). \tag{2.17}$$

We have hence derived the density of the plasmon as a function of the electric field 2.17. Injecting 2.11 into equation 2.17 we obtain:

$$1 = \frac{e^2 sm}{(4\pi)\hbar^2\varepsilon q}\tanh(qd)\left(-1+\frac{1}{\sqrt{1-(\frac{v_F q}{\omega})^2}}\right).$$

Defining $\gamma = \frac{e^2 sm}{(4\pi)\hbar^2\varepsilon q}\tanh(qd)$, and $v_{\text{plasmon}} = v_P = \omega/q$, the previous expression can be written as:

$$\left(\frac{v_P}{v_F}\right)^2 = \left(\frac{1+\gamma}{\sqrt{1+2\gamma}}\right)^2. \tag{2.18}$$

The equation 2.18 gives the renormalisation of the plasmon velocity in comparison to the Fermi velocity, generated due to the Coulomb interactions. Let us evaluate the limits of the plasmon velocity for different wavelengths. For the limit of short wavelength $qd \gg 1$ then $\gamma \to 0$, then $v_P \to v_F$. For the limit of long-wavelength $qd \ll 1$ this gives $\gamma = \frac{e^2 smd}{(4\pi)\hbar^2\varepsilon}$ which means that the v_P is increased with respect to the Fermi velocity. The long-wavelength limit corresponds to our experimental situation. To reach the short-wavelength regime, considering the wave travelling at the Fermi velocity (2×10^5 m/s), we would need a frequency of at least 2 THz to have the wavelength in the order of 100 nm. This limit might be reachable using optoelectronic devices, converting a femtosecond laser pulse into a picosecond electron pulse.

2.2 Quasi-1D problem

In the previous section, we discussed the plasmon velocity in 2D in the presence of metallic gates and which screen the Coulomb interactions. In my PhD thesis, I have studied experimentally mainly the propagation of the plasmon in a quasi-1D system. For this reason we will explain in the following the consequences when the system is confined to such a quasi-1D system.

In experiment we use two parallel metallic gates which are deposited on top of our HEMT, and by applying a negative voltage, we confine the 2D system in one direction, the y-direction for instance. The plasmon propagates thus along the x-direction.

To combine the quantum problem in the transverse direction (y-direction) with the out-of-equilibrium problem in the longitudinal direction (x-direction), we can write the density as the summation of different contributions of the density expected for a 1D-system:

$$n_1(x,y) = \sum_\alpha |\psi^\alpha(y)|^2 n_1^\alpha, \tag{2.19}$$

where $\psi^\alpha(y)$ are the solutions of the Schrödinger equation in the y-direction, considering

the potential as the solution of the 3D Poisson equation at $z = 0$. The density n_1^α is the out-of-equilibrium density of the 1D-system α, and each of this 1D-system α can be regarded as a propagating channel. It is similar to the solution we have shown in equation 2.17, but dealing with the 1D case and it is equal to:

$$n_1^\alpha = \int \frac{dk}{2\pi} f_1^\alpha. \tag{2.20}$$

To calculate the potential induced due to $n_1(x,y)$ we take into account the presence of metallic gates and we consider the long-wavelength limit ($qd \ll 1$). In this limit, the Green's function of the Poisson equation at z=0 takes the form:

$$V_1(y) = \int sG(y,y')n_1(0,y)dy'. \tag{2.21}$$

The Green's function is represented by $G(y,y')$. The density n_1 can be taken at any x position because this problem is translational invariant. One can calculate the average electric field from the last equation, and then insert the average electric field into the equation of electron density of a single channel eq. 2.20, since f_1^α is proportional to the electric field. From this equation one can then derive the expression for the renormalised velocities, as obtained by Matveev and Glazmann [116]. The advantage of this solution is that the problem becomes solvable by numeric methods in a self-consistent way, as we will discuss later. First, let us explore the equation of motion derived in reference [116]:

$$\rho_\alpha \ddot{u}_\alpha = \rho_\alpha v_\alpha^2 u_\alpha^{"} + V_0 \sum_{\beta=1}^{N} n^\alpha n^\beta u_\beta^{"}, \tag{2.22}$$

where n^α is the electronic density in the α^{th} channel, and the density has the form of $n^\alpha = n_0^\alpha + n_1^\alpha$, with $n_1^\alpha = n_0^\alpha u_\alpha^{'}$. $u_\alpha^{'}$ is the first spatial derivative of the displacement operator u_α that has a form of $u_\alpha = \varepsilon_{\alpha\gamma} \exp^{iq_\gamma x - iw_\gamma t}$, which translates the profile of the electronic density in time and position. The term $\ddot{u}_\alpha$ corresponds to the second derivative with respect to time. N is the number of available channels. The term $\rho_\alpha = m^* n^\alpha$ corresponds to the mass density of electron in the channel α and $m^* = 0.067 m_e$ is the effective mass of the electron in GaAs. V_0 is the interaction potential between the different channels. Let us consider V_0 as the screened Coulomb potential, due to the presence of metallic gates used for depletion, thus

$$V_0 = \frac{2e^2}{4\pi\varepsilon_0\varepsilon_r} \ln(k_F D), \tag{2.23}$$

where D is the distance between the conductance channel and the gate, k_F is the wave vector of the electrons in the quantum channel. We assume that a medium separates the gate and the wire with dielectric constant ε_r. V_0 plays the role of coupling the density of different channels, therefore inducing a collective behaviour, in the same way as V_1 in equation 2.21. Injecting u_α into equation 2.22 we find that:

$$-\rho_\alpha \omega_\gamma^2 \varepsilon_{\alpha\gamma} = -\rho_\alpha v_\alpha^2 q^2 \varepsilon_{\alpha\gamma} - V_0 \sum_{\beta=1}^{N} \left(n^\alpha n^\beta q^2 \varepsilon_{\beta\gamma} \right).$$

Defining $s = w/q$ and considering $\rho = m^*.n^\alpha$, we find that:

$$m^* n^\alpha s_\gamma^2 \varepsilon_{\alpha\gamma} = n^\alpha m^* v_\alpha^2 \varepsilon_{\alpha\gamma} + V_0 \sum_{\beta=1}^{N} \left(n^\alpha n^\beta \varepsilon_{\beta\gamma} \right).$$

Now, we will define that $\zeta_{xy} = \sqrt{n^x}\varepsilon_{xy}$, we obtain:

$$s_\gamma^2 \zeta_{\alpha\gamma} = \sum_{\beta=1}^{N} \left(v_\beta^2 \delta_{\alpha,\beta} + \frac{\sqrt{n^\alpha n^\beta}}{m^*} V_0 \right) \zeta_{\beta\gamma},$$

where $\delta_{\alpha,\beta}$ is the Kronecker delta. Using the fact that $n^\alpha = m^* v_\alpha/(\pi\hbar)$, we have:

$$\sum_{\beta=1}^{N} \left(v_\alpha^2 \delta_{\alpha\beta} + \sqrt{v_\alpha v_\beta} \frac{V_0}{\pi\hbar} \right) \zeta_{\beta\gamma} = s_\gamma^2 \zeta_{\alpha\gamma}, \tag{2.24}$$

where $\zeta_{\alpha\gamma}$ is the contribution from the α^{th} channel to the mode γ. s_γ is the renormalised velocity, and it corresponds to the eigenvalue of equation 2.24. To solve this problem, we can calculate $\zeta^{-1} W \zeta = s^2$. Where ζ is the matrix composed by the ζ_γ. To make things more clear, let us analyse the case where we have only two channels available. First, we need to find the eigenvalues of matrix W:

$$\det W = \begin{vmatrix} v_1^2 + V\sqrt{v_1 v_2} - \lambda & V\sqrt{v_1 v_2} \\ V\sqrt{v_1 v_2} & v_2^2 + V\sqrt{v_1 v_2} - \lambda \end{vmatrix} = 0,$$

where $V = V_0/(\pi\hbar)$. For this case, we have two eigenvalues:

$$\lambda = \frac{(v_1^2 + v_2^2) + 2V\sqrt{v_1 v_2} \pm \sqrt{(v_1^2 - v_2^2)^2 + 4V^2 v_1 v_2}}{2}.$$

To simplify even more our problem, we can consider the case where $v_1 = v_2$. For that case we obtain as eigenvalues $\lambda_1 = v_1^2 + 2Vv_1$ and $\lambda_2 = v_1^2$. This implies that $s_1 = \sqrt{v_1^2 + 2Vv_1}$ and $s_2 = v_1$. The eigenvalues are given by

$$\zeta_1 = \frac{1}{\sqrt{2}} \begin{pmatrix} 1 \\ 1 \end{pmatrix} \quad , \quad \zeta_2 \frac{1}{\sqrt{2}} \begin{pmatrix} 1 \\ -1 \end{pmatrix}.$$

For the first eigenvector, ζ_1, we can see that both channels have the same contribution, resulting in a faster velocity. For ζ_2, the contribution of one channel cancels the contribution of the other. Therefore, it becomes almost a charge less mode, that travels with the same velocity as for the case without interaction. The general case, where we have a quantum wire with N available channels, we will end up with N modes. The mode s_1 will propagate much faster than the others and is called the fast (charge) mode. The velocity of the charge mode with the number of channels going to infinite ($N \to \infty$), behave as $s_1 \propto \sqrt{N}$ [109]. The others have a charge almost equal to zero and their velocity almost equal to the Fermi velocity, and they are called the neutral modes.

To derive the velocities s_1 and s_2, we have assumed the screened Coulomb potential 2.23 as the interaction potential between the different channels of conductance. To be able to compare quantitatively the renormalised velocities determined by equation 2.24 and our experimental findings, one needs to use the correct electrostatic potential filled by the electrons in the quantum conductor. It is necessary to simulate the system to address this problem, considering the real parameters of the sample. The input parameters of the simulation are the size and geometry of the Schottky gates, the distance from the gates to the 2DEG as well as the density of electrons of the wafer used. This has been realized by Pacôme Armagnat in collaboration with the group of Xavier Waintal. The steps performed in reference [36] to solve this problem were first to solve the Poisson equation numerically, starting from a given density. Then, using the potential found to solve Schrödinger equation, finding the electronic wave-functions. The next step was to calculate the new density with the electron wave-functions.

This is a self-consistent problem, which is solved by iteration until the error between two successive iteration steps is below the desired error. The equations involved in the self-consistent problem are [36, 120]:

$$\Delta U(y,z) = -\frac{e\rho(y)}{\varepsilon}\delta(z) + \frac{e\rho_0(y,z)}{\varepsilon} \tag{2.25a}$$

$$-\frac{\hbar^2}{2m^\star}\frac{\partial^2}{\partial y^2}\psi_\alpha(y) - eU(y,0)\psi_\alpha(y) = E_\alpha\psi_\alpha(y) \tag{2.25b}$$

$$\rho(y) = \frac{2}{\pi}\sqrt{\frac{2m^\star}{\hbar^2}}\sum_\alpha |\psi_\alpha(y)|^2\sqrt{E_F - E_\alpha}, \tag{2.25c}$$

where Δ is the Laplacian, ρ is the electron density at the 2DEG, ρ_0 is the density of dopants in the heterostructure, and the equation 2.25a corresponds to the Poisson equation, which only needs to be solved in 2D (y,z) due to the translational invariance along the x-direction. The equation 2.25b is the Schrödinger equation for the 1D channels along the y direction, considering that along the x-direction the wave-function is a plane wave. The equation 2.25c corresponds to the new density derived from the result of the Schrödinger equation. The factor 2 is to take into account the spin degeneracy. In the end, the solution of equation 2.25 are the wave-functions, which gives the number of available channels (channels with energy below the Fermi energy) and the electronic density of

each channel. Like this, it is possible to solve equation 2.24 and find the renormalised velocities. For further details we refer the reader to reference [36]. We present the result of the self-consistent calculated density as a function of the gate voltage in figure 2.1.

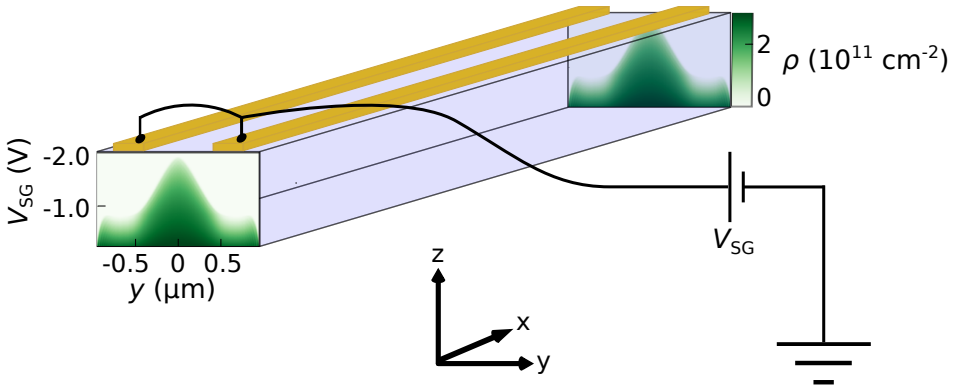

Figure 2.1: Self-consistent electron density. Schematics of the quasi-one dimensional waveguide formed by two parallel electrostatic gates. The density profile when applying a DC voltage V_{SG} to the two gates (in gold) is shown by the two cross sections. Figure adapted from [120].

The drawing in figure 2.1 shows the sample geometry used to solve the self-consistent problem. The coloured images show a cross-section of the electron density profile along the y-axis as a function of the gate voltage V_{SG}, used to define the quasi-1D conductor. By making the voltage V_{SG} more negative, the electron density at the 2DEG is reduced until the point where it gets completely depleted.

The renormalised velocities derived from the simulation will be presented together with our experimental results in chapter 4.

2.3 Conclusion

In this chapter, we have outlined the theoretical description of the plasmon, whereby using a semi-classical theory, we calculate the renormalised velocity of the 2D plasmon. We showed how it is possible to derive the same result for a quasi-1D system. Then, we have used the expression of the velocity renormalisation for a system composed of two coupled channels of conductance. The coupling is mediated by Coulomb interaction. Consequently, the coupled system has new eigenmodes, one which propagates with increased velocity, and it is called the (fast) charge mode. The other mode is practically chargeless, and for this reason, it is called the neutral mode. The velocity of the neutral mode is not modified by the Coulomb interactions. Then, to find accurately the potential-filled by the electrons in the 2DEG, we have described a self-consistent set of equations. This problem consists of solving the electrostatics-quantum-mechanics equations iteratively to find the correct electron density. The solution of the self-consistent problem allows the calculation of the renormalised velocities, which can be compared with experimental results.

CHAPTER 3

Experimental set-up and technical specifications

In this chapter, we will discuss the technical details about the main experiment that I have performed during this PhD work. We present the main experimental results in the next chapter. Here, we introduce the time-resolved measurements to familiarize the reader with our experimental procedures. We also discuss the experimental set-up and the sample fabrication of an ongoing experiment.

To perform experiments involving quantum circuits is a challenging task. One crucial requirement that needs to be fulfilled is to have an experimental set-up that adds as low noise as possible since the signal of interest is very small. We also need to work at low temperatures, to avoid thermal fluctuations to wash out the quantum effects of interest.

We have a powerful dilution refrigerator available in our lab (1 mW of cooling power at 100 mK), where we performed all the measurements described in this thesis. The dilution refrigerator is a cryogenic device that uses the properties of He-3 and He-4. It is possible to reach temperatures in the order of a few mK. For further details concerning the operation principle of a dilution refrigerator, we address the reader to the following reference [121].

From experiment to experiment, we are increasing the complexity of our samples, which demands more and more low frequency and high-frequency connections going from room temperature until the sample. The challenge is to add as many lines as possible, without bringing too much heat to the sample stage and to keep the base temperature of the fridge as low as possible. It is vital to find the best trade-off between electrical conductivity - to be enhanced - and thermal conductivity - to be minimised. Another critical issue is how we thermally anchor each line at different stages of the refrigerator. We describe in this chapter all the tricky details for the DC and RF lines.

Let us start by setting our goals. We want to characterise the propagation of an electronic excitation in a coherent quantum conductor. To address this problem, we create a long quasi-one-dimensional electronic waveguide which will allow us to measure the propagation velocity of an electron wave packet. To do so, we place three probes along the electronic waveguide (see figure 3.1) which allow us to measure the arrival time of the electronic wave packet. From these measurements, we will be able to determine the propagation speed of the wave packet, and as we will see, this will give us a deep insight into the underlying physics.

First, we will concentrate on the nano-fabrication of our samples. In particular, we will discuss the design of two different samples which have been fabricated for our experiments. This is followed by a presentation of the experimental set-up and the description of the RF electronics equipment. Finally, we will focus on the technical details of the time-resolved

measurements and their calibration.

3.1 Characterising the dynamics of a Voltage pulse in a coherent quantum conductor

The electronic waveguide used to characterise the propagation of an electronic excitation is presented in figure 3.1. On the left part, the square with a cross represents the ohmic contact of a size of 10 µm× 10 µm, where we can create an electronic excitation in the two-dimensional electron gas. Two gates are used to guide the excitation towards an electron waveguide as adiabatic as possible. This waveguide, or in other words, this quasi-1D quantum conductor is defined by two, long, parallel gates of a total length of 65 µm and a width of 1 µm.

Along the quasi-1D conductor, we have placed three quantum point contacts (QPC_1, QPC_2 and QPC_3), which can be operated as fast ON/OFF switches as they are connected to high bandwidth bias tees. We have placed an additional QPC at the entrance of our waveguide. This QPC (QPC_0) is used to select a specific single-particle channel, but cannot be operated as a fast switch, due to the limited number of RF lines.

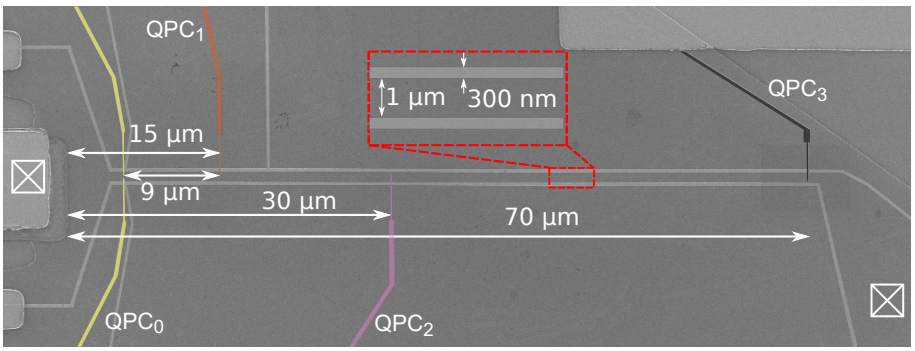

Figure 3.1: Sample used to perform the time-resolved measurements. Scanning electron microscope image of the sample. The light gray lines corresponds to the electrostatic gates. The coloured gates in yellow, brown, purple and black represent to the QPC_0, QPC_1, QPC_2 and QPC_3, respectively. The crossed squares represent the ohmic contacts, used as source (left) and drain (right).

The distances displayed in figure 3.1 are measured from the edge of the ohmic contact until the QPCs. For the data treatment, we considered that the excitation is created at the middle of the ohmic contact, that is around 5 µm from the edge. The gates that are not coloured (light grey) are used to control the confinement in the quasi-1D conductor. On the right, we have another square with a cross, that represents the ohmic contact used to collect the current from the 2DEG and it is measured across a 10 kΩ resistor [1]. The characterisation of the electron propagation along this quasi-1D conductor is the core of my PhD thesis. To be able to study the time-of-flight of the electron wave packets, we had to develop an experimental set-up with an extremely good time control due to their fast propagation speed. In the course of my PhD, I have reached state-of-the-art in time-resolution with a time control within the range of a picosecond, as we will discuss

1 Reference number: ERA6ARW103V

later.

3.2 Determining the coherence of a quantum conductor at zero magnetic field

During my PhD, I have also fabricated an interferometer to investigate the coherence length of single-electron excitation in our system. The interferometer is presented in figure 3.2. The idea is to create the electronic excitation and guide it into one of the waveguides. Let us consider the excitation is on the upper (lower) conductor, and we consider this as the state $|0\rangle(|1\rangle)$. These two conductors are connected via a tunnel barrier, used to control the coupling between the upper and the lower conductor. As the electron propagates over the conductor, it has a probability to tunnel to the other waveguide. Considering the Hamiltonian of the system, in the presence of the tunnel coupling, this system has new eigenstates. These new eigenstates are the symmetric $\frac{|0\rangle+|1\rangle}{\sqrt{2}}$ and anti-symmetric $\frac{|0\rangle-|1\rangle}{\sqrt{2}}$, that travel at different velocities, giving rise to tunnelling oscillations, as described in appendix B. This design could also be used to perform spectroscopy of the flying electron, following a theoretical proposal [79].

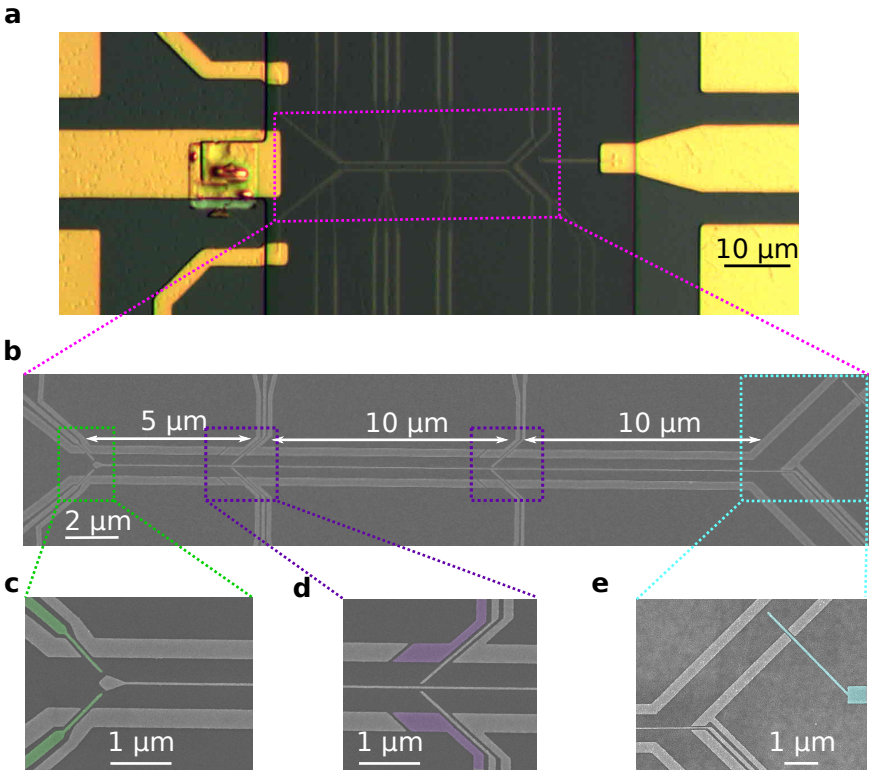

Figure 3.2: Design of the sample made to measure coherent oscillations. a, Optical microscope picture of the fabricated sample. The square with some bubbles on the left is the ohmic contact, where we create an excitation in the 2DEG. **b,** Scanning Electron Microscopy (SEM) picture of the entire sample. SEM zoom on the entrance section **c**, middle section **d** and exit section **e** of the quantum conductor.

We show the optical microscope and scanning electron microscope (SEM) images of the fabricated sample in figure 3.2. On the left of figure 3.2**a**, one can recognise the ohmic contact (the gold square with bubbles). This contact is where we can inject a single-electron excitation into the 2DEG. The excitation is guided towards the quasi-1D conductor via electrostatic gates. In the SEM image, figure 3.2**b**, we show the complete tunnel-coupled wire (TCW) characterised by a very thin gate ($< 50\,\text{nm}$), going from the left all the way to the right. This TCW gate is used to divide the quantum conductor into two different electron waveguides (upper and lower). As these waveguides are spatially very close, there is a tunnel-coupling generated, which can be controlled by varying the voltage applied to the TCW gate. At the entrance of the TCW, we have added two additional gates (in green, zoom in figure **c**) in order to be able to guide the electron excitation either in the upper or lower quantum conductor. Four additional gates have been added (in purple, see figure 3.2**d**) in order to be able to measure the conductance oscillations at different lengths. In figure 3.2**e**, we show a zoom of the exit section of the sample. A QPC (in light blue) is connected to the upper output of the electron waveguide, in order to perform a time-resolved measurement of the injected pulses. These measurements are presently ongoing and should allow us to determine the coherence length of the quantum conductor.

3.3 Sample fabrication

Before entering into any fabrication detail, it is important to note that, during this PhD work, we have worked with two different samples. The first one, which I was responsible for the measurements, was fabricated by Grégoire Roussely. We will discuss the results of these measurements in chapter 4. I was responsible for the fabrication of the sample designed to characterise the coherence length in our electron waveguides.

Now that we have set the direction of the measurements that we want to do let us detail the sample fabrication steps. Let us first discuss the constraints of our sample design. To minimise the distortion of the pulses inside the 2DEG, we place the ohmic contact as close as possible to the quasi-1D structures. Since we will use ultra-high frequency signals, to reduce the reflections of the signal going into the sample, it is important to have an impedance matching from the output of the signal generators until the ohmic contact used to create the excitation into the 2DEG. For this purpose, we patterned a coplanar waveguide (CPW) going from the edge of the sample, until the inner structure (the ohmic contact). We have another one connected to the QPC. The CPW on the right of figure 3.2**a** is connected to the light blue QPC of figure 3.2**e**. The figure 3.3 is a photo taken with a microscope of the sample made to measure coherent oscillations. For the sample used to perform time-resolved measurements, we have in total four CPW, one going to the ohmic contact and the other three to different QPCs (QPC_1, QPC_2, QPC_3). We use a technique that is known as tapered [122], to reduce the sizes of the CPW but keeping the impedance matching, as shown in figure 3.3. The design of the CPW was realised with the transmission line calculator TX-line.

Let us discuss the main steps done in the clean room to arrive at the final sample, as shown in figure 3.2. The starting point is a high-mobility heterostructure of GaAs/AlGaAs wafer. The method to realise such high-quality 2DEG is molecular beam epitaxy (MBE). Our collaborator Prof. Andreas Wieck provides the HEMT used in our fabrication. Despite

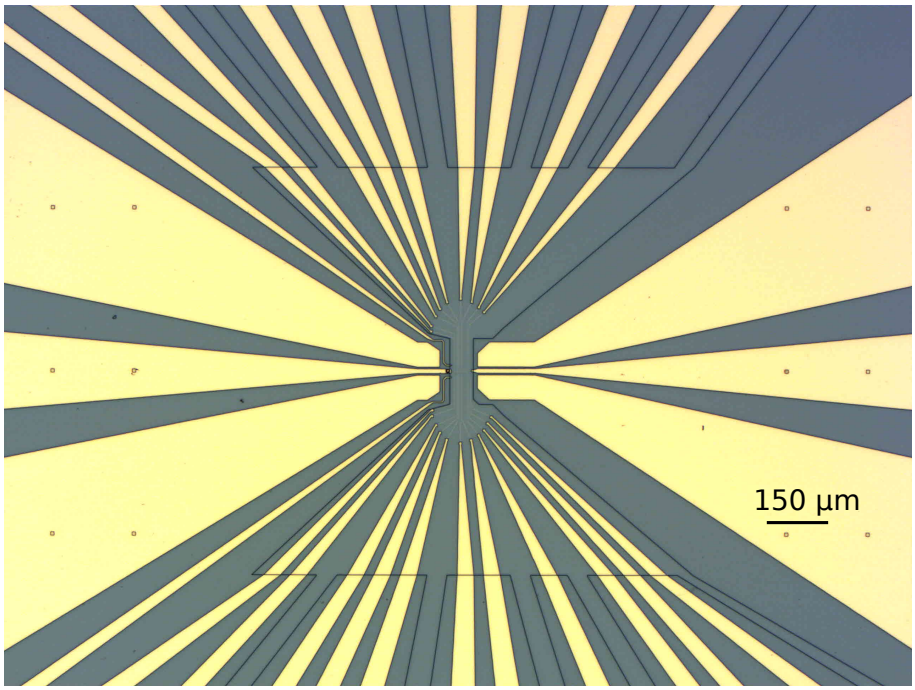

Figure 3.3: Tapered coplanar waveguide. Microscopic picture of the sample presented in 3.2. The big gates on the left and the right part correspond to the coplanar waveguides, and the reduction in size when going from the edges to the centre of the sample is known as tapered.

that step, the entire fabrication is realised in the in-house clean room "Nanofab" of the Neel Institute.

The main steps of the fabrication are:

1. First, we cut the wafer to the desirable size, using a scriber to cleave and break it.
2. Prepare the 'mesa' with wet etching, where the 2DEG is removed from all the places that are not needed. The etching is done using a Piranha reaction (H_2SO_4:H_2O_2:H_2O with concentrations 5:1:25). The places to be etched are defined via optical lithography, using S1805 as the optical resist.
3. We define the position of the ohmic contacts using optical lithography. We use S1818 as the optical resist. Then, we evaporate 5 nm Ni + 60 nm Ge + 120 nm Au + 10 nm Ni + 100 nm Au. The lift-off is done by leaving the sample in a beaker with acetone, waiting a few hours. The sample is annealed at 450 °C for one minute, to make the evaporated material diffuse into the heterostructure.
4. We add alignment marks using optical lithography. These markers are used to perform the electron beam lithography. Again, we use the optical resist S1805. We deposit 20 nm Ti + 100 nm Au. The lift-off is done as in the previous item.
5. The inner structure of the sample is patterned using e-beam lithography. The resist used is PMMA 2%. After the lithography, we deposit 4 nm Ti +13 nm Au. The

lift-off is done with acetone, waiting at least 12 h.

6. The last step is to realize the connection between the contacts and the inner structure. To do this, we perform another laser lithography with the same parameters as in step 4.

3.4 Experimental set-up

In this section we will describe the experimental set-up suitable for our measurement. We will start by presenting the cold finger, that is the part anchored to the coldest stage of our dilution refrigerator.

3.4.1 Cold finger

The cold finger used for the time of flight measurements has been described in detail in ref. [123]. Here, we describe the new cold finger which has been developed during my thesis in order to allow to apply a magnetic field to the sample. This was not possible with the old cold finger, as illustrated in the appendix C. With the new cold finger, we also increased the number of DC lines and improved the thermal anchoring of the DC and RF lines significantly.

The new cold finger is made from oxygen-free high thermal conductivity copper and gold-plated to avoid oxidation. The cold finger is thermally anchored at the mixing chamber (MC). On the bottom part, we install the sample holder, where we can contact the chip carrier with 32 DC lines coming from the bottom. On the top, we can contact the sample with the RF lines, via 4 mini-SMP connectors. In figure 3.4, we show the cold finger and the electrical connections to the sample.

Compared to the old cold finger, several improvements have been made: (i) addition of RC filters at the MC stage, (ii) increase of the number of DC lines from 24 to 32, (iii) 2 low capacitance coax for future usage in combination with a cold pre-amplifier.

3.4.2 Chip carrier

The chip carrier is composed of a PCB made with the material R03010 (dielectric constant $\varepsilon_r \approx 10.2$ [124]), and which can accommodate 4 RF lines. The PCB is designed to have the DC lines and the RF lines on the opposite side of the PCB to reduce cross-talk. The DC lines of the PCB are connected to the cold finger via gold pins using a spring mechanism. Four mini-SMP connectors that are fixed using a solder paste, Loctite HF 212 0307 and an alignment jig in order to precisely position them. The whole is pre-heated for 120 s at 160 °C, then heating for 300 s at 300 °C. This procedure is important to ensure perfect alignment with the shield that goes on the top of the sample holder, as shown in figure 3.4**b**. The sample chip is glued with Varnish (GE 7031) in the middle of the chip carrier (grey square). This hole has been designed to have a depth of $\approx 550\,\mu m$ such that the surface of the PCB and sample chip are aligned, hence minimising the length of the bonding wires.

The sample is bonded with 25 µm thick gold wires. For the CPW, several bonding wires are connected, to optimise the transmission. In figure 3.5**b**, we show the backside of the PCB. The circles are used to make the electric connection with the pins shown in figure 3.5**c**. These pins are part of a spring-load mechanism, in order to have a good mechanical

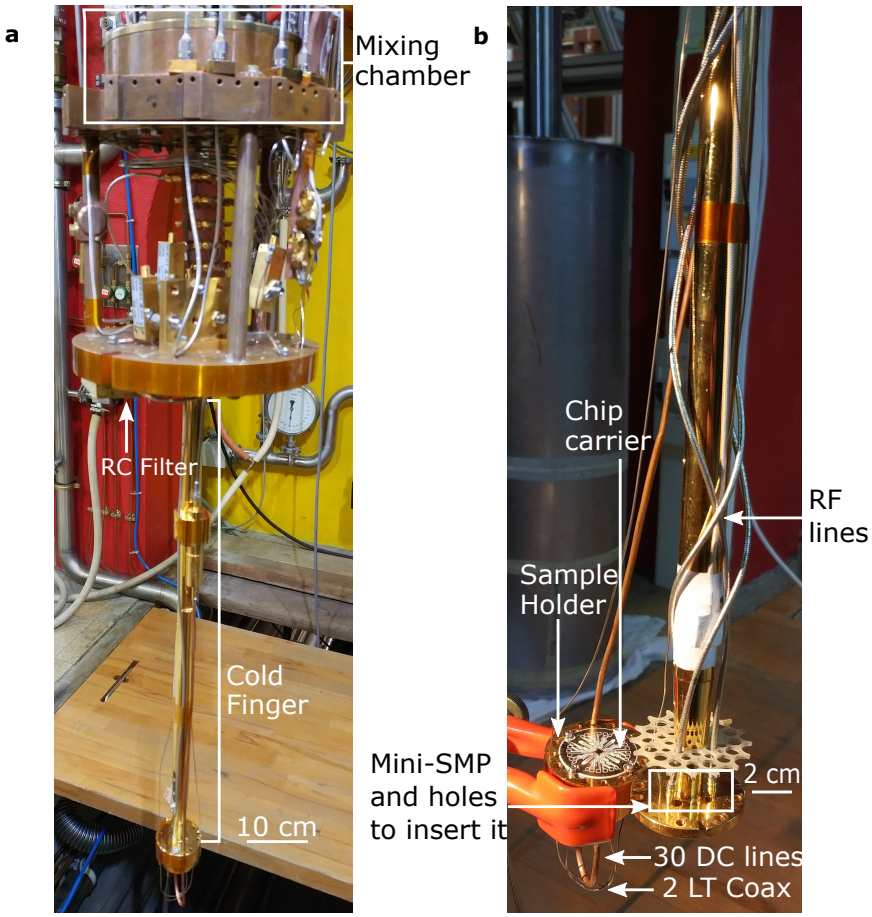

Figure 3.4: New cold finger. a, Photo of the cold finger attached to the mixing chamber. On the left side, it is shown the RC filter, where the 30 DC lines are filtered. **b,** Bottom part of the cold finger. The copper capillary contains the 30 DC lines that are connected from the bottom to the sample holder. On the right side are the RF lines and the mini-SMP connectors. The PCB chip carrier containing the sample chip in connected to the cold finger.

contact. The prolongations of the circles at the chip carrier allow for surface mount device (SMD) electrical components to be added. We usually add 10 kΩ resistors to ground to convert the current into voltage and perform lock-in measurements, as will be discussed later in this chapter.

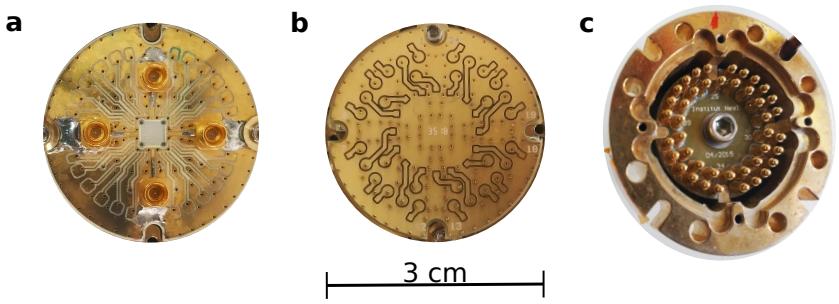

Figure 3.5: Chip carrier. **a,** Top part of the chip carrier. **b,** Bottom part of the chip carrier. **c,** Bottom part of the cold finger. The golden pins make the connection between the DC lines and the chip carrier through a spring mechanism.

3.4.3 Electronic set-up

Let us now discuss the electronic set-up. We will describe the lines used to connect to the sample (DC and RF) and also the equipment used to create ultra-fast voltage pulses.

The measurements presented in the next chapter have been obtained with the experimental set-up described in ref. [123]. We have spent a significant amount of time improving the set-up for the next experiment on quantum coherence effects, and we will describe the new set-up in the following.

DC lines

To polarise the gates of our sample, or to apply a bias, we need to have low-frequency lines going from room temperature until the sample level. Again, we need to care about the amount of heat that we bring inside the dilution refrigerator. As good electric conductors are usually also good thermal conductors, we use a high resistive material to make the connection between room temperature and the sample. We use Constantan wires with the diameter of 125 µm. These lines have around 60 Ω per meter - the resistance from the top of the refrigerator until the mixing chamber is around 130 Ω. We use a technique developed in our lab [125] to filter the radiation in these lines. First, we twist pairs of constantan wires, and then coat these wires with Eccosorb® CRS 117 and insert them into a Cu/Ni capillary. The Eccosorb® is a silicone rubber material that is magnetically loaded, working as a high-frequency absorber. The advantage of this technique is the high number of lines in minimal space. We have 30 DC lines going until the mixing chamber in a capillary of just 3 mm of diameter.

The Cu/Ni capillary is anchored at the different stages of the dilution refrigerator using a highly conductive Copper braid using soft solder. At the mixing chamber the wires are connected to a RC filter in order to ensure thermal anchor of the wires. A 25 µm thick Kapton sheet covered with gold strips are glued with silver epoxy (EPO-TEK H 20E) into an RF shielded copper housing. The whole set-up is made in such a way that the RC filter is dismountable. For this, RF shielded connectors (30 pins) have been especially prepared to improve the RF shielding as well as thermal anchoring. The connections between the RC filter to the cold finger are made from Copper wires (diam. 100 µm).

For the RC filter, one has to make sure that the surface-mounted components (SMD) do not change their electronic values with temperature. To avoid this problem, we realized a test at low temperatures to check that all DC measurement lines are working with the proper filtering. The resistor used and tested was the Panasonic 3 of 1.0 kΩ and the capacitor was a surface-mount multilayer ceramic chip of 47 nF[1].

The transmission of the RC filter in series with the DC lines is plotted in figure 3.6. The blue data in fig. 3.6**a** correspond to the transmission of the RC filter only. We have used the signal analyser HP 35670A, which works from 50 Hz until 50 kHz to measure this data. The dashed grey lines correspond to the -3 dB point, which is known as the cut-off frequency ($f_c = 1/(2\pi RC) = 3.4$ kHz). At this frequency, the power of the transmitted signal is reduced by half, consistent with our measurements.

Furthermore, we have characterised the transmission of the DC line in series with an RC filter using higher frequencies, using the vector network analyser R&S®ZVL6 (VNA). This machine works from 10 kHz until 6 GHz. However, we measure the transmission over a slightly different circuit, composed of the Constantan immersed in Eccosorb® in series with the resistor of the filter, and the capacitor in parallel with an internal resistor in the VNA of 50 Ω going to ground. In figure 3.6**b**, we plot the measured transmission of the discussed circuit (blue circles). We also plot the expected transmission for this circuit (red line), whose electronic model is discussed in detail in appendix I. We observe that, for high frequencies, the measured transmission is lower than our expectation. The reason is the effect of the filter formed by the Constantan within the Eccosorb® at high frequencies, which is not considered in our model.

Control of the Schottky gates

With the ever-increasing number of electrostatic gates for our quantum devices, a suitable and very stable voltage control system is necessary. We use a home-made system containing 40 digital to analogue converters (DAC), based on the chip LTC2604, within a low-noise amplification before the output. The typical white noise is $\approx 25\,\mathrm{nVHz}^{-1/2}$ [123]. The DACs are optically isolated to avoid ground loops and can output DC voltages from -5 V to +5 V with 16-bits of resolution. The voltage rise time is limited to 300 mV /µs. We can also generate a low-frequency square signal often used to test the sample. The maestro of our experimental is the FPGA (field-programmable gate arrays) - we are using the single-board RIO 9612, [2] which allow us to control and sweep the voltage of the DACs. The time required to address each DAC is 16 µs. We can also use the FPGA to trigger other instruments in a synchronized way.

1 Reference of the capacitor:C0805C473J3GACTU.
2 Specifications: CPU 400 MHz, 128 MB DRAM and 256 MB of storage.

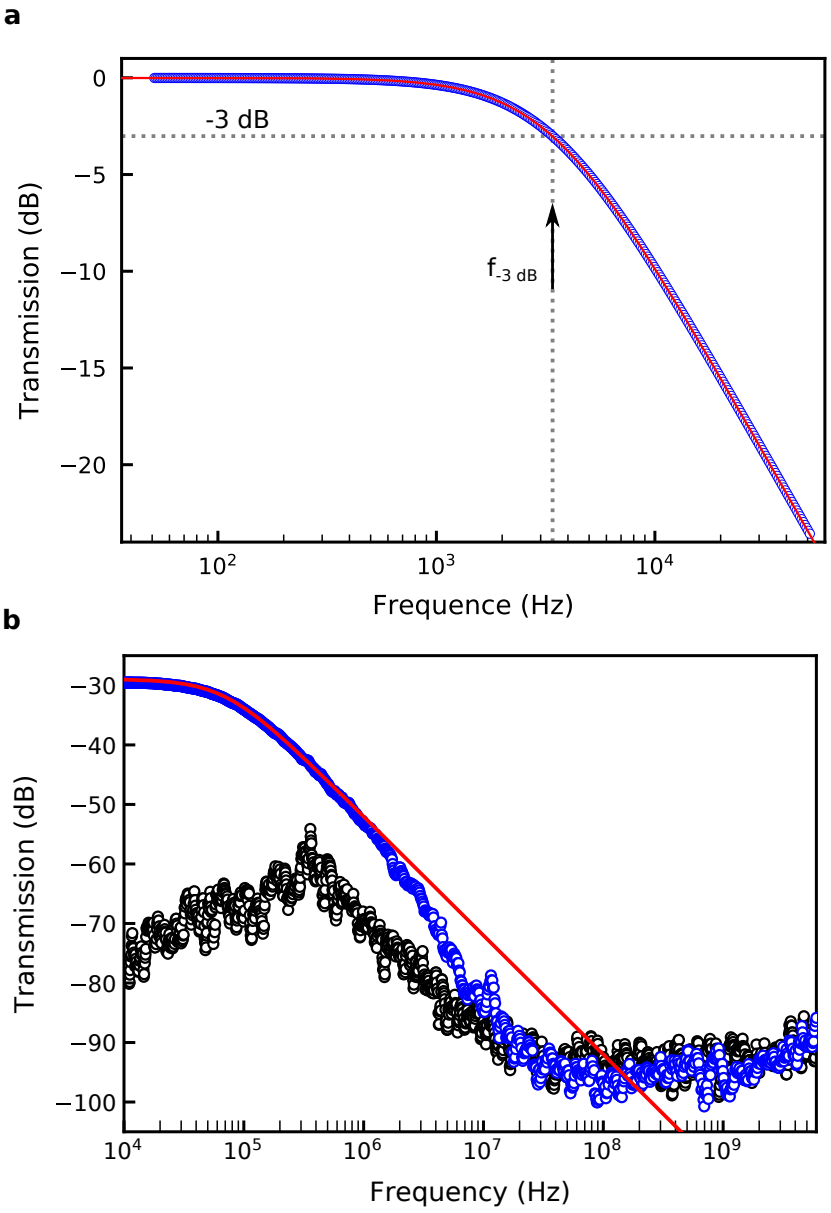

Figure 3.6: Transmission of the RC filter. a, Transmission of a home-made RC filter as a function of the frequency. The blue data corresponds to the measured transmission. The dashed grey line correspond to the value of -3 dB, which is at the frequency of 3.4 kHz. The red line correspond to theoretical expectation of the RC filter. **b,** Transmission of the constantan wire immersed in Eccosorb® in series with RC filter, measured from 10 kHz until 6 GHz with VNA R&S®ZVL6. The blue circles are the measured transmission. The black circles are the noise level of the equipment. The red line correspond to the theoretical expectation of the circuit, as described in appendix I

RF lines

Now that we described all the DC part of our set-up, let us focus on the most challenging parts of our experiments, the demand for ultra-high frequency signals. It is imperative to be able to apply an ultra-short pulse to the sample level to be able to inject a single electron directly to the Fermi sea, which means that we need to:

1. Have an excellent signal generator to create this ultra-short pulse.
2. Make the pulse go from room temperature until the sample (at few mK) with RF cables of a length of roughly 1.8 m, without significant distortion.
3. Have a proper attenuation, reducing the thermal noise coming from room temperature, such that it does not affect the electronic temperature of the sample, which can induce broad band voltage fluctuations [126]. At the same time, we must limit the electronic power dissipated at each stage of the refrigerator, such that we do not increase the base temperature of the experiment.

To address items number 2 and 3, we dedicated a considerable amount of time improving the RF lines in our set-up, to promote a proper thermalisation and also to increase the bandwidth of the lines. At the beginning of this thesis, the RF lines were thermalised only at the 1 K stage and the mixing chamber. The connection between 1 K and the mixing chamber was made with Nb coax [123].

Presently we have 4 RF lines equipped with K-connectors going from RT down to the mixing chamber (MC). The replacement of the SMA connectors by the K-connectors has improved considerably the strong attenuation above 18 GHz due to these SMA connectors [127]. The RF-lines are made out of silver-plated stainless steel for the centre conductor and stainless steel for the outer conductor. They are thermally anchored through screw-type feedthroughs and attenuators with K connectors at the 1K stage (1.5 K), the cold plate (200mK) as well as at the mixing chamber (20 mK). For future experiments, we installed four additional RF lines with the regular SMA connectors. The transmissions at room temperatures and at 4 K are shown in figure 3.7.

The thermal noise appears due to the agitation of electrons inside a conductor, first described by Johnson [128] and explained by Nyquist [129] where the generated noise is proportional to the temperature of the device. The power spectral density describes the generalized noise derived in Nyquist's original paper, and it is equal to

$$S(\nu, T) = 4.k_B.T.\eta(\nu)|\mathrm{Re}(Z(\nu))|, \tag{3.1}$$

where T is temperature, ν is the frequency, $Z(\nu)$ is the impedance of the considered circuit and $\eta(\nu)$ is equal to

$$\eta(\nu) = \frac{\frac{h.\nu}{k_B.T}}{e^{\frac{h.\nu}{k_B.T}} - 1}. \tag{3.2}$$

This formula corresponds to the photon distribution number times the energy of one photon, which is the photon distribution over energy. Simplifying the system and considering

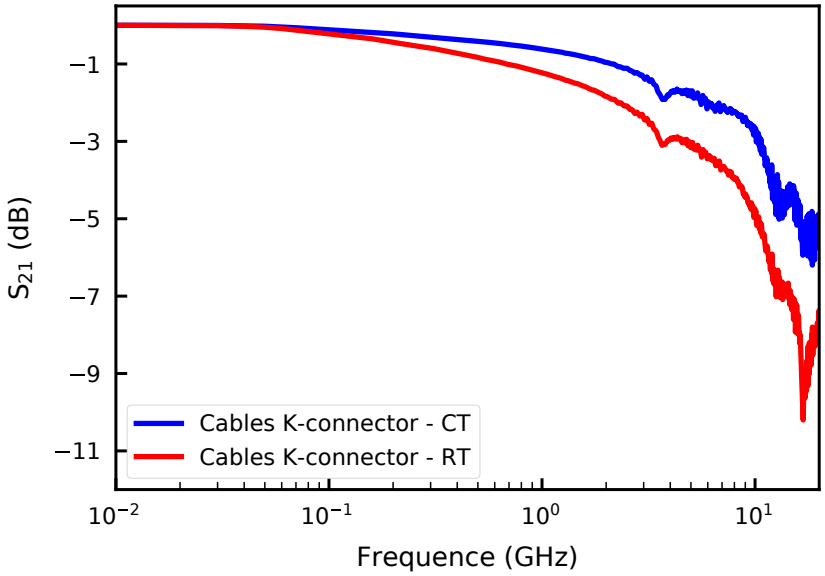

Figure 3.7: Transmission of the RF lines. Transmission per meter of the RF cables at room temperature (red) and 4.2 K (blue). The dip in the transmission around 17.5 GHz is due to the presence of one SMA connector that was used as replacement for one broken K-connector.

the noise added by each attenuator as a 50 Ω load, the added noise is

$$\begin{aligned} S_{all}(\nu) = S(\nu, 20\,\mathrm{mK}) + 10^{\text{Attenuation Mixing Chamber}/10} \times \\ \times \left[S(\nu, 200\,\mathrm{mK}) + 10^{\text{Attenuation Cold Plate}/10} \times \right. \\ \left. \times \left(S(\nu,1\,\mathrm{K}) + 10^{\text{Attenuation 1K pot}/10} \times S(\nu,300\,\mathrm{K})\right)\right]. \end{aligned} \tag{3.3}$$

The outcome of equation 3.3 is: it is better to have higher attenuation at the lowest temperature stage since we would add less noise with the attenuator. However, we should also think about the cooling power capacity of the refrigerator. To restrict the electric power going down the lines in the fridge, we added 10 dB at the 1 K pot level and at the cold plate. At the mixing chamber, we added another 20 dB for the line going to the ohmic contact. For the lines going to the QPCs, we have an attenuation of 6 dB at the 1 K stage and 10 dB at the mixing chamber (MC).

The RF signal is fed through a high bandwidth bias tee (SHF BT 45) in order to be able to inject also DC signal besides the RF signal. From the mixing chamber (MC), via the bias tee down to the samples stage we use a semi-flexible copper coax connected to mini SMP connectors which have a low insertion of loss $< 0.1\sqrt{f(\mathrm{GHz})}$ dB [130] and high bandwidth (DC until 65 GHz). The mini-SMP plug fixed on the chip carrier is connected to a coplanar waveguide (CPW), such that we have 50 ohms impedance matching. The

geometry of the CPW, together with the dielectric constant of the material defines the impedance. We have chosen for the chip carrier a material with a dielectric constant close to that of GaAs ($\epsilon_r \approx 12.9$). This value should not vary much with frequency and with temperature. The material for the substrate of the chip carrier is Rogers R03010 with a dielectric constant of $\epsilon_r \approx 10.2$ at 10 GHz [124]. We also added coplanar waveguides on the sample for the RF connections, which are 50 ohms impedance matched until the inner structure of our sample.

Creation of fast pulses

To create ultrafast voltage pulses, we have two different devices at hand. The first one is a commercial arbitrary wave generation (AWG, Tektronix 7122B) of 24 GS/s (12 GS/s) depending on whether one or two output channels are used. Set at 12 GS/s, we can generate a voltage pulse with a full width at half maximum (FWHM) of $\approx$ 83 ps with a maximum amplitude of 500 mV, as shown in figure 3.8.

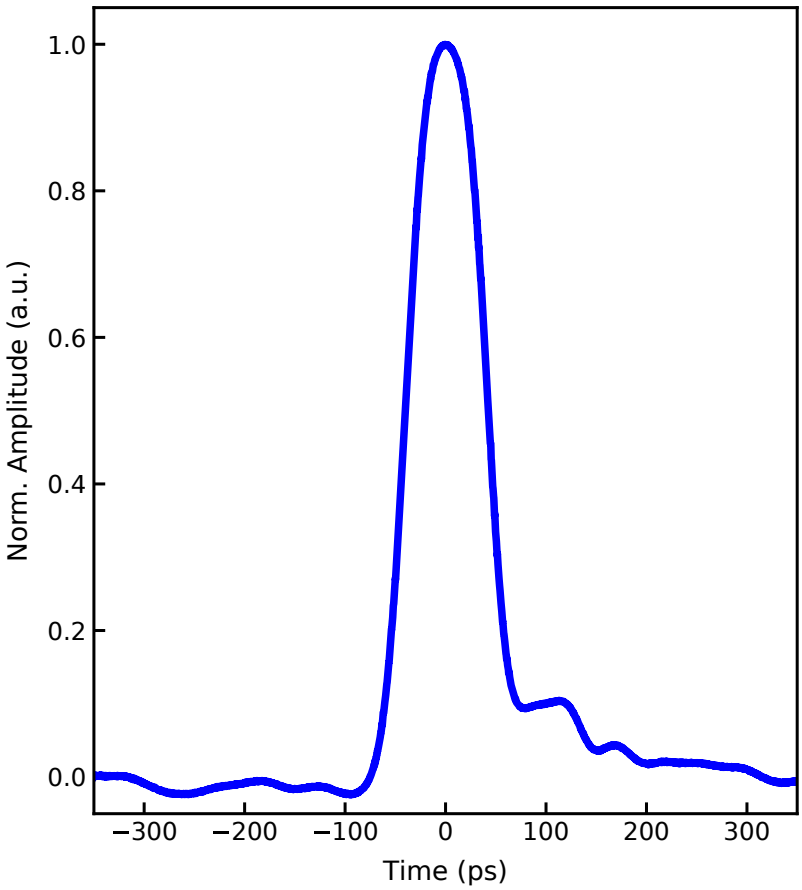

Figure 3.8: Voltage pulse created with the AWG. Shortest pulse created with the AWG, the AWG is set to work at 12 GS/s. The full width of half maximum is in the order of 80 ps.

For the experiment, we create a 1D array where we program the pulse pattern by setting the target voltage as a function of time. The time separation between the points is 83 ps. This array is created with a python script and is sent to the AWG via ethernet connection.

We can define two different waveforms for the two different output channels. Usually, we use one to create the few-electron excitation, and the other one to control a fast switch, allowing us to do time-resolved measurements of the created excitation, as we will describe in section 3.5. We can also generate modulated signals using the waveform array. For our time-resolved measurements we performed a modulation technique combined with a lock-in measurement. An example of waveform and modulation created with the AWG is depicted in figure 3.9.

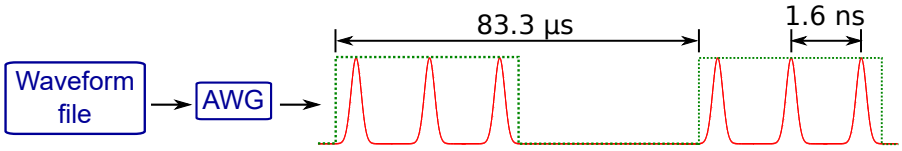

Figure 3.9: Pulse generation. Schematic of the voltage pulses created by the AWG. The AWG tries to follow the waveform file containing the voltages at different times. The right side of the figure represents the AWG output, where the Gaussian pulses are separated by 1.6 ns. The square signal at the top of the Gaussian pulses represents the square modulation of 12 kHz.

To perform the time-resolved measurements, we add a square modulation to the signal used to create the excitations, as shown in figure 3.9. The modulation frequency used is 12 kHz, because this is the best compromise between the bandwidth of the bias tee and the room temperature amplifier [123].

We show one example of a time-resolved measurement of two successive pulses in figure 3.10. We observe a temporal separation of the pulses of 1.6 ns, as discussed in figure 3.9.

One useful feature of this AWG is the possibility to add a delay between the two output channels of +-100 ps with a resolution of 1 ps. We can also create different waveforms, with a fixed separation of 83 ps. Creating different waveforms and using the tunable delay, we have precise control of the pulses in the time domain.

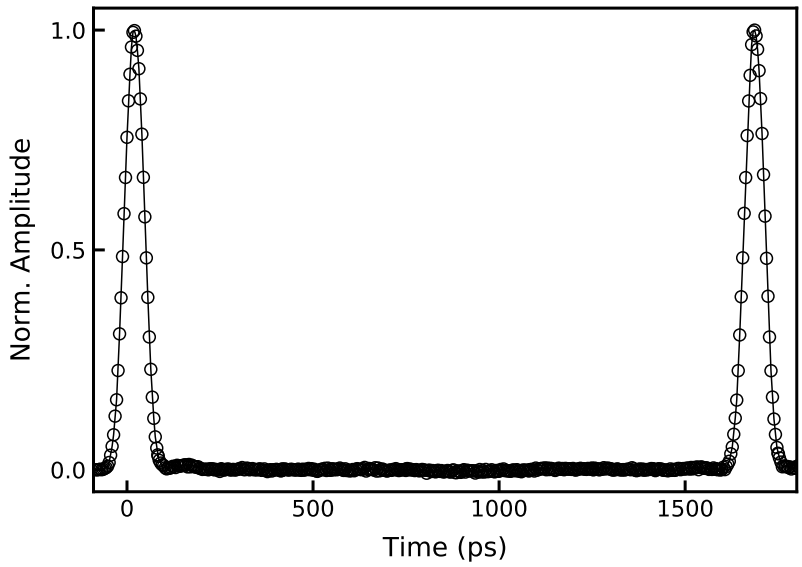

Figure 3.10: Voltage pulse injected at the ohmic contact. Pulse repetition resolved at the sample. The pulses are spaced by 1.66 ns (600 MHz repetition frequency).

Pulse box

We also used a home-made system to create our ultrafast pulses, inspired by the source developed in Glattli's group, as described in [131]. The principle is quite simple. We combine a few harmonics to engineering the desired pulse, in our case, a Lorentzian pulse. The sinusoidal harmonics are created from two different sources, at 6 GHz and of 18 GHz, which corresponds to the first and the third harmonic. The signal coming from the first harmonic is split into two. One branch is connected to a phase shifter followed by a voltage variable attenuator. The other branch is connected to a frequency doubler, used to generate the second harmonic 12 GHz. This signal is split again, and passed through another frequency doubler to achieve the 4th harmonics 24 GHz. The amplitudes and phases of all harmonics are controlled with variable attenuators and phase shifters except the one of the forth harmonics which sets the reference phase. The amplitude of the 3rd harmonics can be controlled by the continuous wave source.

We present the schematic of the home-made system in figure 3.11. In the end, we have 8 parameters to control: The amplitude of the sources of 6 GHz and 18 GHz, the attenuation for the frequencies 6, 12 and 24 GHz, the phase for the frequencies 6, 12, 18 GHz.

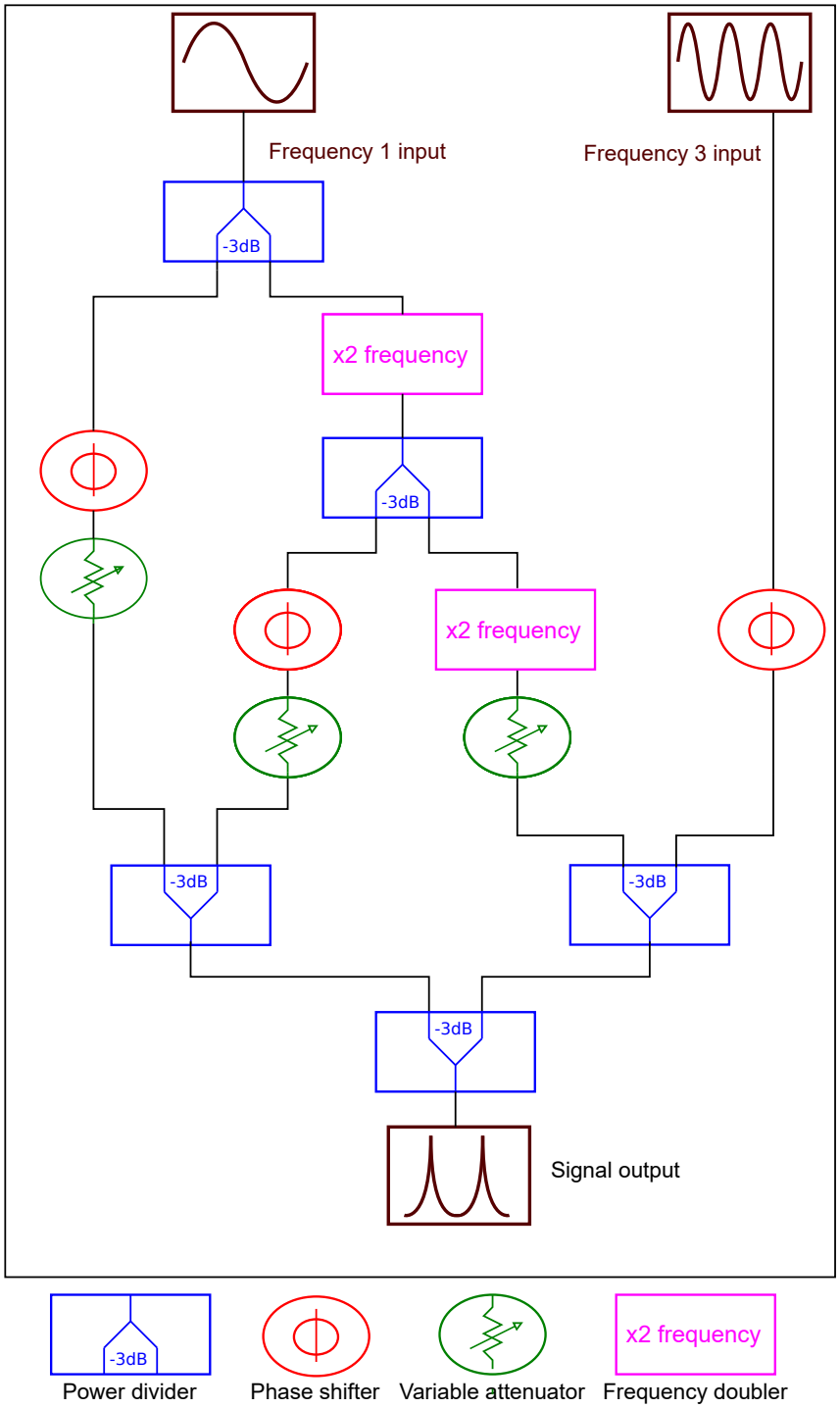

Figure 3.11: Ultra-fast radiofrequency engineering. Schematic of the components used to generate Lorentzian-shaped pulses using 4 frequency harmonics, with the possibility to change attenuation and phases electronically.

The shape of the outcoming pulse will depend on the amplitude of the different harmonics. For example, by setting all harmonics with the same amplitude and phase, the resulting voltage pulse has the shortest possible widths (FWHM $\approx 24\,\mathrm{ps}$), as shown in figure 3.12 **a,b**. However, the pulse is accompanied by several wiggles in the wings due to the limited number of harmonics. Differently, we can set the amplitudes in such a way that the decay of the amplitude is exponential, as shown in figure 3.12 **c**. In this case, one obtains a pulse of Lorentzian shape, as shown in figure 3.12 **d**. The FWHM is $\approx 57\,\mathrm{ps}$.

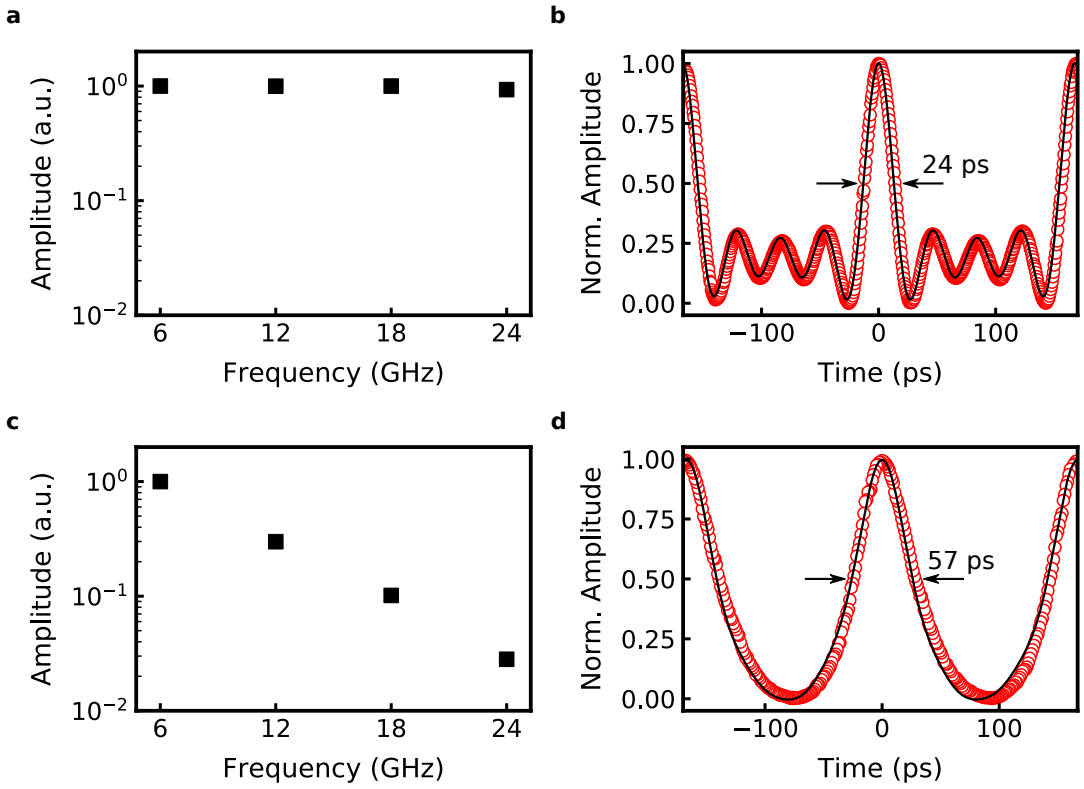

Figure 3.12: Signal generation with the pulse box. **a,** Amplitude of the 4 different harmonics measured on a sample oscilloscope (WaveExpert 100H) to obtain the minimum FWHM (delta-function-like) The black squares are the amplitudes for the different harmonics. In this case, the values are the same. **b,** The red dots are the measured signal output on a sampling oscilloscope (WaveExpert 100H) adjusting all the harmonics in phase using the amplitudes from **a**. The black line is the calculated signal, combining the four harmonics with equal amplitudes. **c,d** same as **c,d** but with the difference that the amplitudes of the harmunics decrease exponentially to generate a Lorentzian-like voltage pulse. A 57 ps pulse width is obtained for the best possible Lorentzian (no wiggles in the wings).

Setting a Lorentzian pulse at room temperature would end up with a very distorted pulse at the sample level, due to the dispersion in the RF lines. We, therefore, have to pre-compensate the individual harmonics of the voltage pulse and this is done by measuring each harmonic by time-resolved measurements on-chip, these data is shown in appendix

D. The strategy adopted to create a Lorentzian pulse at the sample level was to tune the amplitudes and phases of all harmonics and measuring the time-resolved electron wave packet. We have adopted the following procedure:

1. First, we connect the pulse box output to the oscilloscope. Then, we set all adjustable attenuators at the maximum attenuation, except the one for the 24 GHz component, set at the minimum value. We increase the power of the 6 GHz harmonic such that we observe the 24 GHz component on the oscilloscope. Then, we perform a time-resolved measurement of this harmonic on-chip to make sure that the power applied at the top of the cryostat is sufficient to be detected with our time-resolved measurement set-up.
2. We then add the 12 GHz harmonic by decreasing the attenuation of this component, and we perform a time-resolved measurement. Based on the FFT of the measured signal, we adjust the phase shifters such that these two harmonics are in-phase. We then perform another time-resolved measurement to ensure that the phases and the amplitudes are correct. We adjust the amplitudes, as shown in fig. 3.12.
3. Next, we add the fundamental harmonic of 6 GHz. We perform again a time-resolved measurement and analyse the FFT of the resolved signal. Like this, we can adjust the phase and amplitude of the first harmonic in relation to the other harmonics, as we did in step 2.
4. Last, we add the 18 GHz. This harmonic is left as the last one because it is generated by a different source and we perform a similar procedure as we did in step 3.

One inconvenient feature of this pulse box set-up is the synchronization of the reference of the generators. Even when synchronizing the references, we observe some drift between the phase of the two sources over several hours, which makes the synchronization of the phases a little tedious and does not allow for long measurements without readjusting the phases.

For the next experiments, we have started to develop a better solution to remedy this phase drifting. We now use frequency generators which are synchronized through an extremely precise clock. With this approach we have been able to generate Lorentzian voltage pulses which are very stable in time.

To perform time-resolved measurements using the pulse box, we have used a different technique to measure the current going through the sample. This time, we have measured the current flowing in the sample with a home-made current to voltage (I/V) converter with a gain of 1G (operational amplifier - TLC2201). The reason for directly measuring the current was to avoid the use of mixers or any other extra RF component needed for signal modulation. From the I/V converter, we then measure the voltage using the analogue to digital converter national instruments USB-6216 BNC.

Inducing an excitation with a capacitively coupled gate

All the measurements that we will discuss in chapter 4 were taken by injecting an excitation directly into the 2DEG, applying a voltage pulse at the ohmic contact. However, there are other possibilities to generate a short voltage pulse. In this section, we will create short voltage pulse with the sample in a different way. This time, we use the AWG not to induce a pulse directly in the 2DEG via ohmic contact, but to use the non-linearity of the conductance trace of the QPC to engineer a pulse. First, we apply a sufficiently strong negative DC voltage to the QPC, in this case QPC_1, to suppress fully the conductance and we apply a DC bias to the ohmic contact. The next step is to apply a short voltage pulse to QPC_3 which will open for a very short time scale and allows the current to pass through it for a brief time. We show in figure 3.13 the time-resolved trace of this experiment.

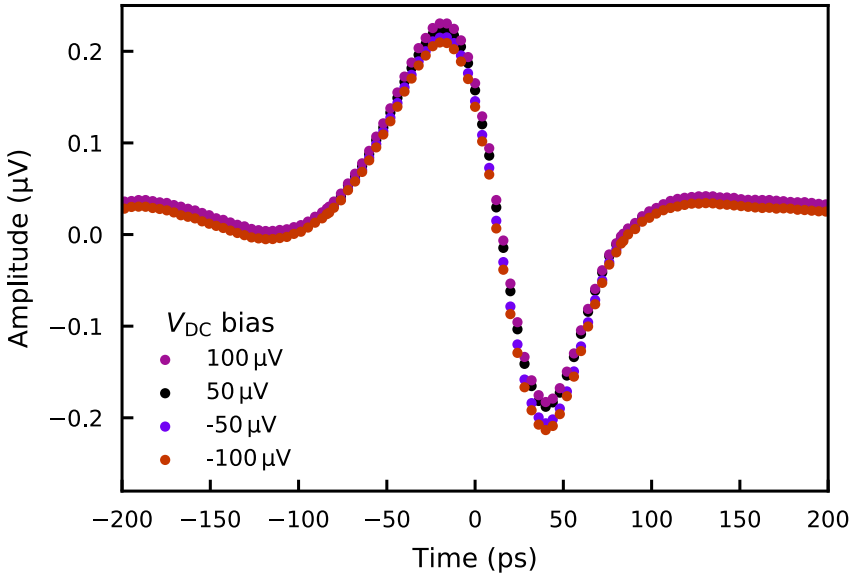

Figure 3.13: Creating pulses with the quasi-1D conductor. Time-resolved measurement of the wave packet when opening QPC_1 on a very short time scale while biasing the ohmic contact with a DC voltage. The time-resolved measurement was performed at QPC_3. Measurements were done with 4 different DC bias, 100, 50, -50 and -100 μV.

We observe that there is a small difference between the signals for different DC bias, but this is not the main effect generated. We observe a large positive and negative peak. To quantify the importance of the DC bias on the amplitude, we performed the same experiment, but this time without the DC bias. Subtracting this data, from the curves in figure 3.13, we obtain figure 3.14.

Comparing the amplitudes from figure 3.13 and 3.14, we can see the effect of the DC bias for this configuration is ten times smaller than the effect of the pulse in the gate. Even small, we can observe a voltage pulse in 3.14 generated when the QPC allows the transmission of the voltage bias for a very short time.

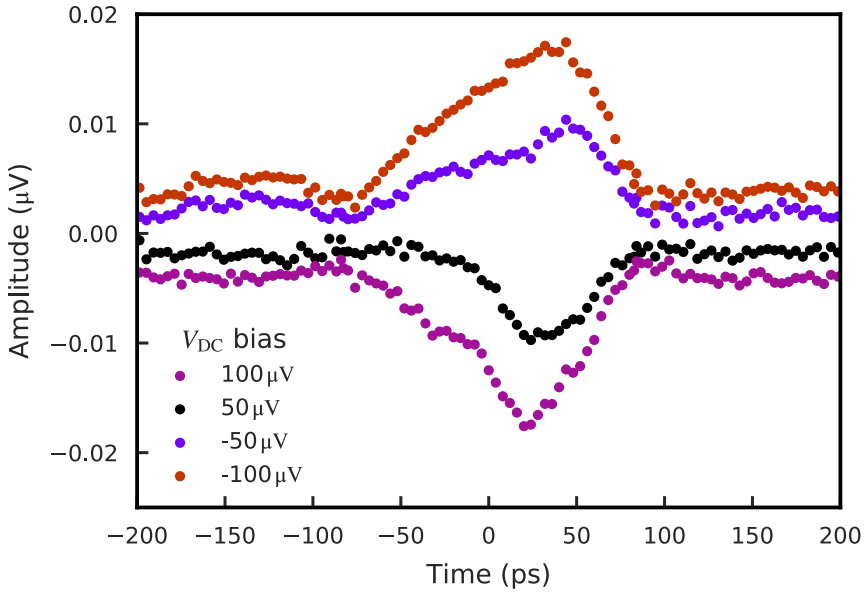

Figure 3.14: Effect of the DC bias on the creation of the pulse. Amplitude of the voltage pulse obtained by subtracting the curve measured with $V_{DC} = 0$.

To understand the measured signal shown in figure 3.13, in particular the positive and negative contribution, we have studied the effect of a pulse applied to the QPC_1 by changing the level of the depletion underneath the QPC_1 gate (V_{DC}). In other words, we are changing the electron density underneath the QPC, thus changing the quantum capacitance and measuring its impact on the resulting pulse shape, as presented in figure 3.15.

We observe that the shape of the voltage pulse is similar to the case of directly injecting the pulse in the ohmic contact when the DC voltage applied at QPC_1 is zero or small. We attribute this effect to the quantum capacitance between the QPC and the quasi-1D quantum conductor. The capacitance between the QPC and the quantum conductor in series with a 10 kΩ resistor results in a RC circuit. The role of the 10 kΩ resistor is to convert the current into a voltage which is read out with a lock-in amplifier. If the RC time is larger or on the order of the applied pulse widths, the output at the resistor will have a similar shape as the original pulse. However, if the RC time is much shorter than the pulse widths, the RC-circuit behaves as a differentiator. When we vary the DC voltage at QPC_1, we are depleting more and more the electrons underneath the gate, therefore decreasing the quantum capacitance. At the same time we are also modifying the RC time and making it much shorter than the original pulse widths ($\approx$ 80 ps).

We have measured time-resolved curves at the two limits of this RC circuit, as shown in figure 3.15. The yellow curve corresponds to the case when the QPC_1 is polarized with a small DC voltage (V_{QPC_1} =-0.29 V). The shape of the resolved pulse does not change by varying the DC voltage at QPC_1 from $V_{QPC} = 0$ to -0.29 V. Indeed, the time-resolved

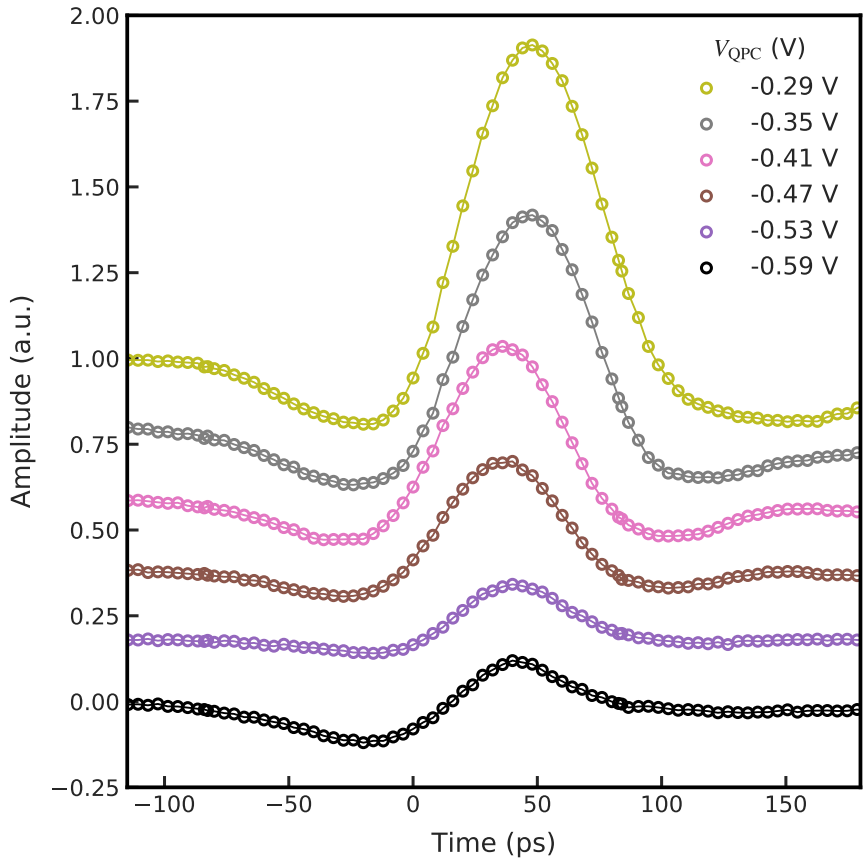

Figure 3.15: Creating excitations with the QPC. Voltage pulse generated by varying the DC voltage on the QPC and by keeping the voltage pulse the same. The curves have been offset vertically for clarity. For the measurement, QPC_1 is used to create the excitation and QPC_3 as a fast switch to resolve the pulse. The side gate voltages are kept with V_{SG} = -0.8 V.

trace resembles the AWG output, as shown in figure 3.8, which means that the RC time is similar to or higher than the pulse widths. Applying a more negative voltage to the QPC, the time-resolved trace resembles the derivative of a Gaussian pulse, as shown by the black trace (V_{QPC} = -0.59 V). In this situation, the RC time is much shorter than the pulse widths ($\tau = RC \ll 80$ ps), and our system behaves as an RC-differentiator.

In figure 3.16, we plot the variation of the output signal of a hypothetical RC differentiator. The curve in blue is the input signal. The orange curves are the output signal. The difference between the two orange curves is the time constant of the RC circuit ($\tau = RC$), where the upper one corresponds to an RC time equal to the voltage pulse period (T). The lower curve corresponds to an RC time of 0.1 T. Hence, as we decrease the RC time constant of the circuit, the output gets closer to the derivative of the input signal. In our case, we are keeping the pulse width constant and altering the RC constant *in-situ*. This is consistent with the observation seen in figure 3.15 .

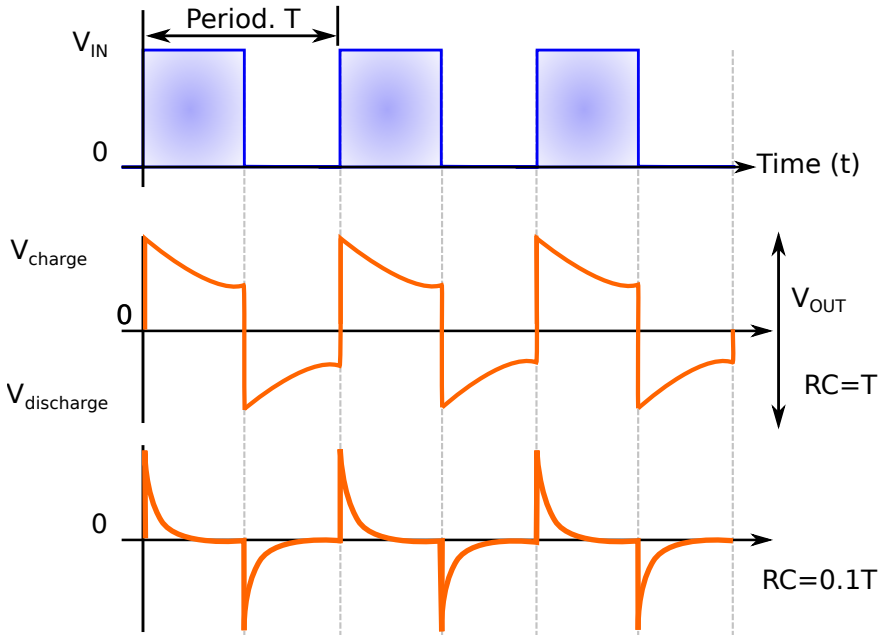

Figure 3.16: RC differentiator output. The blue curve is the applied pulse. The orange curves are the output signal, for different RC time constants, applying the same pulse. **Top,** RC = T. **Bottom,** RC = 0.1 T. The figure is adapted from ref. [132].

In figure 3.17, we show a comparison of the measured signal (black dots) when we apply a Gaussian pulse of a width of roughly 80 ps (top) or a square pulse with width of approximately 420 ps (bottom). We also plot the injected pulse (blue dotted curve) and its numerical derivative (green curve) of the injected pulse. These data confirm the validity of our RC-model interpretation. In figure 3.17**b**, indeed we observe that the measured signals are very close to the derivative of the input signal. In addition, we observe that the positive and negative pulses are more separated in the time domain for the square pulse as expected due to the longer period. The additional wiggles between the main two peaks appear because our square signal is not a perfect square. This is shown by the numerical derivative of the square pulse (green curve) in figure 3.17**b**.

Thus, by applying a voltage pulse to a QPC, it is possible to create excitations in the 2DEG. The shape of the induced excitation depends on the coupling between the QPC and the 2DEG, which can be regarded as a quantum capacitance [133]. Moreover, in this configuration, the system behaves as an RC circuit, in which the quantum capacitance can be controlled *in-situ*, by varying the DC voltage on the QPC.

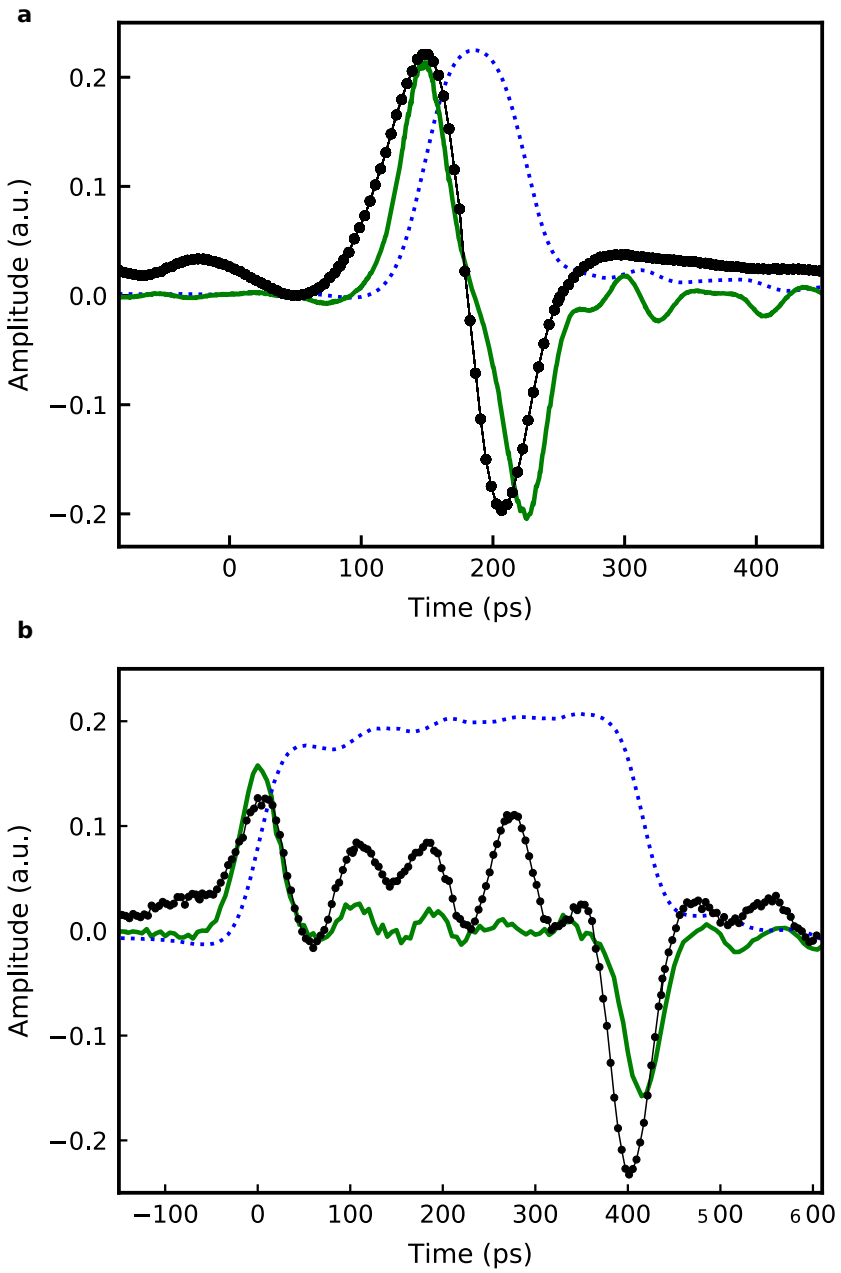

Figure 3.17: Effect of different pulse shapes applied at the QPC. a, Gaussian pulse of width $\approx 80\,\mathrm{ps}$ applied to QPC_1 (dashed blue line). The green curve corresponds to the numerical derivative of the applied voltage pulse. The black dots corresponds to the time-resolved trace measured at QPC_3. **b,** Same as **a** but the applied voltage pulse is a square pulse of widths of $\approx 420\,\mathrm{ps}$ (dashed blue line).

Homodyne detection

In the following section, we will concentrate on the detection of the generated electron wave packet. To determine the current going through the sample, we have a 10 kΩ SMD resistor soldered on the PCB which is connected to the ohmic contact used to collect the current. The resistor is connected from the ohmic contact to the ground in order to convert the current to voltage. This resistor is placed directly on the chip carrier, to give the minimum Johnson-Nyquist noise, since this is the coldest part of our experiment. To measure the voltage across the resistor, we use a home-made amplifier (EPC1b) at room temperature with a gain of 10^3 and a noise level of $0.4\,\mathrm{nV/Hz^{1/2}}$ [123]. After the voltage amplifier, the signal is fed into a lock-in amplifier to have an optimised signal to noise ratio (SNR). We use the lock-in Signal Recovery DSP 7265.

To perform DC measurements, we have used a low-frequency square signal, that can be created with the DAC. The amplitude of the signal needs to be small, such that the voltage bias does not overheat the sample. Therefore whenever we work at 20 mK the applied voltage is not larger than $V = \mathrm{k_B} \cdot \mathrm{T}/e \approx 2\,\mu\mathrm{V}$. To give a rough idea about the current expected, considering that we have perfect ohmic contacts (resistance equals zero) and that we set the sample at the first plateau of conductance ($\approx 13\,\mathrm{k\Omega}$) in series with the 10 kΩ would give a current of $\approx 100\,\mathrm{pA}$. Hence, the voltage expected on the lock-in amplifier for that situation is around 1 mV, which is measurable with our low noise set-up.

To apply such small voltage bias to the sample, whenever we used a DC bias, we have added a resistor divider between the DAC and the DC line. In this way, we are not limited by the resolution of the DAC, and we can create a signal as low as 2 µV.

To perform the time-resolved measurements, we have added a modulation on top of the RF pulses, to be able to do lock-in measurements, as described in figure 3.9. We present in figure 3.18 the complete electronic scheme of our set-up including the main electronic components and equipment. The low temperature part (20 mK) is represented by the red dashed line. For the injection of the voltage pulse to the ohmic contact as well as QPC_{1-3}, we have a large bandwidth bias tee connected [1], such that we can apply AC and DC voltages. There is a resistor R = 10 kΩ connected to the ohmic output contact used to collect the current as aforementioned.

1 bias-tee SHF BT45

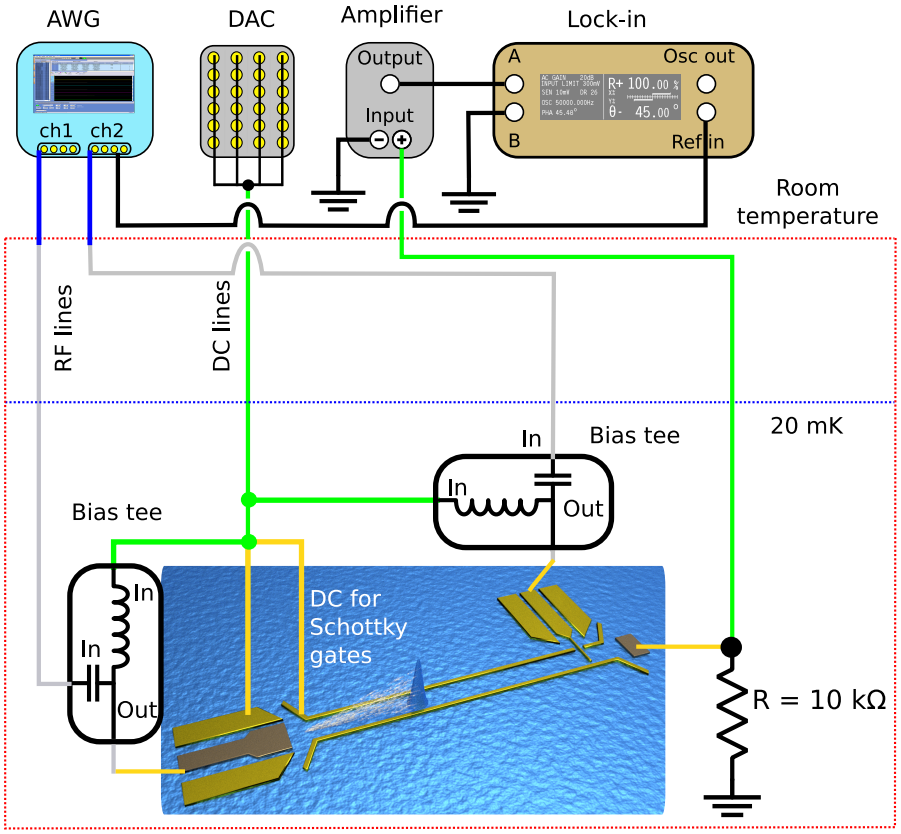

Figure 3.18: Schematic of the measurement set-up. The main electronic equipment is depicted in the top. The grey (green) lines represent the RF (DC) lines. The golden lines represent the bonding wires, used to connect the chip carrier to the sample. The bias tees are represented by the box with a capacitor and inductor and are connected to the injection ohmic and at the fast QPCs. The resistor R on the right is used to convert the current into voltage. The red dashed line represents the part which is at T= 20 mK — sample image; credit: Giorgos Georgiou.

3.5 Time-resolved measurements

We will now discuss the technical details of our measurements since we have already discussed our set-up. To resolve the excitation created at the 2DEG, we use the QPC as a barrier, and due to the non-linearity of the conductance trace, we can open this barrier for a minimal time. The use of the QPC as a fast switch was previously employed by [102], although the kind of excitation resolved was is very different, as described in section 1.9.2. In their case, they were working in the Quantum Hall effect, where the channels of conductance are spatially separated, and they probe edge magnetoplasmons. The physics of the excitations which we are creating will be discussed in the next chapter. In the following section we will outline how the time-resolved measurements are performed.

QPC as a fast switch

To measure the time-resolved trace of a few electron wave packet we will implement a pump and probe technique, well known in the field of optics. This is done by operating the QPC as a fast-switch with the following operation steps: First, we apply a negative DC voltage V_{DC} at the QPC, such that the conductance drops to zero and what is usually referred to the pinch-off regime. In figure 3.19, we show a conductance trace of a QPC versus the applied voltage, and we indicated with an arrow the V_{DC} needed to achieve the pinch-off. Then, we apply a very short voltage pulse on the QPC, such that the conductance is finite for a brief moment. The time that the QPC is open, i.e. conductance is higher than zero, is much shorter than the applied pulse width due to the non-linearity of the conductance trace of the QPC.

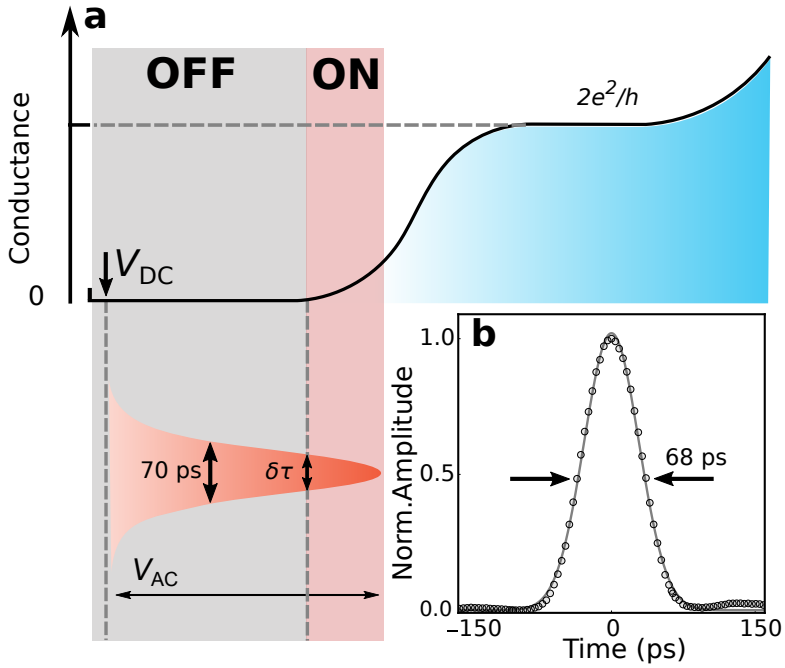

Figure 3.19: A QPC as a fast switch. a, Operation diagram of the QPC switch. Initially, a DC voltage (V_{DC}) is applied to the QPC to set it deeply in the pinch-off regime. Then, a voltage pulse is applied to the QPC (V_{AC}). By carefully choosing V_{DC}, the QPC opens for a very short time. The dark circles are the time-resolved trace, and the continuous grey line is a Gaussian fit. Figure reproduced from [120].

The complete procedure for the time-resolved measurements is the following. We start by applying an ultrashort voltage pulse to the Ohmic contact, and this pulse causes a local change in the density of electrons and which results in a collective excitation (see chapter 4). This excitation propagates towards the quasi-1D quantum conductor. At the same time, we apply a similar pulse to the QPC, and we measure the rectified current going through the 10 kΩ with a repetition frequency of ≈ 600 MHz. We then change the time delay between these two pulses. If there is no time-overlap between the opening and closing of the QPC

and the arrival of the electron excitation at the QPC position, the rectified current is zero. Only if there is a sizeable overlap, we will measure a finite current. By changing the time delay with picosecond resolution, we can then perform time-resolved measurements of the few-electron wave packet. Strictly speaking, we measure the convolution between the excitation and the conductance variation of the QPC (generated due to the voltage pulse). However, since the "opening" of the QPC happens on a time-scale much shorter than the temporal width of the excitation we are probing, we can consider the "opening" of the QPC as a delta function. Thus the time-resolved trace is basically reproducing the one of the electronic excitation.

To determine the best V_{DC} applied to the QPC for the time-resolved measurements, we first do a pinch-off measurement. We then start performing time-resolved measurements, by first setting the V_{DC} to the value where the current becomes zero. Next, we apply a more negative DC voltage on the QPC, and repeat the time-resolved measurements until we achieve a situation where the full width of half maximum (FWHM) reaches a minimum and eventually becomes roughly constant. From that point, the width stays almost constant even for more negative V_{DC}. However, the signal gets smaller and smaller. For the optimal QPC condition, we choose the DC value, where we obtain the minimum FWHM and the largest amplitude. Such a calibration procedure is displayed in figure 3.20. On the left side (figure **a**), we have the raw data, and on right side (figure **b**), we have the normalized data.

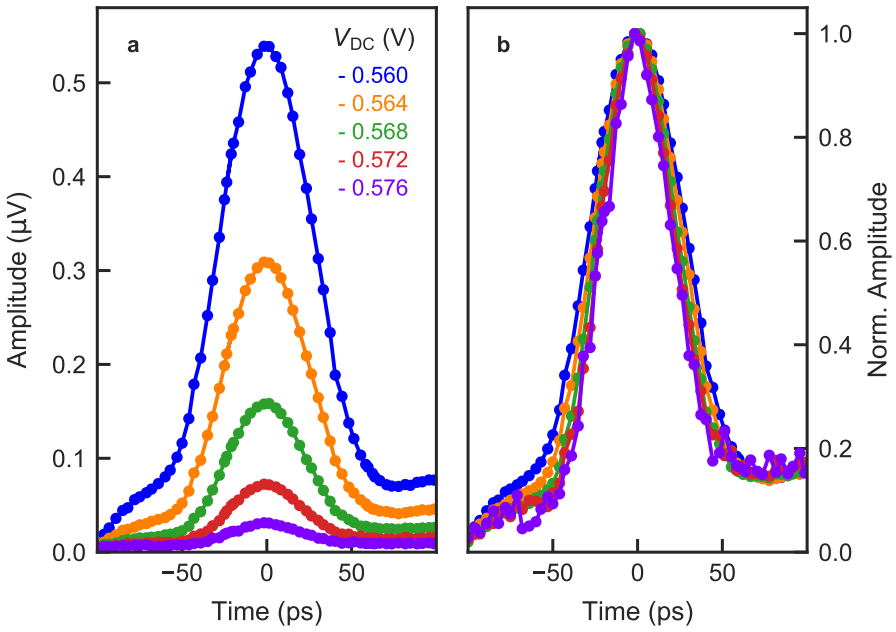

Figure 3.20: Tuning of the DC position at the QPC. a, The colourful lines are the time-resolved curves taken for different V_{DC} at the QPC_3. The more negative voltage we apply, the smaller is the pulse amplitude. **b,** We plot the normalized curves from **a**.

Simulating the measured signal

To have a more in-depth insight into our calibration method, we try to simulate our time-resolved measurement. To do so, we need to estimate the pulse shape at the sample level, considering the dispersion in our RF lines. We need also to take into account the effect of the bias tee on the pulse. Next, we need to estimate the attenuation considering that we have no 50 Ω matching. The ohmic contact of the injection has as an estimated resistance of 1 kΩ and let us consider that the impedance from the QPC to the 2DEG is infinite. Finally, we need to perform a convolution of the electronic excitation at the ohmic contact with the conductance pulse induced by the voltage pulse sent to the QPC, taking into account the DC and AC component.

To consider the effect of the bias tee, we can measure the pulse from the AWG, going directly to one bias tee and then to the sampling oscilloscope (WaveExpert 100H). We have considered one of the most common forms of an attenuator, the 'T-design', to estimate the total attenuation and by assuming a load that is not fifty ohms matched. This derivation can be found in appendix H.

To take into account the dispersion in the RF lines, we have measured the transmission S_{21} as a function of frequency. We have fitted the transmission versus the frequency to calculate the actual attenuation for each frequency component from which our signal is composed. We determine the amplitude of each frequency from which our signal is composed by applying an FFT on the signal measured at the sampling oscilloscope. We plot the fit of the transmission of the RF lines in appendix J.

To convolute the pulse at the ohmic contact with the conductance change on the QPC, we need to determine the conductance variation as a function of time. For this, we first determine the conductance trace of the QPC as a function of QPC-gate voltage by applying a DC voltage to the ohmic contact using the bias tee, as show in figure 3.21. Then, based on the calculated voltage pulse that must arrive at the QPC and the conductance trace as a function of the voltage at the QPC, we calculate the conductance variation as a function of time.

We plot the calculated time trace of the conductance in figure 3.21. We can see that the smaller (more positive) the DC voltage, the larger and broader is the conductance. This is expected since a smaller DC voltage implies that our fast switch would be open for a longer time. In figure 3.22, we plot the convoluted signal by taking the calculated voltage pulse arriving to the ohmic contact. The result shown in figure 3.22 is derived using a discrete convolution, which is defined by

$$(V * G)[t] = \sum_{\tau=0}^{T} V[t-\tau]G[\tau], \tag{3.4}$$

where V and G correspond to the voltage pulse applied at the ohmic contact and the conductance response of the sample. This convolution is proportional to the current traversing the sample. T is the total time of one waveform.

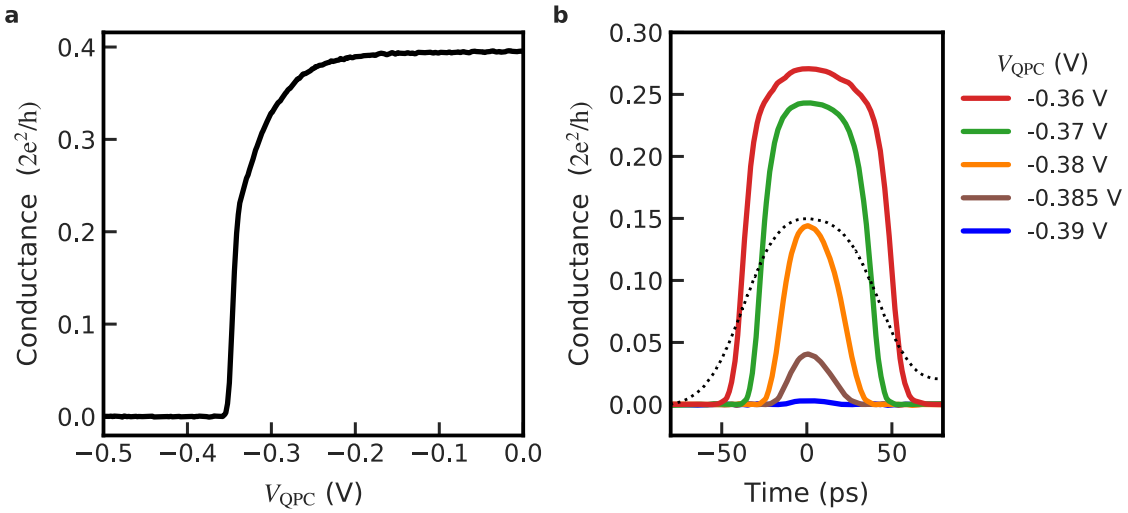

Figure 3.21: Conductance change due to the voltage pulse. **a,** Conductance of the entire system (ohmic contacts in series with the quasi-1D conductor) as a function of V_{QPC} **b,** Expected conductance in the time domain, considering the estimated voltage pulse arriving to the QPC_1. The different traces correspond to different DC voltage set at the QPC_1 (V_{QPC}). The dashed black line is the voltage pulse at the output of the AWG.

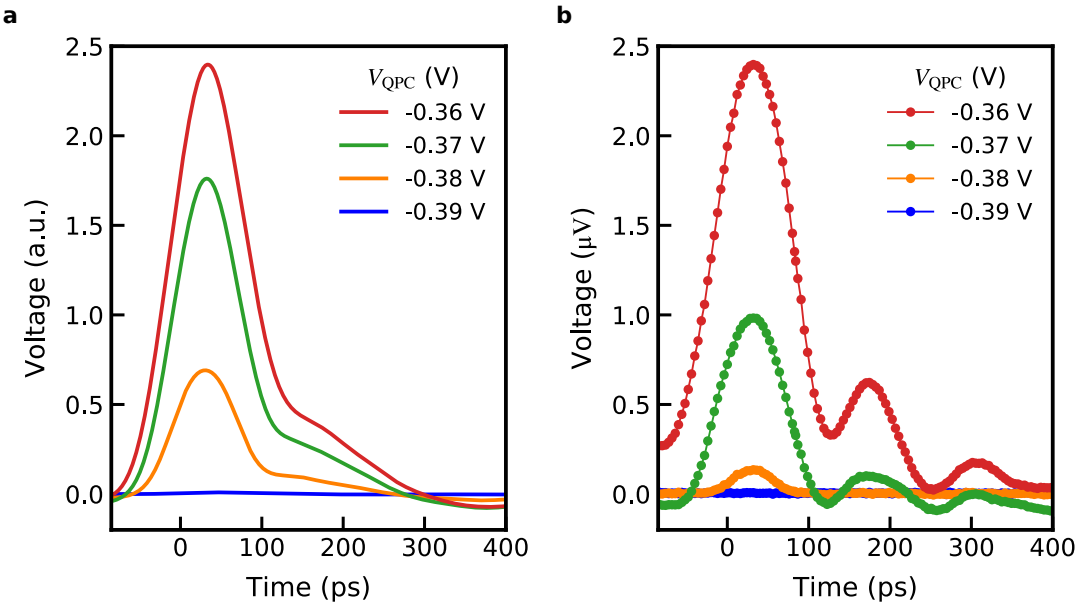

Figure 3.22: Simulating the time-resolved pulse considering the real parameters of our system. **a,** The time-resolved trace considering the convolution of the expected conductance and pulse arriving into the injection. **b,** Time-resolved measurements at QPC_1.

The convolved pulses are higher and broader for more positive V_{QPC}, which is reasonable since the conductance also gets bigger and broader. We have a good semi-quantitative agreement between the simulated and the experimentally time-resolved trace. By changing the DC voltage by a few tenth of mV, we can completely suppress the time resolved signal as seen in experiment and simulation. The change in amplitude and shape of the time-resolved trace are also well reproduced. We also observe a tail in the simulations as observed in the experiment, even though we observe more enhanced wiggles in the measurements. This may come from the fact that we are overestimating the attenuation at higher frequencies. As mentioned before, these wiggles are an artefact of the AWG. We can almost suppress them, by having a very small conductance on the QPC, such that these wiggles are reduced to the noise level of our time-resolved traces. The measurements and the simulated data were done for a $V_{\mathrm{SG}} = -\,1.6\,\mathrm{V}$

3.5.1 Time calibration - what do we need to know?

A crucial part of this experimental work is related to the time calibration of our system with picosecond accuracy. To calculate the velocity of the electron pulse in our system, we need to know with high precision the time-of-flight that the voltage pulse takes to propagate from the generator until the sample. Writing in a formal way we have: $T_{\mathrm{GOC}} + TOF = T_{\mathrm{GQPC}} + \Delta\tau$, where T_{GOC} is the time it takes the pulse to propagate from the generator until the ohmic contact, T_{GQPC} is the time that the pulse takes to go from the generator until the QPC, TOF is the time-of-flight on the sample and $\Delta\tau$ is the parameter that we control, allowing us to change the delay between the pulse sent to the ohmic contact and the QPC. In the end, to know the time-of-flight on the sample, what we need to know is:

$$TOF = (T_{\mathrm{GQPC}} - T_{\mathrm{GOC}}) + \Delta\tau. \tag{3.5}$$

The main result of equation 3.5 is that we do not necessarily need to know the time-of-flight of the pulse going from the generators to the sample. We only need to know the difference in the time it takes for the pulse to reach the ohmic contact compared to the time it takes to reach the QPC. To characterise the time-of-flight in the RF lines in the dilution refrigerator we used two different calibration methods: One using reflectometry, where we have characterised the time-of-flight in each component of our system and the second one is *in-situ* with the sample, using the fact that the velocity of the plasmon in a 2D system [134] is much faster than the velocity of the quantity that we are looking at. We will describe in details both types of calibrations in the next two subsections.

Time calibration: Reflectometry

To measure the time-of-flight in each component of our system we use a reflectometry set-up. We connect our generator to a resistive power divider[1]. One of the outputs we connect directly to the oscilloscope [2] and the other output we connect to the RF line that we want to characterise. On that line, the extremity needs to be open (disconnected). Like

1 http://www.clearmicrowave.com/spec/resistive/D226.pdf
2 http://cdn.teledynelecroy.com/files/pdf/lecroy_waveexpert_specs.pdf

this, the pulse applied will be reflected at the end of the line and will go back through the resistive divider to the oscilloscope. On the oscilloscope, we observe two different pulses, one with high amplitude (the one that goes directly to the oscilloscope) and a smaller one, the one which is reflected. The time separation between these two pulses allows to determine the time-of-flight across the corresponding component.

We show in figure 3.23 a schematic drawing of the measurements set-up. It is essential to characterise all the components of the RF lines from room temperature until the sample level. For this, we test each cable as well as each attenuator separately. This calibration approach offers at most a time accuracy of $\approx \pm 5\,\mathrm{ps}$, because the RF lines cannot be measured with the attenuators installed.

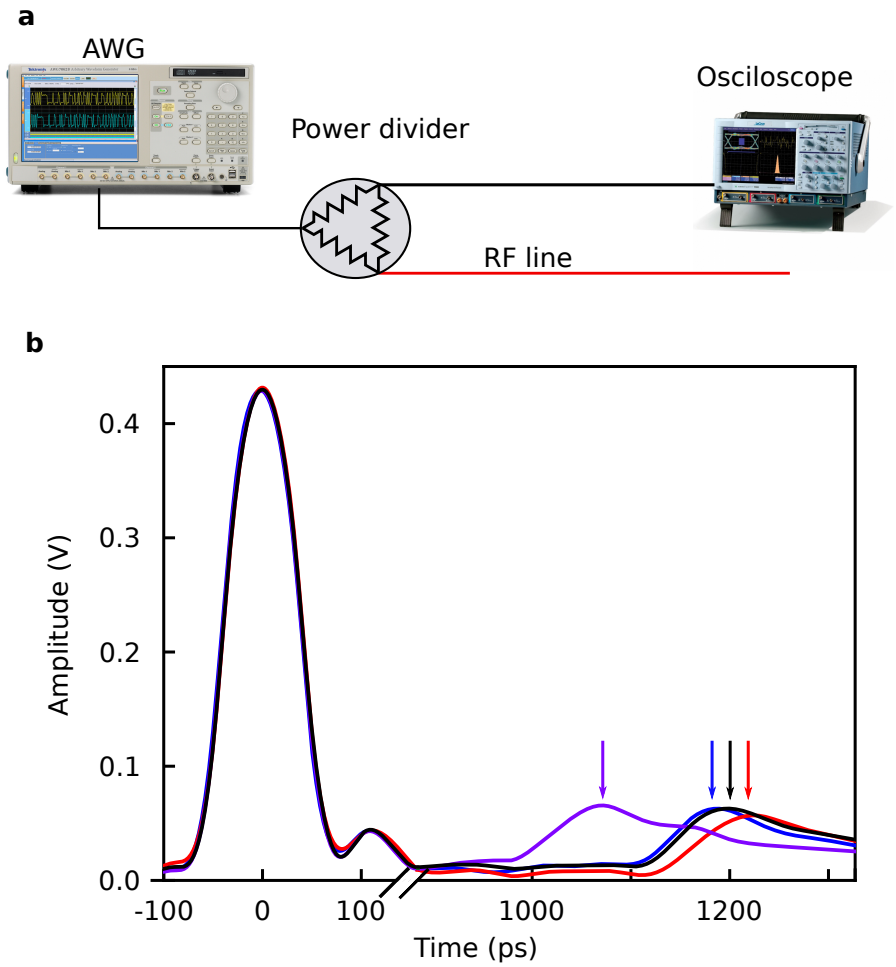

Figure 3.23: Reflectometry set-up. **a,** Schematic drawing of the reflectometry set-up **b,** The Gaussians at time equals 0 s are the pulses applied in the RF line, while the smaller amplitudes are the reflected pulses. The four arrows indicate the time position of the reflected pulses in the lines connected to the ohmic contact (blue curve), QPC_1 (red curve), QPC_2 (purple curve), QPC_3 (black curve).

Time calibration: in-situ

A more precise calibration can be done exploiting the fast propagation of the 2D plasmon. To create such an excitation, we set almost all the gates to zero, except the QPC_1 used as a fast switch (in this case) and the gate opposite of it, as highlighted in figure 3.24.

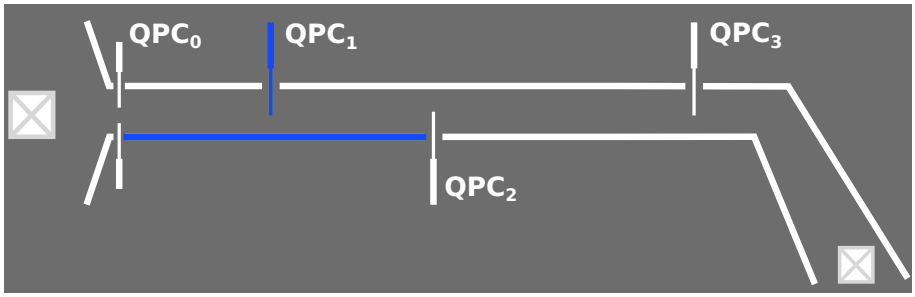

Figure 3.24: In-situ calibration. Scheme of the configuration used to measure the arrival time of the 2D plasmon. The gates highlighted in blue are polarised, all the other gates are set to zero.

We apply a voltage pulse to the ohmic contact, which will give rise to a collective excitation in a 2D system. The propagation velocity of a 2D plasmon is known to be $v_{\mathrm{P}}^{\mathrm{2D}} \sim 1 \times 10^7\,\mathrm{m/s}$ [134, 135]. Thus, the injected pulse will arrive at the sampling QPC almost immediately. By measuring the time-resolved trace of the 2D plasmon, we can estimate the difference in propagation time between the RF line used to create the excitation and the one connected to the QPC detector.

For all the following results on this manuscript, we adopted the *in-situ* calibration to do the conversion from time-resolved measurements to time-of-flight of the electronic excitations.

Time-resolved measurements varying the excitation number

To estimate the number of excited electrons contained in one voltage pulse, we measure the rectified current across the $10\,\mathrm{k\Omega}$ resistor, which is placed on the chip carrier, at 20 mK. Then the signal is amplified at room temperature and measured with a lock-in amplifier. The signal is proportional to the number of generated electrons $\tilde{n}_e$ and also to the repetition rate of our RF signal, as described below,

$$I = \tilde{n}_e\, e\, f = \frac{V_{\mathrm{rms}}}{A}\,\frac{1}{10\,\mathrm{k\Omega}}\,\frac{\pi}{2\sqrt{2}} \tag{3.6}$$

where V_{rms} is the voltage measured with the lock-in amplifier, $A = 1000$ is the gain of the room temperature amplifier, and the factor $\frac{\pi}{2\sqrt{2}}$ appears because our modulation signal is a square signal and not a sinus (see Appendix A).

3.6 Conclusion

In this chapter, we have presented the experimental set-up. We started by discussing the sample fabrication and the sample designs to study the dynamics of a quantum conductor as well as coherent tunnelling oscillations in order to determine the coherence length in our system. We then introduced our experimental set-up, the changes that have been added compared to the set-up when I arrived at the Néel Institute. In particular, we detail the new RF set-up and the new cold finger that has been realised during my PhD. This is followed by a detailed description of the time-of-flight measurements that we have performed. Special emphasis has been put on the calibration of the RF lines in order to be able to measure precisely the time-of-flight of an electronic excitation in our waveguide.

In the next chapter, we will apply these technical developments, to characterise the dynamics of a voltage pulse propagating at the surface of the Fermi sea.

CHAPTER 4

Experimental results

In this chapter, I will present the main experimental results of this PhD work, namely the time-resolved measurements of a single-electron wave packet as well as its propagation velocity. We will show how such measurements will give deep insight into the propagation of an electron wave packet in 2D electron systems. In particular, we will investigate the effect on the confinement potential or in other words, the number of available single-particle states in the quasi-1D quantum conductor. Combined with numerical simulations, we are able to demonstrate the importance of electron-electron interactions in such 2D electron systems.

In order to avoid confusion, let us define the terminology that we use in this chapter. Whenever we mention the word **channel**, we refer to the single-particle states. The coupling between the single-particle states give rise to a different eigenmode in the system, and we use the word **mode** to refer to these collective excitations.

4.1 Time-of-flight measurements

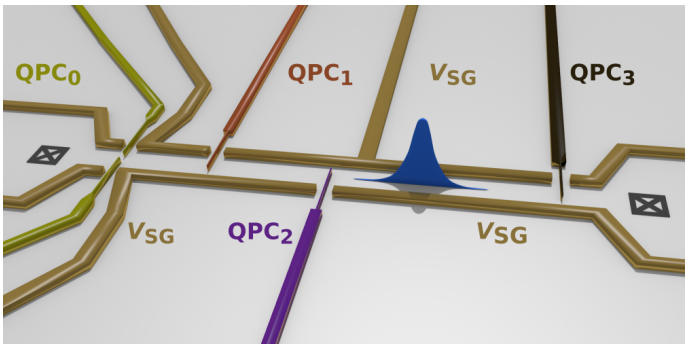

Figure 4.1: Sample design. The golden gates are the electrostatic gates. The gates in yellow, orange, purple and black represent the QPC_0, QPC_1, QPC_2 and QPC_3 respectively. The two squares with cross represent the ohmic contact. The wave packet is represented in blue, going from the left ohmic contact to the one on the right. The distance between the ohmic contact in the left and the QPCs are 10.9, 20, 35 and 75 µm.

In figure 4.1, we show a schematic of the sample designed to study the propagation of electronic excitations. To create an electron excitation in the 2DEG, we apply a voltage pulse on the ohmic contact (the square with the cross on the left side). We guide this excitation into our quasi-one-dimensional conductor, formed by the Schottky gates (gates in gold color), polarised with the side-gate voltage V_{SG}. We have described in detail the sample in chapter 3. The idea of the measurement is to determine the arrival time of

the electron wave packet at different distances using the different quantum point contacts (QPC1, QPC2, QPC3). To measure the arrival time, we use a time-resolved measurement technique presented in section 3.5 of chapter 3. Where we repeatedly inject the electron excitation in the quasi-one-dimensional wire. We are applying a voltage pulse on one of the QPCs, to make it work as a fast-switch. Moreover, this fast-switch allows the transmission of a tiny part of the electron excitation. We measure the DC current generated on that process. Changing the delay between the generation of the electron excitation and the voltage pulse in the QPC, we can measure in a time-resolved manner the electron wave packet. We have discussed this technique in further details in the preceding chapter in section 3.5.

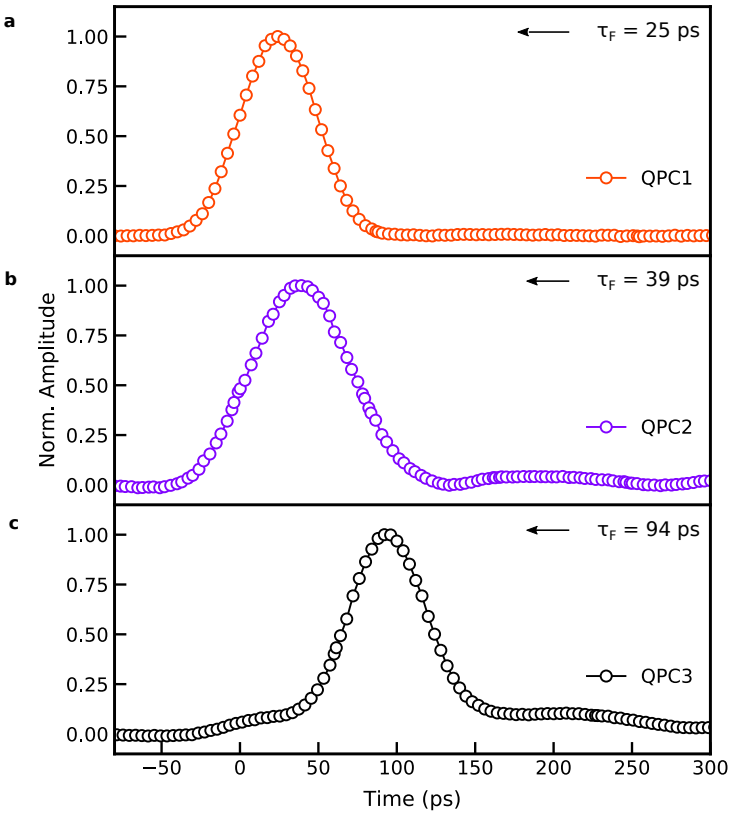

Figure 4.2: Time-resolved measurements at different distances. The plots **a,b,c** were taken at different QPCs, placed at distance d = 20, 35 and 75 µm from the ohmic contact.

In figure 4.2, we show the time-resolved measurements of the electron wave packet at the three different QPCs. One observes that the maximum of the wave packet moves to longer arrival times. This clearly indicates that the wave packet propagates through the quasi one-dimensional waveguide. We also observe a change in the widths of the electron wave packet for different propagation length. This could be associated with the dispersion in our waveguide. Indeed, comparing the figures 4.2**a** and **b**, we see an increase of the width when the pulse has propagated over longer length. This hypothesis is, however, ruled out

looking at the pulse that has propagated over the longest distance in our system (75 µm), shown in 4.2**c**. This width is similar to the one of the electron wave packet measured for the shortest distance as seen in figure 4.2**a**. The explanation comes from the fact that the measured current ΔI is proportional to the voltage applied in the ohmic contact $\Delta V_{\mathrm{SD}(t)}$ times the conductance change in the QPC ($\Delta G(t-\tau)$). However, each QPC has a different response function when a time dependent voltage is applied.

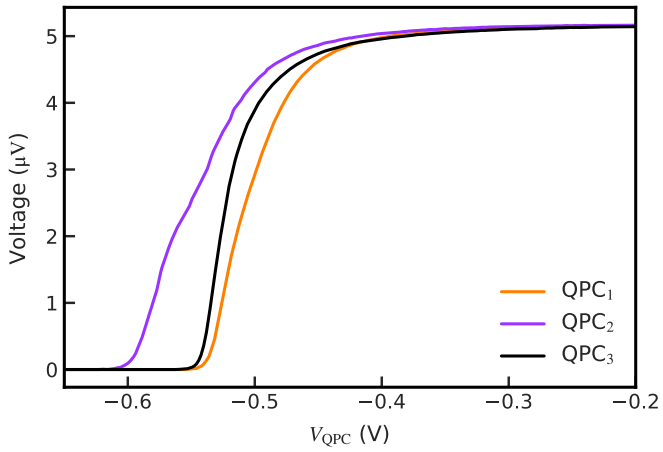

Figure 4.3: Pinch-off curve of the different QPCs. Voltage on the 10 kΩ resistor versus the voltage applied to the QPCs. The side gates were set to $\mathrm{V_{SG}} = -0.8\,\mathrm{V}$.

To highlight this effect, we show the pinch-off curves for the QPCs in figure 4.3. To measure the pinch-off, we apply a low-frequency voltage in the injection ohmic, which induces a current going through the sample. We convert this current into a voltage on chip by adding a 10 kΩ resistor connected in series with the sample. The voltage measured across the 10 kΩ resistor is plotted on the y-axis of figure 4.3. Thus this value is proportional to the conductance due to the voltage applied to the QPC. There is a significant difference in the pinch-off trace of $\mathrm{QPC_2}$ that we do not fully understand. This difference could be related to fabrication issues, such as imperfect sticking of the gates. The difference of the pinch-off of $\mathrm{QPC_2}$ results in a wider time-resolved trace, as observed in figure 4.2**b**. For the QPCs with similar pinch-offs, we get similar time-resolved traces, as shown in 4.2**a** and **c**. The pulse with minimum widths is measured at $\mathrm{QPC_3}$. The explanation comes from the fact that this is the QPC with the most abrupt conductance trace close to pinch-off, as we can see in the black curve of figure 4.3.

The time-resolved electron wave packet corresponds to the convolution between the electron wave packet going through the quasi one-dimensional conductor and the response function of the conductance due to the voltage pulse applied to the QPC. Therefore, the steeper is the pinch-off trace, the sharper it will be the response function of the conductance, which results in a smaller widths in the resolved wave packet.

In order to extract the propagation velocity, we plot the distance covered by the pulse versus the TOF and we also show a schematic drawing of the sample in figure 4.4. The

electron wave packet is generated at the ohmic contact in the left. Then, it propagates the length x_0 with a certain speed v_0 (which is unknown), thus spending a time $t_0 = x_0/v_0$ before entering in the quasi-1D system. From that moment on, it propagates with velocity v_e, which we would like to determine. For this reason we measure the time of flight from the electron propagation until the QPCs, placed at the position x. We plot these data in figure 4.4 for a given confinement $V_{SG} = -1.2\,V$. One can see a linear dependence between the distance and the time, which shows that the velocity is constant inside the quasi 1D-conductor. For the determination of the arrival time, we have fitted the top part of the pulse with a Gaussian fit and used the time corresponding to the centre of the peak. We can describe the propagation of the electron wave packet considering only the position x of the centre of the peak as:

$$x = v_0.t_0 + v_e.(t - t_0) \tag{4.1}$$
$$x = v_0.t_0 - v_e.t_0 + v_e.t \tag{4.2}$$

where t is the arrival time that we measure at three different distances x. We have used the time corresponding to the centre of the peak. The equation 4.2 shows a linear dependence of the position x as a function of t. Applying a linear fit $x = a + b.t$ to the data, we can determine the slope b. Comparing with equation 4.2 **b**, we can determine the velocity v_e of the electron wave packet inside the quasi 1D-conductor through the slope b. For the plot in figure 4.4, the velocity found is approximately $7 \times 10^5\,m\,s^{-1}$.

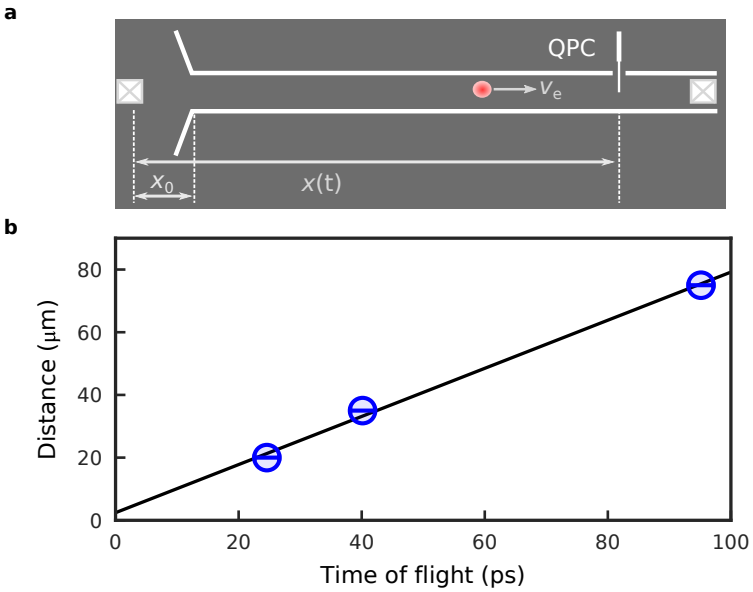

Figure 4.4: Propagation velocity. **a,** Schematic of the sample. **b,** The blue circles correspond to the arrival time of the electron wave packet at the different QPCs. The solid line is the linear fit.The confinement applied at the side gates is equal to $V_{SG} = -1.2\,V$ for the plotted data. Figure adapted from [120].

One could imagine that the Landau quasiparticles of the system carries the electronic excitation. The Landau quasiparticles are like free electrons with renormalised mass [117]. The effect of the Coulomb interactions is taken into account in the renormalisation and the velocity of the Landau quasiparticles is equal to the Fermi velocity. For our system, the Fermi velocity is $2 \times 10^5\,\mathrm{m\,s^{-1}}$ [18]. Thus the velocity of the electron wave packet is much faster than the Fermi velocity. To shed some light on this problem, we will investigate the amplitude dependence of the time-of-flight, as well the confinement dependence.

4.2 Measurements of the Plasmon velocity

4.2.1 Amplitude dependence

It is interesting to explore the amplitude dependence for two reasons: first, to show that the physics we are looking at is not dependent on the number of electrons and second, to show that with such a technique we are able to measure in a time-resolved manner electron wave packets which contain sub-electron number.

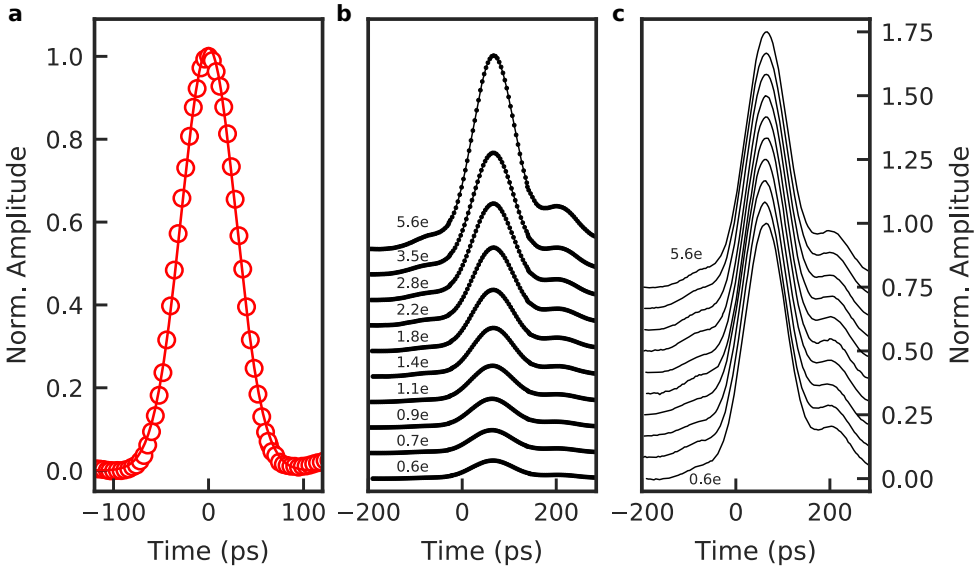

Figure 4.5: Time-of-flight measurements. a, Time-resolved measurement of an electron wave packet of Gaussian shape containing approximately 28 electrons. The red line corresponds to a Gaussian fit. **b,** The time-of-flight measured for different amplitudes. An offset is added for better clarity of the data. **c,** Normalised data of **b**. An offset is added for better clarity of the data.

We show in figure 4.5 **b** the time-resolved measurements for different injection amplitudes. We normalise the time-resolved measurement for different amplitudes and we plot them in 4.5 **b**. The time-of-flight curves are the very similar, showing no dependence of the velocity with the electron injected number. We also show in the plot the net number of electrons created by each voltage pulse, and demonstrate that we can measure electrons wave packets that contain less than a single-electron charge. These numbers are determined from the average current generated taking into account the repetition frequency of the pulses that

we apply. This determination of the electron number per pulse has been described in detail in section 3.5.1.

4.2.2 Confinement dependence

The next study concerns the change in propagation velocity due to the electrostatic confinement potential. We can modify the confinement potential with the gates used to define our waveguide (V_{SG}). In figure 4.6, we show the time-of-flight measured at a fixed length $L_3 = 75\,\mu\mathrm{m}$ (QPC_3), but for different confinements.

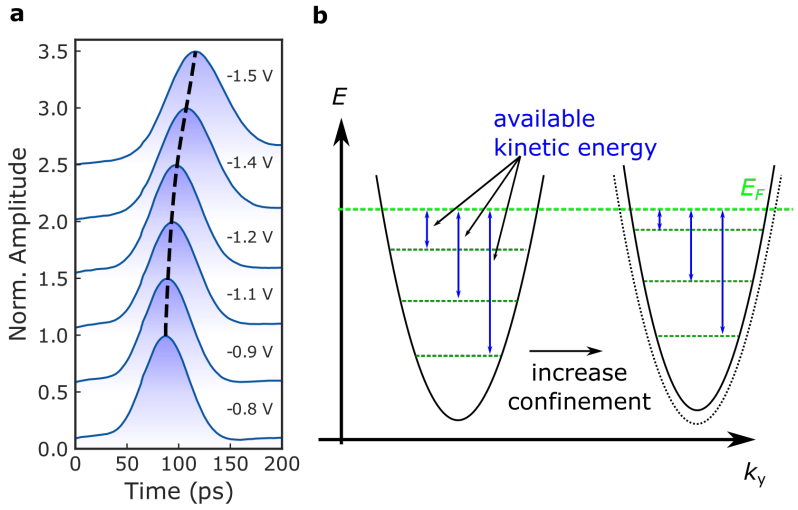

Figure 4.6: Effect of the confinement. a, Time-resolved measurements of a few electron wave packet as a function of the confinement of the side gates (V_{SG}). **b,** Change in the potential energy of the quasi-1D conductor when applying more negative voltage to the side gates.

One can see that for more negative gate voltages applied to the side gates used to define the waveguide, the pulse takes a longer time to arrive at the QPC detector. This behaviour indicates a reduction of the velocity when we make the confinement stronger. We can easily explain this phenomenon considering the electrostatic potential E_P created with the side gates. This potential is transverse to the propagation direction of the wave packet. For a given configuration, we have a fixed number of conductance channels available in our quantum conductor that contribute to the transport. Let us consider the kinetic energy the of these channels due to the transverse potential defined as $E_{\mathrm{kinetic}} = E_F - E_P = \frac{\hbar^2 {k_F}^2}{2m^*} - E_P$. Whenever we apply a more negative voltage to the gates, we are increasing the electrostatic potential. Therefore, we are shifting the channels towards the Fermi energy which results in a smaller value for the kinetic energy, as represented in figure 4.6**b**. This is in qualitative agreement with our observations.

To summarise our findings, we plot the velocity as a function of the confinement of the side gates (V_{SG}) in figure 4.7. We observe that the velocity shows a monotonic behaviour with the confinement V_{SG}, in quantitative agreement with what we observed in figure 4.6. The weaker the confinement, the higher is the propagation velocity. We also plot in figure 4.7 the Fermi velocity of our system, derived from a parameter-free simulation that we discuss. Remarkably, the velocity of the electron is much higher than the Fermi velocity,

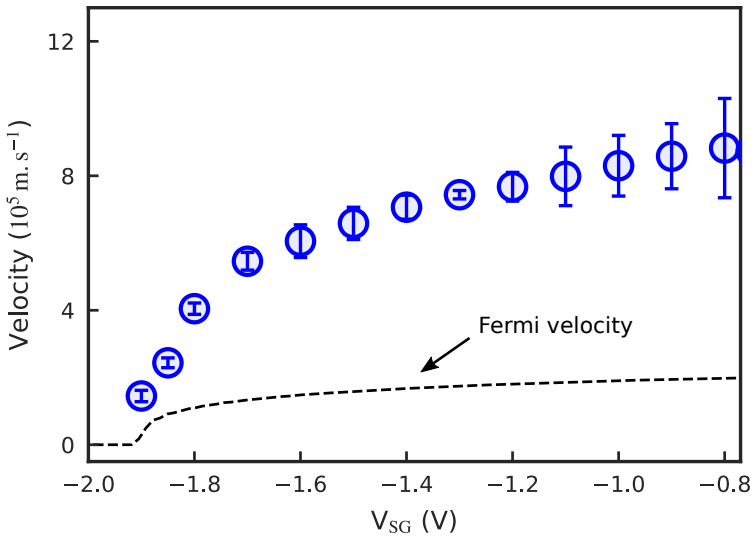

Figure 4.7: Velocity of Gaussian pulses. The velocity of the gaussian pulses for different confinements induced by the side gate voltage V_{SG}. The blue circles correspond to the velocity calculated from the experimental data, and the dashed line corresponds to the Fermi velocity in our system.

which shows that a non-interaction picture is not enough to explain the propagation velocity of an electron wave packet in our system.

Let us compare our results, with measurements taken at different regimes or different systems. For example, we can compare our findings with what has been measured in the DC regime, using transverse electron focussing by magnetic field [136]. The velocity of the electrons observed in this case is in agreement with the Fermi velocity, which indicates a vigorous screening of the Coulomb interactions. Another system with which we can compare is the single-electron tunnelling experiments [93, 97] that we discussed in section 1.9.1 of the first chapter. The central idea of the experiment is to measure the current generated by the electron tunnelling between two quantum wires. By varying the applied bias and the magnetic field to a quantum wire, one can control the Fermi energy and the momentum of the electrons. Thus, it is possible to map the dispersion relation experimentally, which gives access to the velocity of the collective excitation generated by the tunnelling of an electron to a quantum wire. It was observed a 30% increase in the excitation velocity relative to a non-interaction system [93]. However, the reference [97] predict the existence of a collective mode that propagates much faster than the Fermi velocity, which was not observed experimentally.

Our findings give a very different result. We observe a much faster velocity compared to the Fermi velocity. The difference has to come from the fact that here we deal with electron wave packets generated using voltage pulses instead of a DC bias. When we apply a voltage pulse, we are locally modifying the electron density with an excess of charge. This excess will acts on the surrounding electrons, due to the locally generated electric field, which

gives rise to a collective effect, known as a plasmon. In principle, an excitation created into a 1D system, generate collective effects. The 1D system, in our case, is a channel of conductance (single-particle states). Coupling 1D-systems, for instance, via Coulomb interactions, give rise to new collective modes of propagation. These new collective modes have renormalised velocities. One of the modes propagates with velocity much faster than the Fermi velocity. This mode is known as the charge mode. This name is related to the fact that the summing the charge distributed over the channels there is an effective charge being carried. The other modes are known as the neutral modes. The neutral modes propagate roughly with the Fermi velocity. The charge distribution over the channels is such that there is basically no net charge being carried. We described in chapter 2 the theoretical derivation for the velocity of the plasmons.

Plasmons have been observed in the past in quantum Hall systems. The first observations of plasmons propagating around the edge of a 2D electron system were in the '80s by two different research group at the same time [137, 138]. This plasmon is regarded as a particular kind, and it is called edge magnetoplasmon. The first measurements of this effect were realised inducing standing waves in a 2D electron system and recording the power absorbed. The existence of modes whose frequencies decrease with the field was observed, in contradiction with what is expected from the cyclotron frequency $w_C = eH/mc$. The solution of this problem corresponds to the existence of edge magnetoplasmons [137, 138].

A pioneering investigation of edge magnetoplasmons in the time domain was performed by Ashoori *et al.* [139]. By applying voltage pulses of $\propto 100\,\mathrm{ps}$ widths to an ohmic contact placed on the edge of a circular high-mobility 2DEG and then by doing time-resolved measurements of the generated wave packet with a sampling oscilloscope, it has been shown that the magnetoplasmon propagates along the edge, only in the direction expected for negatively charged electrons.

Furthermore, the edge magnetoplasmons were used as electron waveguide to study fundamental quantum phenomena such as the coherence length. As we have mentioned in section 1.5.1, one of these experiments was the Mach-Zehnder interferometer. An unexpected behaviour has been found in the amplitude of the oscillations of the Mach-Zehnder interferometer, of which the visibility varied in a lobe fashion way with the injecting bias [140, 141]. This lobe structure in the visibility is explained by the presence of the (slow) neutral modes [110], created by the long-range Coulomb between the edge channels.

A theoretical proposal [142] described a way of measuring the charge fractionalization, that is, the separation of charge and neutral mode by time-resolved measurements or shot noise measurements. Let us focus on the velocity of the charge mode measured in edge magnetoplasmons. The physics we are looking at is hence similar to what has been observed in quantum Hall effect.

The main difference between our system and the quantum Hall system, however, is that the conductance channels are separated in space for the latter case, while in our case, the channels of conductance are separated in energy.

The velocity found for the charge modes propagating over two edge channels is plotted in figure 1.16 of the first chapter. It has been shown a change in the velocity as a function of the voltage applied to a gate used to define the region of propagation of the edge channels. The values of the velocity vary from approximately $4.5 \times 10^5\,\mathrm{m\,s^{-1}}$ to $3 \times 10^5\,\mathrm{m\,s^{-1}}$, which

is the same order of magnitude of the velocity that we have found. However, in this case, the velocities increase when applying more negative gate voltages. The edge channels will travel further away from the gate when the voltage is more negative, which means less screening of the Coulomb interactions [102, 143, 144], leading to a higher velocity. On the other hand, in our system, we observe exactly the opposite effect, the velocity of the wave packet decreases when applying a more negative gate voltage. This effect happens because the velocity is proportional to the root square of the number of channels, as we have seen in chapter 2. The voltage applied to the metallic gates in the case of the Quantum Hall effect do not affect the number of edge channels, as in our case where the gate voltage defines the number of conductance channels.

4.2.3 Generation and TOF measurements of a Lorentzian pulse

As discussed in section 1.7.4, to go towards the control of a single-electron during the flight, we need to be able to inject a single-electron at the surface of the Fermi sea. The only way to do this, without adding unnecessary quasi-particles is sending Lorentzian pulses with the characteristic of $\int eV(t)\,dt = nh$, as discussed in [61–63, 66]. To reach this situation, we use a home-made system, inspired by the source developed in C. Glattli's group. We have described this source and the procedure used to create the Lorentzian pulse in section 3.4.3. One example of a time-resolved measurement of a Lorentzian electron wave packet is shown in figure 4.8. We can see the spacing between the pulses is proportional to the base harmonic used, in this case, 6 GHz. When we have used Gaussian pulses, one can observe some small wobbles on the right side of the tail of the Gaussian pulse, as shown in figure 4.5. With the Lorentzian pulse, we do not observe these extra features. The wobbles are an artefact and are created due to the generation of the pulse by the AWG, as the time resolution is too limited. We have no control over these additional features in the tail of the Gaussian pulse. These wobbles are also present in the pulse measured directly with the oscilloscope, as we have shown in figure 3.8 of chapter 3.

We can reproduce our measurements computationally by combining higher harmonics of the fundamental one with $f_0 = 6\,\text{GHz}$. The normalised amplitude (zero-to-peak) relative to that for the fundamental 6 GHz signal were derived from the fit as 2.4×10^{-1}, 4.4×10^{-2} and 1.2×10^{-2}, corresponding to the harmonics of 12 GHz, 18 GHz, 24 GHz, respectively. The numerical fit works very well, however, we find that the contribution of the fourth harmonic is very small. The reason is probably due to the strong attenuation of the signals above 18 GHz. We addressed this issue in section 3.4.3 when we discuss the new experimental set-up of the RF lines using K-connectors.

We have also measured the time-of-flight using a Lorentzian pulse, and we calculated the velocity for different V_{SG}, repeating the procedure described in the last section. We present the results in figure 4.7. The uncertainty in our findings using the Lorentz pulse is more significant than for the Gaussian pulses because we calculate the velocity with the time-of-flight for just two different distances (the shortest $L_1 = 20\,\mu\text{m}$ and the longest $L_3 = 75\,\mu\text{m}$). The reason is that for the second QPC we encountered a noisy signal. Long averages were, however, not possible due to the fact that the "pulse box" systems is not very stable in terms of phase drifts between the two signal generators which provide the 6 and 18 GHz harmonics.

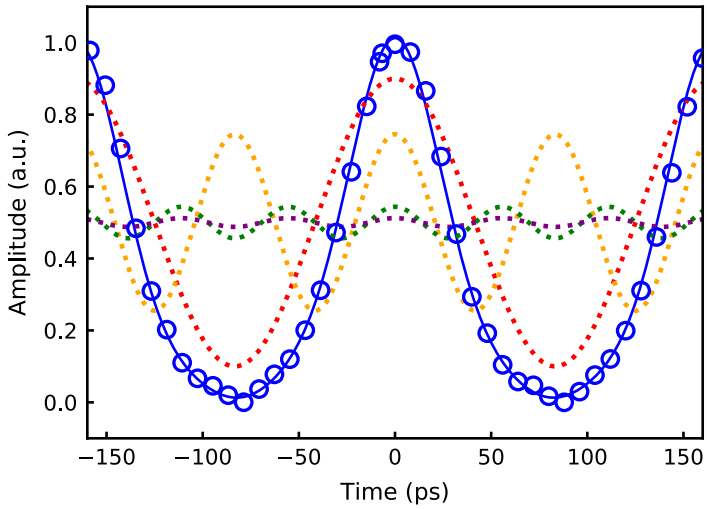

Figure 4.8: Time-resolved measurement of a Lorentzian pulse. The blue circles correspond to the pulse resolved at the sample level. The dashed lines correspond to the plot of the harmonics 6 GHz, 12 GHz, 18 GHz, 24 GHz in red, orange, green and purple, respectively. The blue line is the sum of the data of all the harmonics (dashed lines).

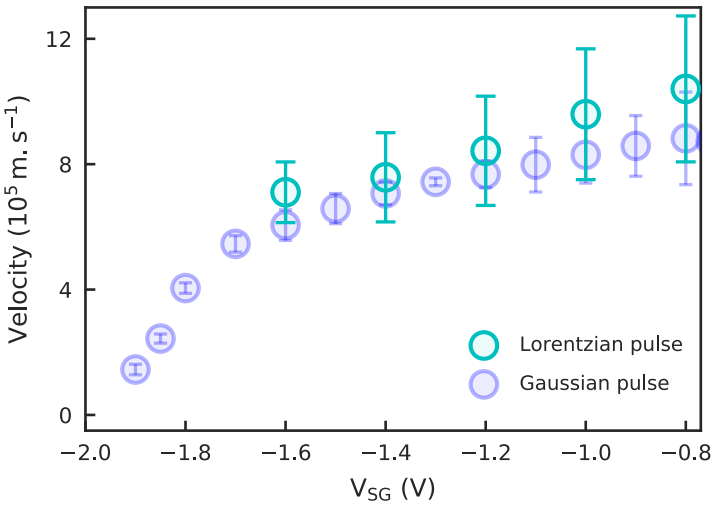

Figure 4.9: Velocity of Lorentzian pulses. Velocity of few-electron wave packets as a function of the side gates voltage V_{SG} for Gaussian and Lorentzian pulse shape.

Despite the larger uncertainty in comparison with the Gaussian pulses, the measured velocities are very similar. Therefore, we can conclude that our findings about the propagation of Gaussian pulses are also valid for Levitons.

4.3 Simulating the plasmon velocity

We will now compare the experimentally determined velocity with the Plasmon velocity in our system, to demonstrate that what we are probing is a collective effect of the Fermi sea, generated by the voltage pulse. We have seen in chapter 2 that to find the renormalised plasmon velocity, we need to know the Coulomb interactions. This task is not trivial considering that we are talking about a 3D system, where it is necessary to take into account the interactions between the channels and also the screening created due to the presence of the metallic gates needed to create the electron waveguide. We must also know the number of channels available when we tune the electron waveguide with the voltage applied to the side gates. These questions have been addressed through a collaboration with the group of Xavier Waintal. They have built a parameter-free model which allowed to calculate the plasmon velocity depending on the electrostatic confinement potential.

The main steps of the simulation are: First, determine the electrostatic potential landscape using a Poisson solver. This solver needs to take into account the presence of metallic gates with voltage V_{SG} and the dopant layer. Second, considering that the quasi-1D waveguide is infinitely long in the x-direction, they used Kwant [145] to solve the Schrödinger equation in the y-direction. With the wave function derived from the solution of the Schrödinger equation, it is possible to calculate a new density. Third, applying this new density to the Poison equation again, and repeating the same process until the solution converges, they perform what is called a self-consistent calculation. At the end of the process, it is possible to calculate the wave functions with energy lower than the Fermi energy.

It is also possible to calculate the interaction between the channels, calculating the Green's function numerically, as discussed in detail in reference [36]. Last, to determine the renormalised velocities, due to the interactions, one needs to solve the equation of motion 2.22. This equation corresponds to a problem of eigenvectors and eigenvalues. The eigenvectors appeared due to the coupling of single-particle states (channels of conductance) via the Coulomb interactions. We will call modes the eigenvectors of the system, taking into account the Coulomb interactions. The eigenvalues of this equation are velocities of each mode.

As we have discussed before, when we have two coupled 1D systems (Luttinger-Liquid like) the eigenvectors of this system are the charge and the neutral mode. The charge mode has equivalent charges distribution over the two channels, propagating together. The velocity of the charge mode is increased (reduced) for repulsive (attractive) interactions in comparison to the Fermi velocity. The neutral mode has opposite charges distribution, such that it carries zero net charge, and it propagates with a velocity close to the Fermi velocity. A similar effect happens for N-coupled 1D systems. Let us consider that the coupling is made by Coulomb interactions. Thus, there will be one charge mode, that propagates with increased velocity, which we will refer to as the plasmon velocity. There will be N-1 quasi-neutral modes as well, propagating roughly with the Fermi velocity. We plot the only the velocities of the fast mode found from this self-consistent electrostatic-quantum mechanics problem in figure 4.10.

The agreement between the experimental data and the simulation is remarkable, consider-

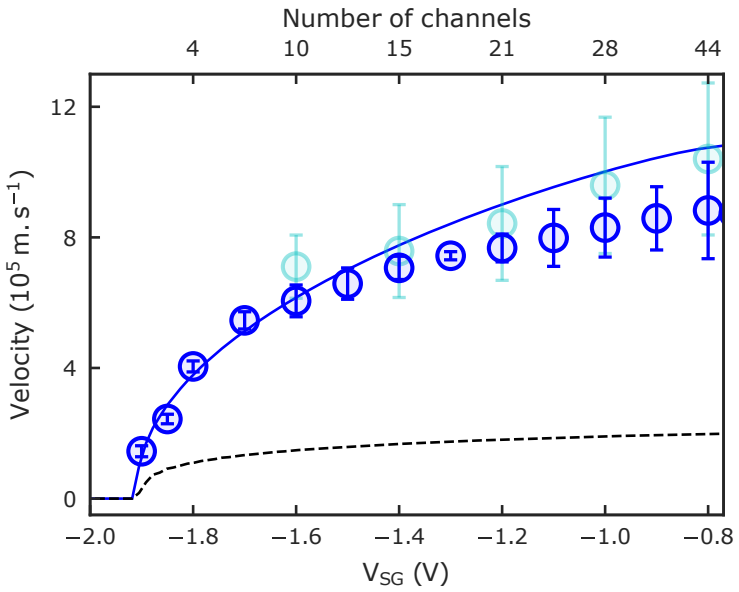

Figure 4.10: Parameter-free simulation of the plasmon velocity. The blue line corresponds to the velocity calculated by self-consistent calculations and taking into account the renormalisation due to Coulomb interactions. The dashed black line is the Fermi-velocity derived from the self-consistent calculations without interactions. The upper axis correspond to the number of channels of conductance available for each confinement. The blue and light blue circles are the experimental data previously plotted in 4.7 and 4.9.

ing the fact that there are no adjustable parameters. The differences between the velocities for low confinement (more positive V_{SG}) can be explained due to forward scattering. The simulation was done by only considering the electrostatics of the problem, without taking into account any scattering effects. The dashed line corresponds to the Fermi velocity derived from the density calculated from the self-consistent problem.

The number of channels plotted in figure 4.10 was obtained from the simulations, considering the number of eigenfunctions available with energy lower than the Fermi energy for a given confinement V_{SG}.

From figure 4.10, we can see that the effect of the Coulomb interactions on the propagation velocities is very strong, and strongly increases its value. At this point, it is essential to emphasise that the matching between the experimental data and the simulation is a strong indication, that what we are measuring is a collective effect, generated when we apply the voltage pulse at the Fermi sea. This is in agreement with the proposal from Matveev and Glazmann [116], where they calculated the plasmon velocity generated by a local change of the density in a coupled system. The voltage pulse generates this local change in the density.

Therefore, we are not exciting Landau-quasiparticles that travel with the Fermi velocity. Nevertheless, the correct mindset for coupled 1D-systems is based on the consequences of the Luttinger-liquid model, which results in collective modes [104, 108, 109, 116]. Thus

we have characterised the velocity an electron wave packet, created by applying a voltage pulse to the Fermi sea. Furthermore, we have shown a manner to control this velocity of this excitation by reducing the number of conductance channels. Moreover, we create an excitation that follows the bosonic statistics, in our case a plasmon, formed by a local variation in the electron density, which are fermions.

4.4 Velocity control via QPC selection

The voltage pulse applied to the Fermi sea becomes a collective excitation spread over the channels of conductance (separated by energy). When we change the confinement, we are also changing the number of available channels in the whole quasi-1D conductor, and to have the lowest velocity, we need to have the minimum number of channels available (stronger confinement). However, when we increase V_{SG}, the wave packet is distorted, as shown in figure 4.6. This effect is probably due to inhomogeneities in the quasi-1D conductor.

To achieve the situation of a single-channel of conductance we will use a different strategy. Instead of changing the confinement in the entire conductor, we use QPC_0 located at the entrance of the quasi-1D conductor, as shown in figure 4.11. We can set the QPC_0 at the first plateau of conductance. Therefore, we have effectively one channel being transmitted. The situation in the conductor is the following: We will have N channels of conductance available before and after the constriction (QPC_0). At the constriction, however, the passage is limited to only a single-channel of conductance as represented in figure 4.11. In that figure, the wave functions are limited to three available channels.

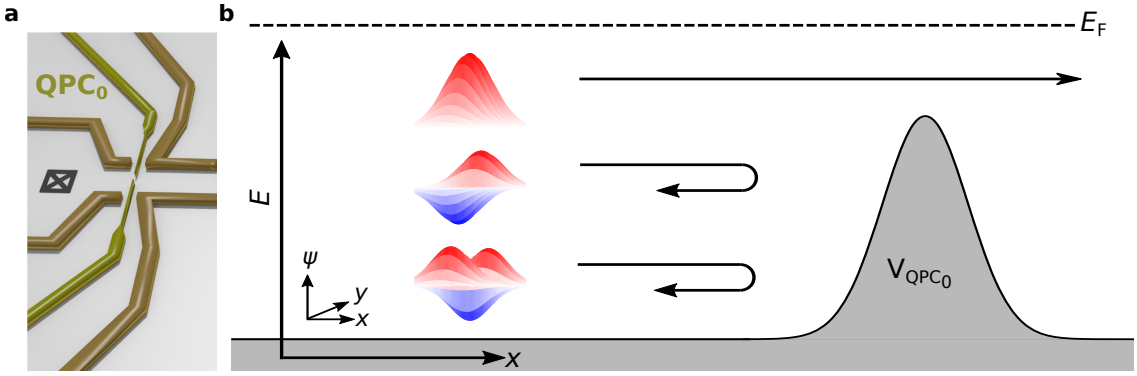

Figure 4.11: QPC effect on the quasi-1D conductor. a, Schematic of the sample, where we show the injection ohmic contact and the QPC_0 used to locally reduce the number of channels of conductance. **b,** Representation of the wave function of the channels of conductance before and after the QPC constriction (only three represented). At the QPC_0 position only one channel of conductance is transmitted.

We plot in figure 4.12 the time-resolved measurements at QPC_1 with QPC_0 set to the first plateau of conductance. The distance between these two QPCs is of 10 µm.

The black data corresponds to the time-resolved trace when we do not polarise QPC_0. One can see a substantial increase in the time-of-flight. We observe a similar increase in the time-of-flight measured after 20 µm.

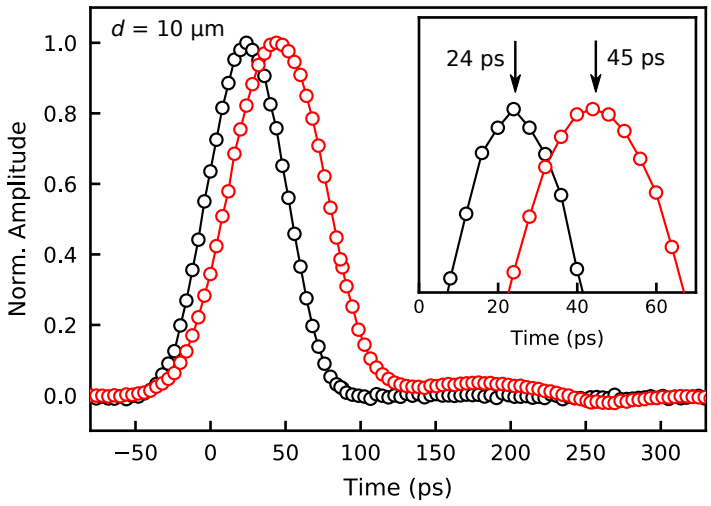

Figure 4.12: Time-resolved trace polarising QPC$_0$. The signal is measured at QPC$_1$ after a distance d =10 µm. The black curve corresponds to the measurement when QPC$_0$ is not polarised, and the red curve corresponds to the situation when QPC$_0$ is polarised at the first plateau of conductance. The data was taken with $V_{SG} = -1.0\,V$.

Similar to what we have discussed in the last section, we have repeated the time-of-flight measurements for different confinement, having QPC$_0$ fixed at the first plateau and perform the time-of-flight measurements at QPC$_1$. To calculate the velocity, we had to follow a different approach. The excitation should spend a certain time t_0 to go from the ohmic contact until the QPC$_0$. This value is independent whether QPC$_0$ is polarised or not. By subtracting the time-of-flight measured having QPC$_0$ polarised from the time-of-flight without polarising QPC$_0$, we eliminate t_0. The difference between the two times-of-flight now depends only on the different average velocities between the two QPCs. Since we have already characterised the velocity of the excitation when QPC$_0$ was not polarised, the new velocity can be determined by the equation:

$$T_{\mathrm{QPC_1\ (QPC_0\ at\ 1st\ plateau)}} - T_{\mathrm{QPC_1\ (QPC_0\ unpolarized\ )}} = \frac{d_{\mathrm{QPC_0\text{-}QPC_1}}}{v_{\mathrm{QPC_0\text{-}QPC_1}}} - \frac{d_{\mathrm{QPC_0\text{-}QPC_1}}}{v_{\mathrm{plasmon}}} \quad (4.3)$$

where $d_{\mathrm{QPC_0-QPC_1}}$ is the distance between QPC$_0$ and QPC$_1$, $v_{\mathrm{QPC_0-QPC_1}}$ is the average velocity between the QPCs when QPC$_0$ is polarised and v_{plasmon} corresponds to the velocity of the charge mode measured before (see figure 4.10), without polarising QPC$_0$.

We plot the velocities derived from these measurements in figure 4.13. The red (green) circles correspond to the case when QPC$_0$ is polarised at the first (second) plateau of conductance. The blue circles and the blue line are the velocity of the electron wave packet are shown for comparison and which correspond to the data of figure 4.10.

The velocities of the pulse when passing through QPC$_0$ set at the first plateau are

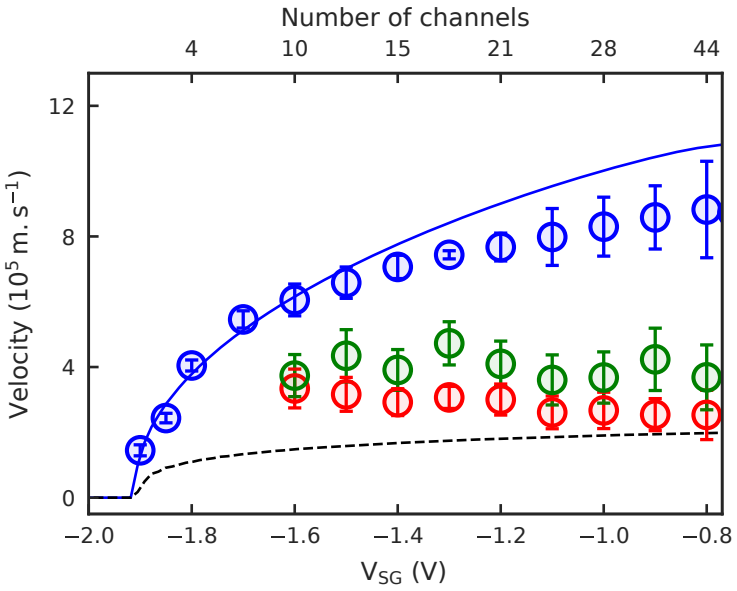

Figure 4.13: Velocity of an electron wave packet using a QPC barrier. The red (green) circles correspond to the measured propagation velocities when QPC_0 is polarised at the first (second) plateau of conductance. The blue data is (see fig. 4.10) is shown for comparison.

much smaller than when QPC_0 is unpolarized. The consequences of the plasmon theory is that the velocity of the charge mode grows with the number of channels, as discussed in chapter 2. Since we observe a reduced velocity, it looks like that the QPC_0 acts like if it were reducing the number of channels over which the plasmon is spread, thus reducing the velocity. The natural question that emerges from this effect is: is this reduction of the velocity localized at the QPC_0? Or is the plasmon changed such that the velocity is reduced during some propagation length?

One possibility of the slowing down of the wave packet could be due to a local change in density due to OPC_0. As the density controls the Fermi velocity, one expects a local change in propagation velocity. To evaluate this effect, we assume that the pulse after entering the quasi-1D conductor propagates with velocity v_1, which is the same velocity for the wave packet when we do not use the QPC_0 barrier. Therefore, v_1 is equal to the plasmon velocity v_{plasmon} measured before (blue circles in figure 4.13). Then, close to the QPC, the excitation would slow down over a distance δ, as schematised in figure 4.14. The wave packet would then propagate over an effective length 2 δ around the QPC_0 barrier with a reduced velocity v_0. After having passed the effective length of the QPC_0, the pulse would re-accelerate until it reaches again v_1. This will happen over a certain length δ. The variation of the velocity gives a different time-of-flight when the QPC barrier is activated, which we will refer to as τ. To calculate the new average velocity v^*, we compare the time-of-flight with and without the QPC_0 barrier until the detector. Therefore, the new average velocity v^* is equal to:

$$v^* = \frac{D_1}{\tau - t_0} \tag{4.4}$$

where $t_0 = D_0/v_1$ is the time of propagation until the QPC_0 barrier, when the barrier is not activated. D_0 is the distance from the source until the QPC barrier. D_1 is the distance from the QPC barrier until the detector. Considering the different velocities at the different segments, as shown in figure 4.14, we find that τ is equal to:

$$\tau = \frac{D_0 - 2\delta}{v_1} + 2\frac{\delta}{v_0 + v_1} + 2\frac{\delta}{v_0} + 2\frac{\delta}{v_0 + v_1} + \frac{D_1 - 2\delta}{v_1} \tag{4.5}$$

$$= \underbrace{\frac{D_0 + D_1}{v_1}}_{\text{Time-of-flight without the barrier}} + 2\delta\left(-\frac{2}{v_1} + \frac{2}{v_0 + v_1} + \frac{1}{v_0}\right) \tag{4.6}$$

Putting equation 4.4 and 4.6 together we find:

$$v^* = \frac{D_1}{\frac{D_1}{v_1} + 2\delta\left(-\frac{2}{v_1} + \frac{2}{v_0+v_1} + \frac{1}{v_0}\right)} \tag{4.7}$$

we use equation 4.7 to fit the average velocity measured setting QPC_0 at the first plateau, as shown in figure 4.13 (red circles). The fitting parameter is the velocity v_0. we have considered an active length 2δ, with δ =250 nm over which the velocity of the wave packet is reduced to v_0. This value is around five times the width of the QPC. We are taking this large value of delta such that the fitted velocity v_0 is maximally overestimated. We plot the new average velocities $v^\star$ found with our fit in figure 4.14. It corresponds to the grey triangles.

The result of the fit for the reduced velocity $v_0 \approx 2.3 \times 10^4$ m/s. To evaluate this model, we have used the velocity v_0 obtained from the fit, but considering a longer distance between the QPC barrier and the detector ($D_1 = 40\,\mu m$). In this case, the barrier is QPC_2, and the detector is QPC_3. The result of the model and the experimental data are shown in figure 4.14. For a longer length, the error of this model becomes larger and larger. Therefore this model[1] can be ruled out, although it should have a contribution to the reduction of the velocity. It also indicates that the effect of QPC on the propagation of the pulse it is not something that happens just locally, but has a deeper origin. In the next section, we describe another model to get a better understanding of the effects of the QPC in our system.

1 Credits to Michele Filippone

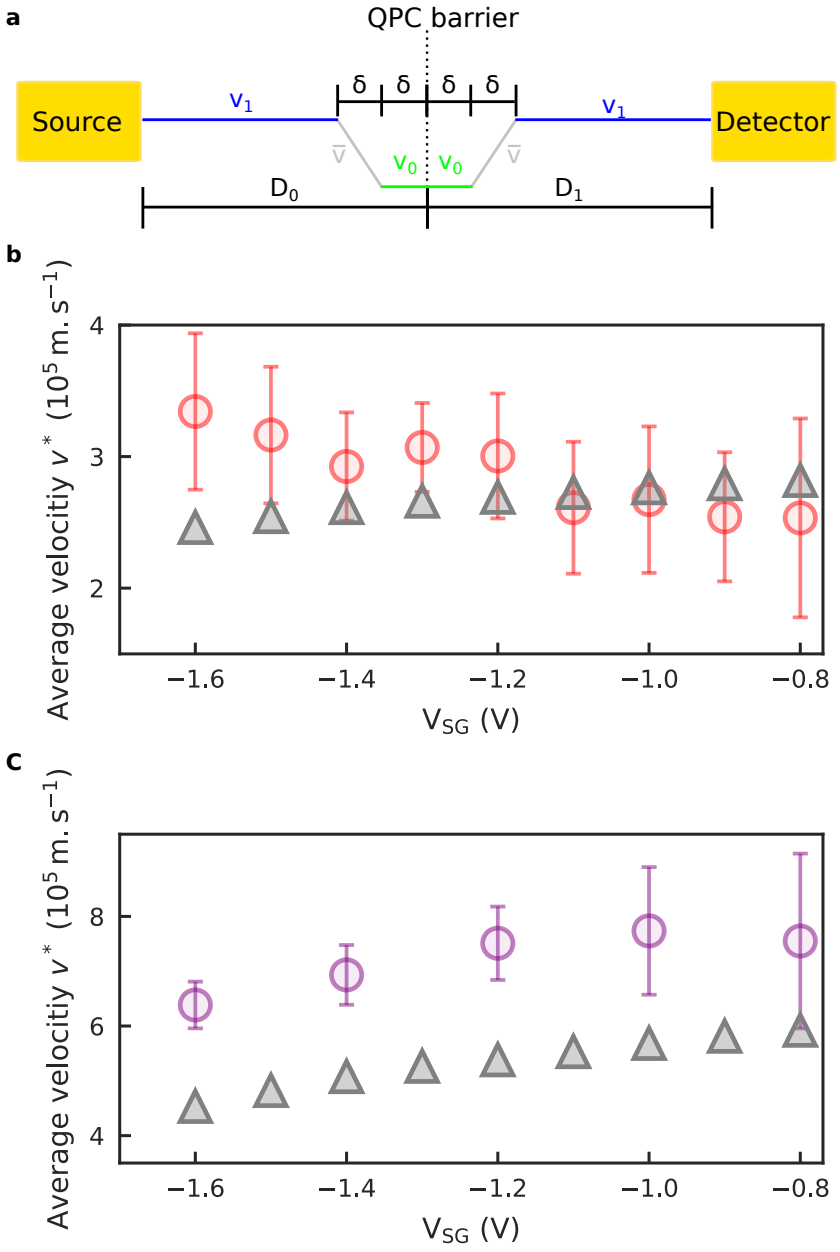

Figure 4.14: Average velocity v^*. a, Schematics of a model, where the electron wave packet is slowed down by the potential barrier (QPC_0). **b,** The red circles correspond to the average velocity measured when the QPC_0 is polarised at the first plateau. The grey triangles are the velocities v^* derived from fitting the red data with equation 4.7. **c,** Plot of the average velocity v^* considering the distance $D_1 = 40\,\mu m$, using the velocity v_0 estimated in **b**. The grey triangles are the velocity estimated from the model, and the purple circles are the experimental data.

4.4.1 Modelling the effect of the QPC

To understand how the QPC affects the plasmon mode, we model the QPC in two ways, taking into account that the generalized Luttinger liquid theory provides two information: The velocity v_P^a of each mode a and the decomposition $\tilde{n}_{a\alpha}$ of mode a as a function of the single-particle state (channel) α. We investigate two different scenarios – the funnelling and filtering scenario – and calculate the resulting propagation velocity for both of them. In both cases we assume that the ohmic contact populates all channels equally, considering the initial weight of the mode a as $c_a = \sum_\alpha \tilde{n}_{a\alpha}$, where $\tilde{n}_{a\alpha}$ is the contribution of channel α to the mode a. The value c_a represents the charge carried by each mode. These calculations were done in collaboration with Pacome Armagnat in the group of Xavier Waintal.

Funnelling scenario

Let us consider that the QPC set at the first plateau funnels the created excitation at the ohmic contact. In this *funnelling* scenario a transformation of the plasmon occurs at the QPC. The plasmon that was spread over the N available channels in the waveguide is projected into a single channel. Then, it behaves as a plasmon hosted by a single channel.

Let us consider that part of the injected charge is reflected at the QPC. However, we are not interested in the absolute value of the current, but only in the relative weight of the different modes. We can estimate the value of the measured signal at distance d as:

$$S(t) \propto \sum_{a=0}^{N-1} c_a f\left(t - \frac{d}{v_P^a}\right) \tag{4.8}$$

Where $f(t) = \exp(-4\log(2)t^2/\Gamma^2)$ is the Gaussian pulse used to inject the charges with FWHM $= \Gamma = 70\,\text{ps}$. The velocity v_P^a in equation 4.8 will be modified by the presence of the QPC at the first plateau. By considering that the excitation is guided into a single channel, one could consider that the plasmon would be created as if there was only one available channel in the quasi-1D conductor. This is equivalent to truncate equation 2.24 (in chapter 2) to a 1x1 dimension before diagonalising the matrix to calculate the renormalised velocities.

Then, the measured signal should be proportional to:

$$S(t) \propto f\left(t - \frac{d}{v_P^{(1\times1)}}\right) \tag{4.9}$$

The simulations of equations 4.8 and 4.9 are presented at the upper part of figure 4.15 **a**, **b** and **c**. The features presented in the time-resolved signal without polarizing the QPC_0 for time higher than 200 ps are related to the neutral modes.

Recalling the results derived in chapter 2 tells us that the velocity of the charge mode increases with the number of available channels. Therefore, the velocity of the charge mode formed in a single channel is reduced in comparison to the plasmon formed by several channels. Moreover, for the actual scenario, the velocity of the charge mode will depend only on the number of channels of conductance available in the QPC. Thus the velocity is independent of the number of single-particle states available in our quasi 1D-conductor.

Filtering scenario

Let us consider once more that the QPC_0 set at the first plateau of conductance. In the filtering scenario, we assume that the QPC_0 acts only allowing the transmission of the plasmon components carried by channel 0. Once passed the QPC_0, the concentrated in channel 0 is redistributed over all available channels. Therefore, it develops in the charge and neutral modes. At determined QPC, for example at QPC_1, this charge distribution is projected onto a single-particle state and measured.

As aforementioned, we consider the $\tilde{n}_{a\alpha}$ is the decomposition of the mode a as a function of the channel α. The weight of the different modes is $c_a = \sum_\alpha \tilde{n}_{a\alpha}$, where the weight sort of indicates the charge carried by each mode. The charge mode is equally distributed over all the channels. On the other hand, the neutral modes are spread over the channels with positive and negative contributions, such that the sum is almost zero. Let us consider that c_0 is the charge mode, and since all the other channels are roughly neutral, thus $c_0 \gg c_a, \forall a \neq 0$. Assuming that the QPC_0 only allows the transmission of the contributions $\tilde{n}_{a\alpha}$ present at $\alpha = 0$, this implies $c_a = \tilde{n}_{a0}$. Therefore, the weight of the charge mode will be reduced in comparison to the neutral modes. To consider this effect due to the QPC_0, it corresponds to add an extra factor $\tilde{n}_{a0}$ in the expected signal. Hence, the signal expected just because we are using a QPC to time-resolved our signal is proportional to:

$$S(t) \propto \sum_{a=0}^{N-1} c_a \tilde{n}_{a0} f\left(t - \frac{d}{v_P^a}\right) \tag{4.10}$$

The factor $\tilde{n}_{a0}$ appears because we need to use another QPC to perform the time-resolved measurements, which projects the excitation to the single-particle state.

We can take into account the effect of the QPC_0, set to transmit a single channel, then the expected signal becomes:

$$S(t) \propto \sum_{a=0}^{N-1} c_a (\tilde{n}_{a0})^2 f\left(t - \frac{d}{v_P^a}\right) \tag{4.11}$$

We present the results of the simulations for equation 4.10 and 4.11 in the bottom part of figure 4.15 **a**, **b** and **c**.

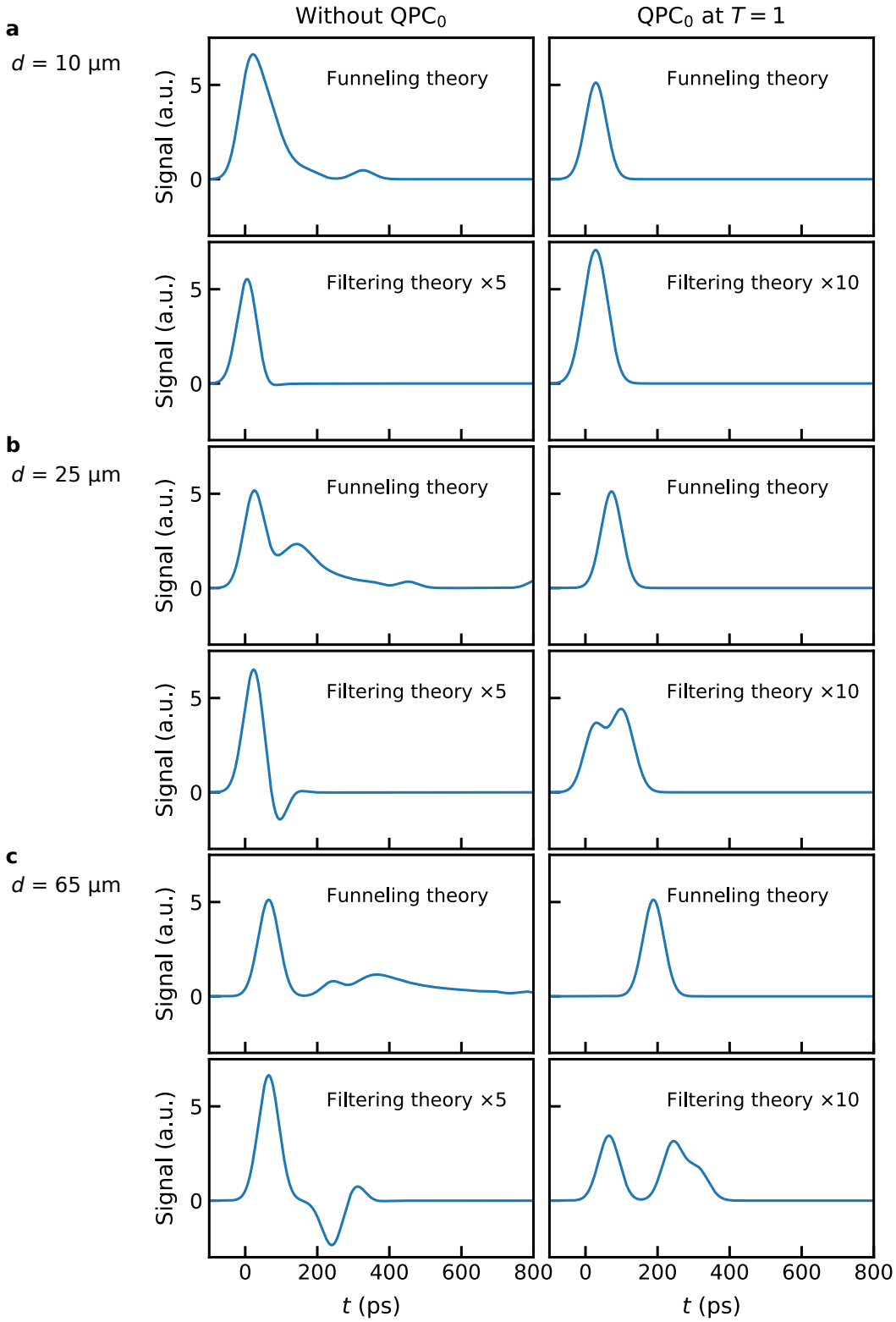

Figure 4.15: Funneling vs Filtering scenario. Time-resolved signal of the propagation of the wave packet for two different scenarios (Funnelling and Filtering) and for two cases (polarized or un-polarized QPC_0). All the curves were simulated considering $V_{SG} = -1.0\,V$ for a distance $d = 10\,\mu m$ **a**, d = 25 µm **b** and d = 65 µm **c**.

In figure 4.15, we plot the expected signal for the two different scenarios, considering the propagation over different lengths. For the shortest distance, $d = 10\,\mu m$ with QPC_0 at the first plateau (T=1), we observe a single wave packet for both scenarios. This effect is compatible with the experimental result shown in figure 4.12. The signal for the filtering scenario is slightly wider. Thus, it would agree a little better with the measured wave packet. Considering the length of 25 µm, we observe a splitting of the resolved a wave packet into two wave packets for the filtering scenario. This separation happens because the neutral modes travel at a slower velocity than the charge mode. On the other hand, this effect is not present in the funnelling scenario, where we observe a single wave packet. After a distance of 65 µm, we observe two wave packets which correspond to a full separation of the charge mode and the neutral modes for the filtering scenario. The signal for the neutral mode, which arrives later, is broader because the neutral modes propagate at slightly different velocities.

We present the time-resolved trace measured having QPC_0 at the first plateau and measuring after a distance of 25 µm in figure 4.16.

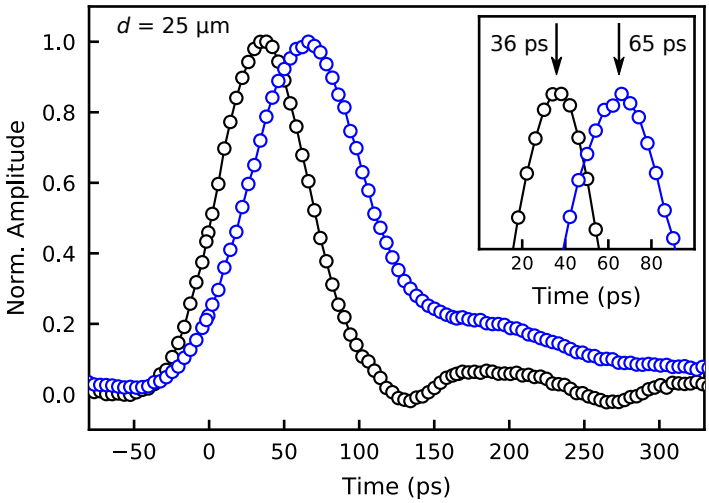

Figure 4.16: Time-resolved trace polarising QPC_0. The signal is measured at QPC_2, where the distance $d = 25\,\mu m$ corresponds to the distances between QPC_0 until QPC_2. The black curve corresponds to the measurement when QPC_0 is not polarised, and the blue curve corresponds to the situation when QPC_0 is at the first plateau of conductance. The data was taken with $V_{SG} = -1.0\,V$.

Comparing the two simulated signals with the time-resolved traces in QPC_1 (figure 4.12) and in QPC_2 (figure 4.16), lead us to conclude that the funnelling scenario describes better our experimental data.

To get a more quantitative comparison, we plot the calculated velocities for the funnelling scenario versus the confinement in figure 4.17 in addition to our experimental data. The agreement between the experimental results and the simulated velocities is quite remarkable, especially when considering that we do not have any adjustable parameter. This is confirmed

when repeating the same experiment with the only difference that the funnelling QPC is set to transmit two channels as shown by the green data point in figure 4.17.

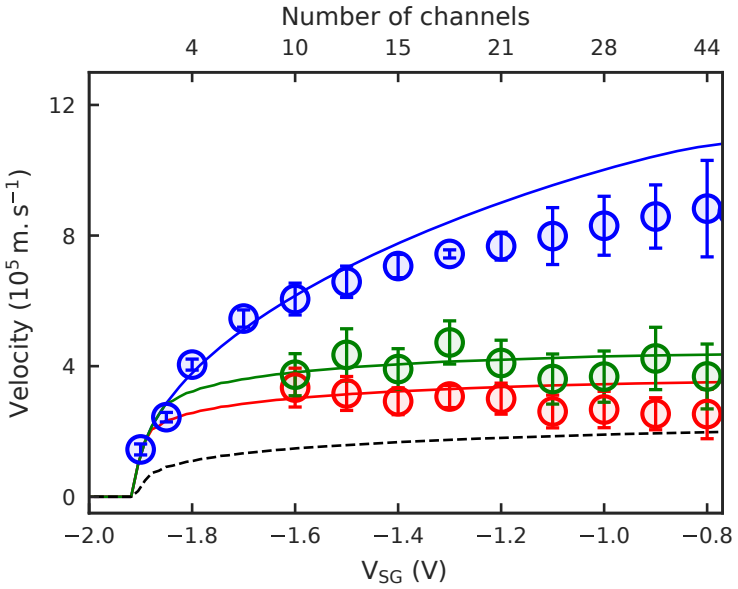

Figure 4.17: Velocity using QPC_0 set to T=1 and T=2. The blue circles are experimental data for 4.10. The red circles (green circles) correspond to the measurement of time-of-flight at QPC_1, when $QPC_0 = 2 \cdot e^2/h$ $(4 \cdot e^2/h)$. The red (green) line corresponds to the self-consistent simulation, considering the velocity derived from the truncated equation 2.24 for 1 or 2 channels.

This investigation can be generalized to an arbitrary conductance of the *funnelling* QPC. We have measured the time-of-flight at QPC_1 by varying the voltage of QPC_0 and plot the deduced propagation velocity of the wave packet in 4.18 as grey circles. The confinement of our waveguide has been fixed to $V_{SG} = -1.0\,V$.

Once more, we see a monotonic increase in the velocity when reducing the confinement potential. However, this time the voltage is applied to a local constriction (QPC_0) with a width of few tens of nanometres, instead of the confinement gates, that form the quasi-1D channel. One remarkable feature present in figure 4.18 is the continuous control of the velocity as a function of voltage on the QPC_0. The velocity can be controlled from the case where there is a single channel being transmitted (slowest), until the fastest case when we do not polarise the constriction (QPC_0) on our waveguide.

In order to compare the experimental data of fig.4.18 with our funnelling theory, we have to convert the channel number of the "funnelling" QPC into gate voltage. This is done in the following way: first, we measure the pinch-off curve of the QPC_0, that means, the current going through the sample versus the applied voltage on the QPC V_{QPC_0}. Then, we convert the measured current to conductance. We show the data of conductance as a function of the applied voltage in figure 4.19.

We take the voltages at which the conductance is an integer of $2e^2/\hbar$. We plot these

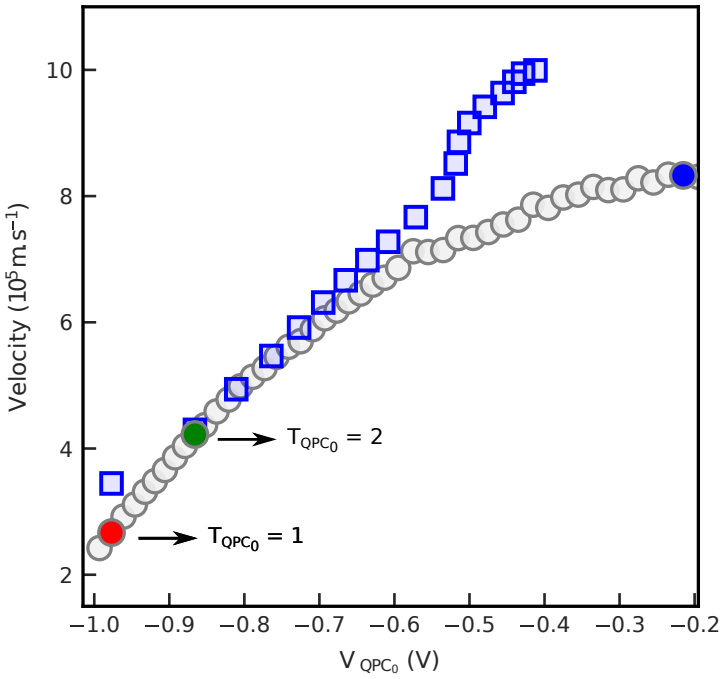

Figure 4.18: Velocity varying transmission of the QPC barrier. The data was taken with $V_{\mathrm{SG}} = -1.0\,\mathrm{V}$. The grey circles are the experimental velocities. The coloured circles correspond to $V_{\mathrm{QPC}_0} = 2 \cdot e^2/h$ (red), $4 \cdot e^2/h$ (green) and fully depolarized (blue). The blue squares correspond to the plasmon velocity for an integer number of channels.

values with the hexagonal marker in fig. 4.19 **a**. In figure 4.19 **b** we plot these symbols again. However, we invert the axis of the plot (V_{QPC_0} versus the conductance).

To finish, we interpolate the hexagonal markers to find a function that predicts the voltage in QPC_0 for a certain number of channels. We plot the interpolation as a dashed line in figure 4.19 **a**. The middle of the plateau corresponds to the integer number of conductance, as shown in figure 4.19 **a**. However, as we have more and more channels of conductance available, the plateaux get smoothed out. This means that our interpolation will be suitable for a small number of channels, but it is not so precise for the case when we have many channels of conductance available. We use this interpolation to convert the results of the parameter-free simulation of the *funnelling* scenario, that is, velocities versus the number of channels, to velocities versus the voltage in QPC_0 V_{QPC_0}. The results are plotted in figure 4.18.

The blue squares are the velocities calculated from the simulation, and the grey circles are the experimental data. Once more, we have a good agreement for strong QPC confinement, that stands for a plasmon propagating over a small number of channels. The data does not match for a high number of channels, similar to what has been shown in figure 4.10, most probably due to the fact that the simulation does not take into account any forward scattering.

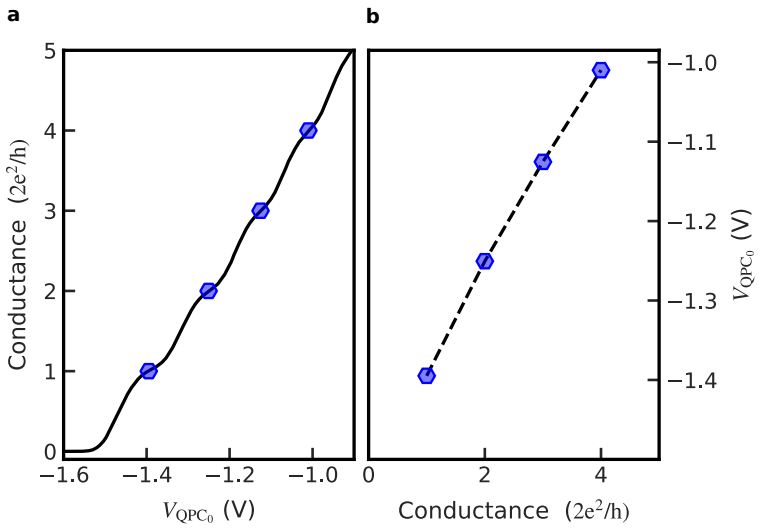

Figure 4.19: Pinch-off of QPC$_0$. a, The black line is the conductance versus the applied voltage in the QPC$_0$ V_{QPC_0}. The other gates were not polarised. The hexagonal markers correspond to the positions in which the conductance is an integer of $2e^2/\hbar$. **b,** Inversed plot of **a**. The hexagonal markers are the same as in **a**. The dashed line is an interpolation of the hexagonal markers. The data was taken with $V_{SG} = 0\,V$.

In summary, we have shown that with a local constriction, in our case, a QPC, we can control the velocity of the plasmon. Considering two different hypotheses of the role played by the QPC and comparing to the time-resolved measurements, we conclude that we can tune our system such that it behaves like a clean single-channel Luttinger-liquid. Changing the voltage in the barrier, we can go from this single channel regime into a multi-channel Fermi liquid in a non-chiral system. Finally, we did not observe a significant change in the time-of-flight after 65 µm, even having the QPC$_0$ polarised at the first plateau. That means, the system behaves like a clean single-channel for a length of more than 20 µm. At longer distances, the excitation repopulates the available channels. This effect will be in the next section.

Time evolution of the electron excitation – Studying the relaxation length

In the preceding section, we have seen that the electron wave packet slows down considerably when passing through a QPC. With our sample, we have the possibility to measure the time-of-flight at a different positions along the quasi-1D conductor. As mentioned above, we also observe a significant increase in the time-of-flight at a distance of 25 µm (QPC2). In this section, we study the arrival time as a function of distance, where we can use the different QPCs available in our sample. We show the different possible length between the QPCs in figure 4.20. We can use one QPC to transmit a fixed number of channels, thus modifying the plasmon. For instance, we can set QPC$_a$ to transmit a single channel, resolving the wave packet at QPC$_b$.

What we experimentally observe is that the electron wave packet regains its original speed after a propagation length of about 70 µm. In figure 4.21, we show the data of the

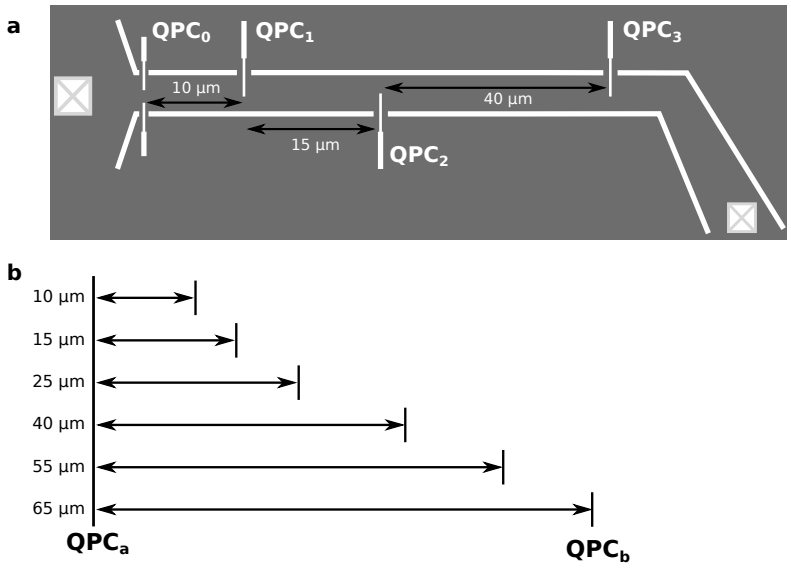

Figure 4.20: Distances between the QPCs. a, Schematic of the sample with the distances between the QPCs. **b,** Length of all possible combinations between two QPCs.

average velocity at various propagations distances and for different confinement potentials.

These data points have been obtained by using all possible combinations of 2 QPCs. One of the QPCs is used as a local barrier. We always set this QPC to transmit a single-channel of conductance. A second QPC is used as a sampling QPC. With all the combinations, we can cover the distances of 10, 15, 25, 40, 55 and 65 µm as shown in figure 4.20.

We observe that for a length of 10 µm the velocities are quite the same for all confinements. Between 10 and 25 µm, we can see that the velocity increases slowly, before a relatively sharp increase in the velocity that happens between 25 µm and 40 µm. For the propagation length of 40 µm and above, the velocities approach the ones of the plasmon velocity (blue curve in figure 4.17). This increased velocity indicates that after a long-distance, all the channels are repopulated.

According to our findings, we suspect that this "relaxation" process could be due to some impurity scattering. The fact that this effect is enhanced for stronger confinement supports this assumption. The probability for the excitation to find a scattering source is increased for a stronger confinement since it has less space to propagate within the quasi-1D wire.

We also verified the influence of the amplitude used to create the excitation for these measurements as well as the influence of the confinement potential as shown in figure 4.21. We can see that there is no change in the velocity for different amplitudes, what leads us to conclude that the relaxation effect, in this case, does not depend on the number of charges injected at the ohmic contact.

We also plot the result of a different experiment on the right panel of figure 4.21, where we set two QPCs at the first plateau, in this case, QPC_0 and QPC_1. By doing so, we can verify whether it is possible to decrease the average velocity by re-projecting the excitation into single-particle states repeatedly. This behaviour is confirmed in figure 4.21, noting

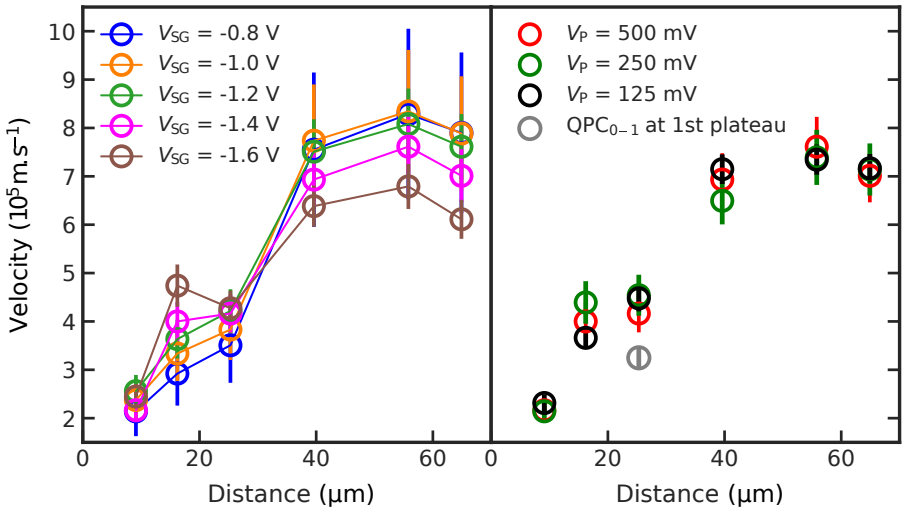

Figure 4.21: Average velocity after a QPC barrier. left, Velocity for different propagation lengths calculated from the TOF and for various confinement potentials. The amplitude V_P of the voltage pulse at the output of the AWG generator is equal to 500 mV. **right,** Velocity for different distances and for different amplitudes V_P. The quasi-1D conductor was polarised with $V_{SG} = -1.4$ V. The grey circle corresponds to the case where QPC_0 and QPC_1 were polarised at the first conductance plateau.

the reduction of the average speed. In this case, we use QPC_2 to measure the TOF. The distance to calculate the TOF is taken from QPC_0 until QPC_2.

The way that the relaxation process takes place repopulating the other channels is still an open question. Presently, we are performing time-resolved simulations in collaboration with the group of Xavier Waintal to see whether the scattering hypothesis can explain our experimental data.

We can, however, make an analogy with the quantum Hall system where an electronic excitation is injected into a single edge channel in the presence of several co-propagating edge channels.

Let us consider the simplest system of two co-propagating edge channels. Suppose a charge is injected in one of the edge channels, the electron charge will fractionalize due to the Coulomb interactions between the two channels.

This fractionalisation effect was measured recently by the ENS group [146] as well as the Tokyo group [111] with time-resolved measurements. In ref. [146], this fractionalisation process has been measured using Hong-Ou-Mandel interferometry, using edge channels as the waveguide for the electrons. The fractionalization has been measured after a length of only 3 µm [146]. Analysing their data implies that the fractionalisation mechanism has to occur instantaneously after the injection of the electron wave packet. This is in contrast to our system where we see almost no change in the propagation velocity up to distances of 20 µm.

One has to keep in mind the differences between the use of chiral co-propagating edge

channels and our non-chiral system. In the first, the channels of conductance are spatially separated. On the other hand, in our system, the channels are separated in energy and not spatially. Even though the Coulomb interactions are responsible for the coupling in both systems, we observe important differences in the way that the fractionalisation takes place.

Determination of the propagation velocity from an electronic cavity

When measuring the time-resolved traces of the wave packets beyond a distance of 65 µm after a QPC set to transmit a single-channel, we observe a beating pattern in the time-resolved trace after the main peak with a distinct frequency as shown in figure 4.22.

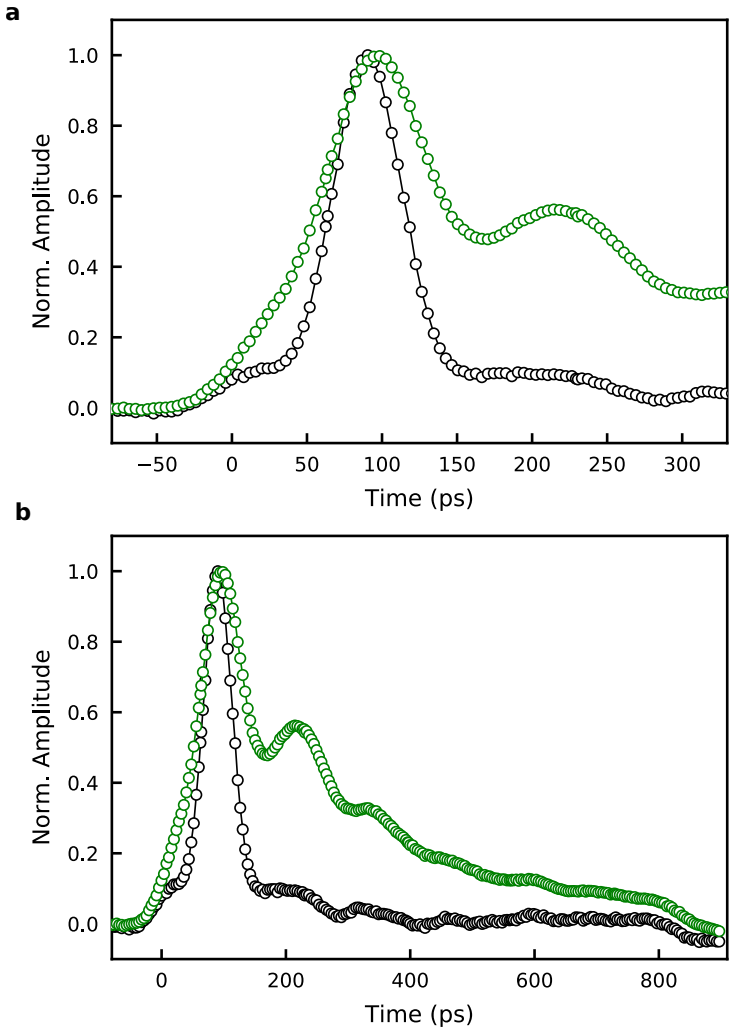

Figure 4.22: Time-resolved measurements at QPC_3. a, The green data was measured polarising QPC_0 at the first plateau, and the black data was measured without polarising the QPC_0. **b,** We show the time-resolved trace of **a**, but with a larger time range.

These additional peaks resemble Fabry-Pérot resonances, meaning that we form an electronic cavity with the two polarised QPCs. There is a probability that the pulse will be

transmitted or reflected at each QPC, which results in a beating pattern after the arrival of the main peak of the Gaussian wave packet.

We can use a Fabry-Pérot model to determine the time separation between the peaks. This separation should give the time-of-flight of a round trip inside the cavity. Therefore, we can calculate the average velocity of the round trip. We apply a simple model, considering a Gaussian pulse that can be transmitted or reflected on the QPCs with a certain probability and that the time separation is constant.

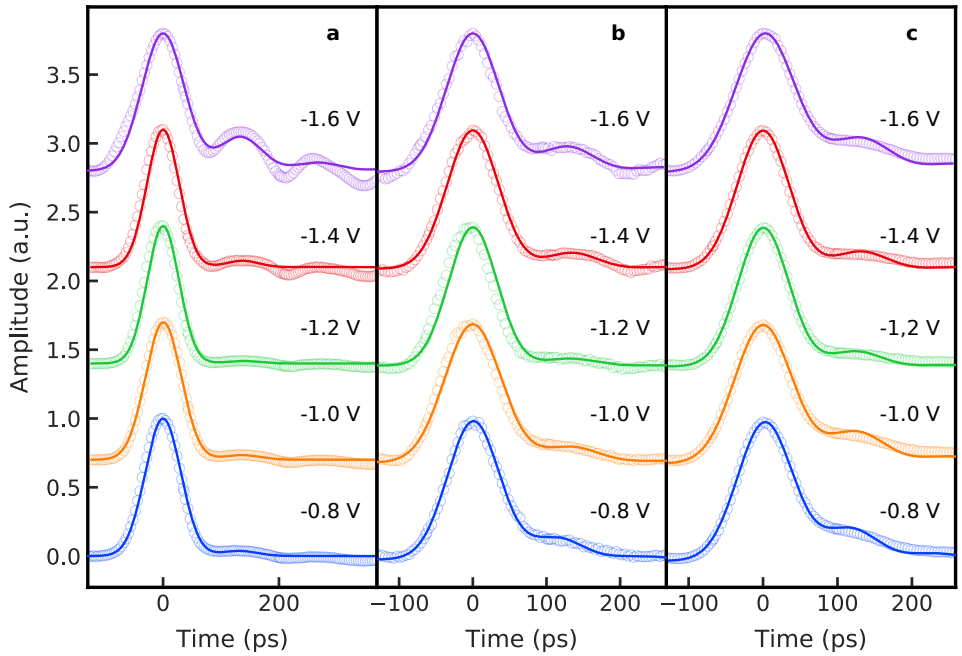

Figure 4.23: Time-resolved trace within the electronic cavity. The different colours for the data points going from blue to purple correspond to different confinements, ranging from $V_{\mathrm{SG}} = -0.8\,\mathrm{V}$ to $-1.6\,\mathrm{V}$. The coloured lines correspond to equation 4.12 using the fitted parameters. The parameters are shown in appendix F. The length of cavity is 10 µm, 15 µm, 25 µm for **a**, **b** and **c**, respectively.

To minimise the number of fitting parameters, we work with renormalised amplitudes, where we fitted the following function:

$$f(t) = \sum_n R^n \cdot e^{-\frac{1}{2}(t-\tau_0-n\cdot t_{\mathrm{separation}}/\sigma)^2} \tag{4.12}$$

where R, τ_0, $t_{\mathrm{separation}}$ and σ are the fitting parameters. R is proportional to the reflection coefficients of the QPCs, τ_0 and σ are the position of the first Gaussian and its widths, and $t_{\mathrm{separation}}$ is the time separation among the different Gaussians. The sum is made up to a number n of Gaussians until no further improvement of the fit is obtained. The derivation of equation 4.12 is presented in appendix E and the fitted data of the time-resolved measurements is shown in figures 4.23 and 4.24.

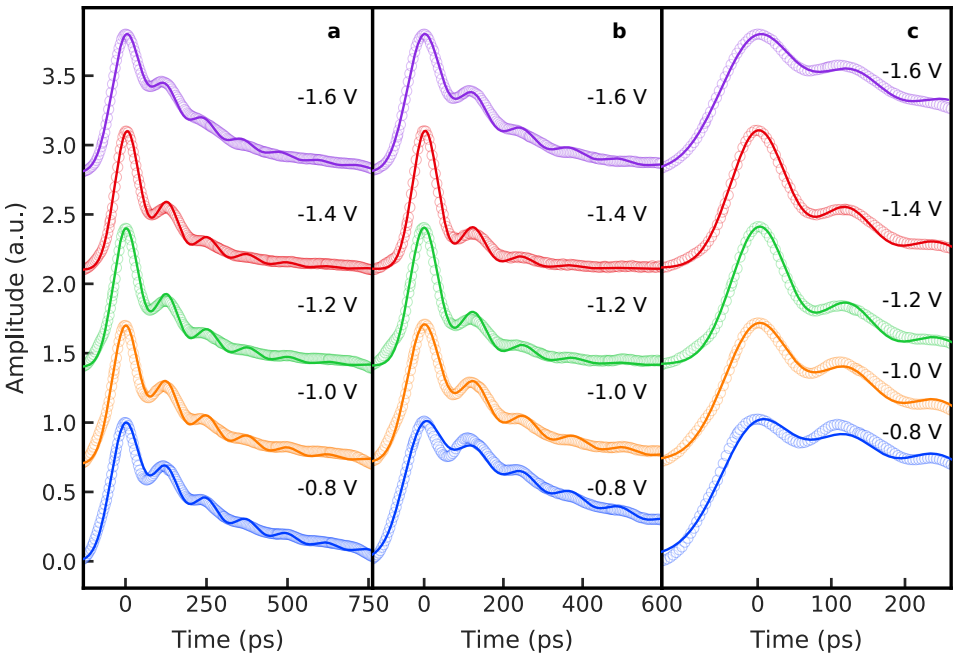

Figure 4.24: Time-resolved trace within the electronic cavity. The different colours for the data points going from blue to purple correspond to different confinements, ranging from $V_{SG} = -0.8\,V$ to $-1.6\,V$. The coloured lines correspond to equation 4.12 using the fitted parameters. The parameters are shown in appendix F. The length of cavity is 65 µm, 55 µm, 40 µm for **a**, **b** and **c**, respectively.

We observe enhanced features in the cavity formed with higher confinement and more extended length. The fits usually show more pronounced features than the data. The time-resolved traces measured in QPC_3 show good agreement with the fit in figure 4.24, at least for the first and second round trip between the two QPCs barriers. This agreement allows us to extract a reliable value for $t_{separation}$. The full width at half maximum (FWHM) varies between 70 ps and 90 ps for the fitted data in figure 4.23. For the fit in figure 4.24, the FWHM varies between 80 ps and 115 ps. It can be, that there is some dispersion occurring in the process of the repopulation of the single-particle states. We show the results of all the fitted parameters in appendix F.

The results of the velocity calculated from the $t_{separation}$ versus the distance are plotted in figure 4.25, where the distances correspond to a complete round trip between the QPCs. We also show data for different confinements. Remarkably, the values of the velocity are very similar, independently from the confinement V_{SG}. This result is different from what we have found for the plasmon velocity within our long quasi-one-dimensional wire. We observe a linear increase of the velocity with the distance. The speed at the largest distance, with the highest confinement, is quite surprising. This value is much higher than the plasmon velocity for this confinement, which is shown with the blue circles in figure 4.17.

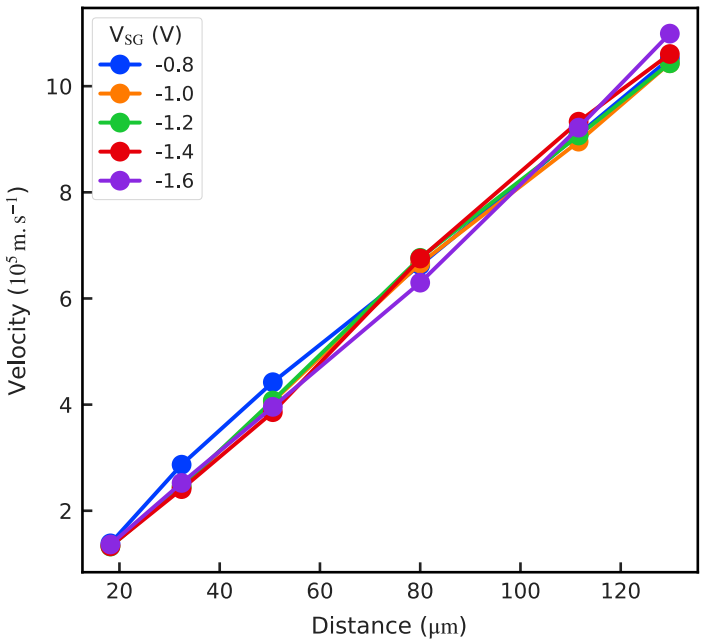

Figure 4.25: Velocity of the wave packet within an electronic Fabry-Pérot cavity. Propagation velocities derived from the time-of-flight measurements within the Fabry-Pérot cavity for different cavity length.

For the moment, we do not have a precise explanation for this effect. We can speculate that it is related to the relaxation process itself since the plasmon travels with a slower velocity for some length, and at some point starts to accelerate. Finally, the plasmon reaches a very high speed when arriving after 65 µm, which is similar to the one of the plasmons that were not slowed down, as shown in figure 4.17.

4.5 Conclusion

In this chapter, we have presented time-resolved measurements at the picosecond level of electronic excitation propagating at the surface of the Fermi sea. We determined the velocity of propagation of such excitations through time-of-flight measurements of the electrons in a quasi-1D quantum conductor. It turned out that the velocity of such an electronic excitation is much higher than the Fermi velocity. Despite the Fermionic statistics of electrons, we have shown that a local perturbation of the electron density results in the creation of a bosonic excitation – a plasmon.

A parameter-free self-consistent simulation solving the quantum-mechanics-electrostatic problem of our system explains with good accuracy the velocities found experimentally. Indeed, the origin of the increased velocity compared to the non-interacting system is due to Coulomb interactions. To our knowledge, this is the first observation of the plasmon

velocity in an electron waveguide defined by Schottky gates and at zero magnetic fields.

We showed that the plasmon velocity can be controlled by varying the confinement potential of our electron waveguide. Our results agree qualitatively with a theory initially developed by Matveev and Glazmann, predicting that the plasmon velocity would be proportional to $v \propto \sqrt{N}$ [109], where N is the number of channels of conductance in a quasi-1D quantum conductor. In collaboration with the group of Xavier Waintal, we have refined this theory by taking into account the "real" electrostatic confinement potential. Without any adjustable parameters, we have been able to obtain a quantitative description of the propagation speed of the plasmon mode in our quantum conductor.

We also have observed how a simple constriction (QPC) in our waveguide can have a considerable impact on the plasmon velocity. In order to account for our observation we have presented two models for the role of the QPC. Comparing our experimental data with the simulations it seems that the QPC acts as a funnel for the plasmon. Within this picture, the calculated velocities for this situation are in very good agreement with our experimental results.

Finally, we have measured the time evolution of the plasmonic excitation when passing through the QPC constriction. We observe that the plasmon excitation initially slows down over a distance of 20 micrometres before accelerating to gain its initial velocity. This acceleration of the plasmon excitation is presently not completely understood and needs further investigation. Presently theoretical studies are underway in the group of Xavier Waintal to understand this puzzling time-dependent behaviour.

CHAPTER 5

Summary and Outlook

During this PhD work, I have investigated the propagation of an electronic excitation at the surface of the Fermi sea generated with ultrafast voltage pulses. This required to develop a new experimental set-up inspired by the approach of Kamata *et al.* [102] in order to measure the propagation speed of a single electron wave packet. Careful calibration of the measurement set-up as time-resolution down to the ps-regime were necessary. We found that the propagation velocity of an electron wave packet generated by applying an ultrafast voltage pulse to the ohmic contact of a two-dimensional electron system is much higher than the Fermi velocity. Thus, the local change in the density created with the application of an ultra-fast voltage pulse does not behave like a Landau-quasiparticle [117]. The origin of this high velocity comes from the fact that the voltage pulse creates a plasmonic excitation. In this case, the Coulomb interaction at the origin of this collective behaviour leads to a strong modification of the naive picture of non-interacting electrons. The measured velocity is indeed in very good agreement with the plasmon velocity for a gated two-dimensional electron gas calculated using the Boltzmann kinetic equation [119].

We have then shown that we can control the plasmon velocity by changing the number of channels of conductance available in the waveguide. This change is realized by varying the potential of the side gates used to define our quasi-1D conductor. We also observed that the electron wave packet propagates basically without any spreading over a distance of 70 micrometres, hence showing no dispersion. Our experimental results show a qualitative agreement with a theoretical approach based on the work of Matveev and Glazman [109] that allows to calculate the velocities of interacting electrons in a quasi-1D wire containing an arbitrary number of conducting channels. In order to obtain a quantitative description of our experiment we have initiated a collaboration with the group of Xavier Waintal. Using a realistic description of the experimental set-up, in particular, the exact electrostatic confinement potential, we have been able to obtain a quantitative description of our experimental results. Here it is important to underline that the theoretical description is based on a numerical calculation/simulation without any adjustable parameters.

In addition, we have seen that adding a constriction on our electron waveguide, in our case, a quantum point contact, can change the properties of the plasmon. When the QPC is set to transmit a single-channel of conductance, we observe a substantial reduction in the plasmon velocity. However, after a certain length, a re-acceleration of the plasmon is observed. This re-acceleration is most probably related to the repopulation of the single-particle states. The understanding of time evolution of such an electron wave packet when passing through a QPC constriction is presently an on-going project in the group of

Xavier Waintal by employing numerical simulations of time-resolved quantum electronics [81, 145].

We have also designed and fabricated an electronic interferometer in order to characterise the coherence length in this system. The interferometer consists of a tunnel coupled wire of tuneable length and could be used to inject to detect new interference effects when short voltage pulses are injected into it [64]. This detection requires, however, voltage pulses of very short temporal extension, such that this voltage pulse extension is much shorter than its propagation time. Due to the high plasmon velocity, this would need the creation of a voltage pulse within the picosecond range. There is an on-going project in our group which aims to address this problem by building an efficient optoelectronic converter. This device will allow us to transform on-chip a femtosecond laser pulse into a few picoseconds electronic excitation.

Finally, let us mention that the presented time control of single-electron pulses at the picosecond level will also be important for the implementation of waveguide architectures for flying qubits using single electrons. Integrating a leviton source into a waveguide interferometer would allow to realise single-electron flying-qubit architectures similar to those employed in linear quantum optics. Furthermore, our studies pave the way for studying real-time dynamics of a quantum nanoelectronic device such as the measurement of the time spreading or the charge fractionalisation dynamics of the electron wave packet during propagation.

APPENDIX A

Lock-in measurements

Most of the measurements presented in this manuscript were taken using a lock-in amplifier. Formally speaking, the lock-in detects the root mean square (RMS) voltage of an applied signal with respect to a given frequency. Considering a sinusoidal signal with root mean square equal to V_{RMS}, we obtain:

$$V(\theta) = \sqrt{2} V_{\mathrm{RMS}} \sin(\theta),$$

The lock-in multiplies this input signal with an internally generated sinusoidal voltage. The frequency of this internal signal is equal to the frequency of the signal applied to the lock-in reference input. For simplicity, let us consider that the signal of interest has the same frequency and phase as the internally generated signal. The operation that the lock-in does can be represented by the integral of the multiplication of these two signals over a period, divided by a period,

$$V = \frac{1}{2\pi} \int_0^{2\pi} \sqrt{2} V \sin(\theta) \cdot \beta \sin(\theta) d\theta, \tag{A.1}$$

where β is the amplitude of the internally generated signal. Calculating the integral, we find:

$$\beta = \sqrt{2} \tag{A.2}$$

To perform the lock-in measurements, we have used a square modulation on top of the Gaussian pulses, as exemplified in figure 3.9 in chapter 3. Let us define the square signal as:

$$f(\theta) = \begin{cases} A & \text{if } 0 \leq \theta \leq \pi \\ -A & \text{if } \pi < \theta \leq 2\pi \end{cases} \tag{A.3}$$

To calculate the measured voltage, we must perform the same integral as we have done in equation A.1. But first, let us calculate the RMS voltage for this square signal:

$$V_{\mathrm{RMS}}^{\mathrm{Square}} = \sqrt{\frac{1}{2\pi} \int_0^{2\pi} [f(\theta)]^2 d\theta} \tag{A.4}$$

$$V_{\mathrm{RMS}}^{\mathrm{Square}} = \sqrt{\frac{1}{2\pi}\left[\int_0^{\pi} A^2 d\theta + \int_{\pi}^{2\pi} (-A)^2 d\theta\right]} \tag{A.5}$$

$$V_{\mathrm{RMS}}^{\mathrm{Square}} = A \tag{A.6}$$

Let us calculate the measured voltage by the lock-in, using equation A.1 and the square voltage defined in equation A.3:

$$V_{\mathrm{measured}} = \frac{1}{2\pi}\int_0^{2\pi} f(\theta)\cdot\beta\sin(\theta)d\theta \tag{A.7}$$

$$\Longrightarrow \frac{1}{2\pi}\left[\int_0^{\pi} A\cdot\beta\sin(\theta)d\theta - \int_{\pi}^{2\pi} A\cdot\beta\sin(\theta)d\theta\right] \tag{A.8}$$

$$V_{\mathrm{measured}} = \frac{2\sqrt{2}A}{(\pi)} \tag{A.9}$$

Therefore, to find the correct RMS value using the voltage measured by the lock-in, we need to multiply the result of the measurements by the factor $\frac{\pi}{2\sqrt{2}}$.

APPENDIX B

Derivation of the transmission matrix for the tunnel-coupling wire

To derive the scattering matrix of the flying qubit in the presence of a tunnel-coupling barrier, we will first define the eigenstates at the entrance of the system (non-interaction region). We define the eigenstates of the electron propagating on the upper (lower) rail as $|0\rangle$ ($|1\rangle$) The schematic of the system is shown in figure B.1.

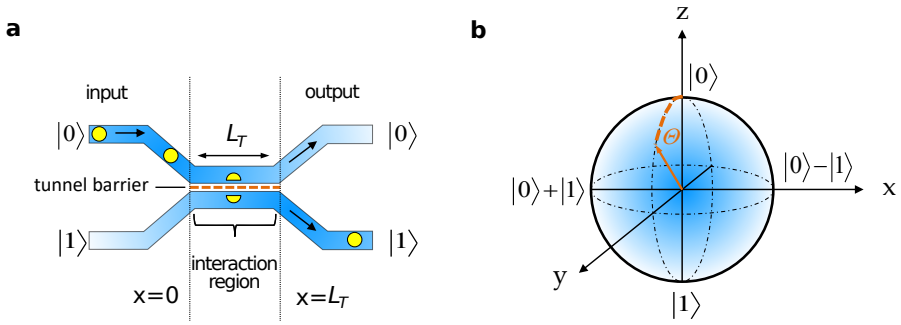

Figure B.1: Schematic of electron waveguides. a, Two electron waveguides used to define the two states of the flying qubit. The dashed orange line represents the tunnel barrier, used to couple the upper and lower electron waveguide. **b,** Bloch-sphere representation of the phase θ acquired by the qubit in the presence of the tunnel barrier. Figure adapted from [52].

Let us consider that the Hamiltonian of each electron waveguide outside the interacting region is H_0. We will consider that the electrons are in the ground state of H_0 with energy equal to:

$$\hat{\mathcal{H}}_0|0\rangle = \epsilon|0\rangle \tag{B.1}$$
$$\hat{\mathcal{H}}_0|1\rangle = \epsilon|1\rangle. \tag{B.2}$$

Then, let us consider that in the interaction region, the coupling is done by the operator $\hat{V}$, such that $\langle 0|\hat{V}|0\rangle = \langle 1|\hat{V}|1\rangle = 0$ and $\langle 1|\hat{V}|0\rangle = \langle 0|\hat{V}|1\rangle = t_c$. The Hamiltonian of the system considering the coupling is $\hat{\mathcal{H}} = \hat{\mathcal{H}}_0 + \hat{V}$. The new eigenstates for this Hamiltonian are:

$$|A\rangle = C_{A0}|0\rangle + C_{A1}|1\rangle \tag{B.3}$$
$$|S\rangle = C_{S0}|0\rangle + C_{S1}|1\rangle, \tag{B.4}$$

Normalising the eigenstates, we find $C_{X0}^2 + C_{X1}^2 = 1$, where $X = \{A,B\}$. We will refer to these new eigenstates as antisymmetric ($|A\rangle$) and symmetric states ($|S\rangle$). Let us calculate the energies of the new eigenstates:

$$\hat{\mathcal{H}}|A(S)\rangle = E_{A(S)}|A(S)\rangle \tag{B.5}$$
$$\implies (\hat{\mathcal{H}} - E_{A(S)})|A(S)\rangle = 0 \tag{B.6}$$
$$\implies \sum_{i=0,1} (\hat{\mathcal{H}} - E_{A(S)}) C_{A(S)i}|i\rangle = 0 \tag{B.7}$$

Multiplying the equation B.7 by $\langle j|$, where $j = 0, 1$, we find:

$$\implies \sum_{i,j=0,1} \left(\underbrace{\langle j|\hat{\mathcal{H}}|i\rangle}_{\hat{\mathcal{H}}_{j,i}} - E_{A(S)} \underbrace{\langle j|i\rangle}_{\delta_{i,j}} \right) C_{A(S)i} = 0 \tag{B.8}$$

To determine the non-trivial solution, we calculate the determinant of the matrix formed by equation B.8:

$$\det \begin{vmatrix} H_{00} - E_{A(S)} & H_{01} \\ H_{10} & H_{11} - E_{A(S)} \end{vmatrix} = 0 \tag{B.9}$$

Where the elements H_{ij} are equal to:

$$H_{00} = \langle 0|\hat{\mathcal{H}}_0 + \hat{V}|0\rangle = \epsilon \tag{B.10}$$
$$H_{11} = \langle 1|\hat{\mathcal{H}}_0 + \hat{V}|1\rangle = \epsilon \tag{B.11}$$
$$H_{10} = \langle 1|\hat{\mathcal{H}}_0 + \hat{V}|0\rangle = t_c \tag{B.12}$$
$$H_{01} = \langle 0|\hat{\mathcal{H}}_0 + \hat{V}|1\rangle = t_c \tag{B.13}$$

The determinant B.9 can be easily solved, and the solutions are:

$$E_A = \epsilon - t_c \tag{B.14}$$
$$E_S = \epsilon + t_c \tag{B.15}$$

By introducing this solution into equation B.7, we obtain the relationship between the constants C, where $C_{A0} = -C_{A1}$ and $C_{S0} = C_{S1}$. Normalising the eigenvectors, we find:

$$|A\rangle = \frac{1}{\sqrt{2}}\left(|0\rangle - |1\rangle\right) \tag{B.16}$$

$$|S\rangle = \frac{1}{\sqrt{2}}\left(|0\rangle + |1\rangle\right) \tag{B.17}$$

We rewrite the eigenstates of the non-interacting Hamiltonian as a function of the new eigenstates, by combining the equations B.16 and B.17:

$$|0\rangle = \frac{1}{\sqrt{2}}\left(|A\rangle + |S\rangle\right) \tag{B.18}$$

$$|1\rangle = \frac{1}{\sqrt{2}}\left(|S\rangle - |A\rangle\right) \tag{B.19}$$

As discussed in the main text, the wave function picks up a phase $e^{i\Theta_{A(S)}}$ inside the tunnelling region, considering the WKB approximation $\Theta_{A(S)} = \int_0^{L_T} dx k_{A(S)} \approx k_{A(S)} L_T$ [79] the wave function after the tunnelling region is equal to:

$$|A\rangle e^{i\Theta_{A(S)}} = |A\rangle e^{ik_A(S)L_T} \tag{B.20}$$

We can calculate the transmission matrix comparing the eigenstates before and after the interaction region:

$$S_T = \begin{pmatrix} S_{00} & S_{01} \\ S_{10} & S_{11} \end{pmatrix} = \begin{pmatrix} \langle 0|_{x=0}|0\rangle_{x=L_T} & \langle 0|_{x=0}|1\rangle_{x=L_T} \\ \langle 1|_{x=0}|0\rangle_{x=L_T} & \langle 1|_{x=0}|1\rangle_{x=L_T} \end{pmatrix} \tag{B.21}$$

We can easily calculate the elements of equation B.21, considering the equations B.18, B.19, B.20, finding:

$$\implies S_T = \exp\left(\frac{i(k_S + k_A)L_T}{2}\right) \begin{pmatrix} \cos\left(\frac{(k_S - k_A)L_T}{2}\right) & i\sin\left(\frac{(k_S - k_A)L_T}{2}\right) \\ i\sin\left(\frac{(k_S - k_A)L_T}{2}\right) & \cos\left(\frac{(k_S - k_A)L_T}{2}\right) \end{pmatrix} \tag{B.22}$$

APPENDIX C

Old cold finger

The cold finger used to perform the measurements presented in this manuscript is shown in figure C.1. We can see where the low-frequency DC lines (Thermocoax and constantan) are thermally attached, and how the cables arrive at the cold finger.

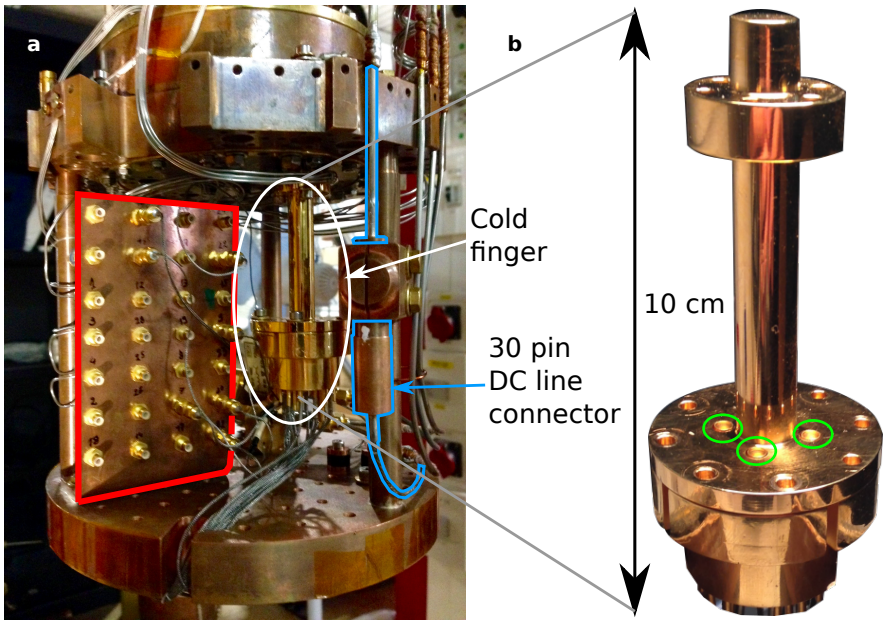

Figure C.1: Old cold finger. a, The cold finger is the gold piece, attached to the mixing chamber (MC). The red square shows where the thermocoax are thermally anchored. The blue line encircles the capillary and the thermal anchor for the constantan wires. These low-frequency wires arrive at the cold finger coming from the bottom. **b,** Photo of the cold finger. We highlight the holes used to connect the mini-SMP connectors with the green circles. Mini-SMP connectors are used to transmit the RF signals from the RF cables to the chip carrier. Figure adapted from [123].

APPENDIX D

Time-resolved sinusoidal signals

The figure D.1 shows time-resolved measurements of sinusoidal signals, generated using the pulse box. The data show that we can transmit up to the sample level all the harmonics of interest.

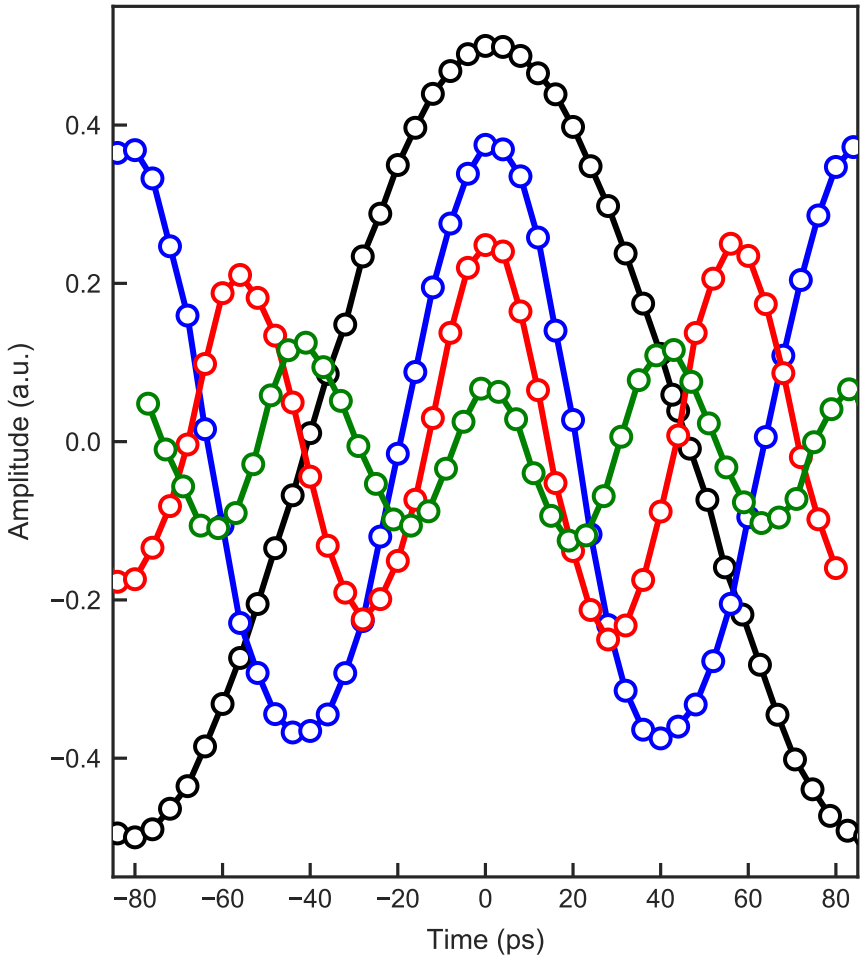

Figure D.1: Time-resolved measurements of sines. The black, blue, red and green circles correspond to the frequencies of 6, 12, 18 and 24 GHz, time-resolved at the sample level.

APPENDIX E

Fabry-Pérot model

The equation presented in section 4.4.1 comes from a simple model, where we consider that the QPC works as a simple beam-splitter with probabilities r and t to reflect or transmit the electron pulse propagating over the quasi-1D conductor. Considering that we apply a Gaussian pulse, the first pulse that is transmitted by two QPCs (in series) is proportional to,

$$A.e^{\frac{-1}{2}(\frac{t-\tau_0}{\sigma})^2} \times t_1 t_2, \tag{E.1}$$

where the first term is the Gaussian pulse centred around τ_0 and t_1 and t_2 are the transmissions probability of QPC_1 and QPC_2. Considering that part of the pulse is reflected at the second QPC, then reflected at the first QPC, and then transmitted by the second QPC, the second gaussian pulse transmitted by the two QPCs is equal to:

$$A.e^{\frac{-1}{2}(\frac{t-\tau_0-t_{separation}}{\sigma})^2} \times t_1 r_2 r_1 t_2. \tag{E.2}$$

Considering the case of a pulse that was reflected N times inside this "cavity" before traversing QPC_2, we have:

$$A.e^{\frac{-1}{2}(\frac{t-\tau_0-N\times t_{separation}}{\sigma})^2} \times t_1 (r_2 r_1)^N t_2. \tag{E.3}$$

Therefore, the general formula of the pulse traversing the sample is equal to:

$$f(t) = \sum_N A.e^{\frac{-1}{2}(\frac{t-\tau_0-N\times t_{separation}}{\sigma})^2} \times t_1 (r_2 r_1)^N t_2. \tag{E.4}$$

To reduce the number of variables, we normalized the first Gaussian pulse. Thus we get rid of the elements A, t_1 and t_2. Considering $R = r_2 \times r_1$, we arrive to the equation 4.12.

APPENDIX F

Fitting parameters of a electron cavity

In the table below, we list the parameters obtained from the fitting of the time-resolved trace transmitted through the electron cavity. These parameters were used in the plot of the figures 4.23 and 4.23. Using the equation 4.12, we have found the widths of the incoming pulse (σ), the position of the incoming pulse (τ_0), which we have initially set to zero, the time difference between the arrival time of the pulses at the sampling QPC ($t_{separation}$), and the reflection coefficient (R), which is proportional to the reflection coefficient at both QPCs. In table F.1, we show all the parameters, for the different side gate voltages and the different distances.

Table F.1: Parameters derived from the fit of the time-resolved trace of a wave packet within an electronic cavity.

Distance (µm)	V_{SG} (V)	τ_0 (ps)	Reflection (R)	$t_{separation}$ (ps)	FWHM (ps)
18.2	-0.8	-2.1	0.04	130.0	72.7
18.2	-1.0	0.5	0.03	135.6	72.4
18.2	-1.2	-3.5	0.02	138.5	64.9
18.2	-1.4	-3.9	0.05	139.3	66.1
18.2	-1.6	-3.7	0.25	135.1	86.7
32.4	-0.8	0.8	0.16	113.0	82.9
32.4	-1.0	-4.1	0.13	124.4	88.6
32.4	-1.2	-6.6	0.06	125.3	76.3
32.4	-1.4	-1.7	0.12	134.0	81.9
32.4	-1.6	-3.3	0.19	127.9	83.5
50.6	-0.8	2.7	0.23	114.4	87.1
50.6	-1.0	-1.1	0.23	122.8	90.2
50.6	-1.2	0.5	0.11	124.1	80.0
50.6	-1.4	-1.2	0.13	129.7	81.9
50.6	-1.6	2.9	0.25	127.9	94.0
79.6	-0.8	-3.9	0.85	118.0	115.8
79.6	-1.0	0.4	0.65	120.1	107.0
79.6	-1.2	2.6	0.44	118.3	89.9
79.6	-1.4	1.2	0.43	118.5	90.0
79.6	-1.6	-1.4	0.71	125.0	118.0
111.6	-0.8	-1.6	0.78	122.0	117.8
111.6	-1.0	0.0	0.57	124.6	100.7
111.6	-1.2	-1.0	0.39	122.9	84.9
111.6	-1.4	2.7	0.30	119.6	76.1
111.6	-1.6	0.4	0.56	121.1	101.9
129.8	-0.8	-3.1	0.67	122.6	105.5
129.8	-1.0	-2.1	0.59	124.0	97.8
129.8	-1.2	1.8	0.52	124.4	93.1
129.8	-1.4	5.2	0.48	122.4	90.7
129.8	-1.6	2.7	0.62	118.1	105.6

APPENDIX G

Using the QPC to create short pulses

In the last section of chapter 3, we investigate how to create ultra-short pulses using QPCs. One possibility is to apply a fast voltage pulse to a QPC which is capacitively coupled to the 2DEG.

This method is an alternative way to induce excitations in the 2DEG, instead of injecting charges via an ohmic contact. We can find a significant number of studies that employed this method to induce electron excitation into the 2DEG [111, 144, 147]. Usually, the shape of the induced wave packet is proportional to the derivative of the applied voltage when this method is applied to induce excitation onto edge channels [111, 144, 147]. This of course depends on the frequency of the applied voltage pulse and the RC time of the system. We have shown that for a fixed voltage pulse (Gaussian with FWHM $\approx 80\,\mathrm{ps}$), we can change the shape of the induced pulse, just by playing with the electron density underneath the gate. We can control the electron density by varying the DC voltage of the gate. Let us focus on two extreme situations: (i) the induced pulse is proportional to the derivative of the initial voltage pulse. (ii) the induced pulse has the same shape as the applied voltage pulse.

The measurements protocol will be the following: we create the electron excitation in the quasi-1D conductor by applying an ultra-short voltage pulse to one QPC. Then, we use another QPC to time-resolve the induced excitation. Setting the DC voltage of the QPC used to induce the voltage pulse close to the pinch-off regime drastically changes the shape of the resolved excitation. We present the time-resolved measurements for this situation in figure G.1 for different confinement potential (V_{SG}).

Let us discuss the time-resolved traces shown in figure G.1. The time-of-flight does not change by varying the confinement (V_{SG}). The only change is an increase in the widths, for more negative V_{SG}. The excitation is induced at QPC_1, and is time-resolved at QPC_3. The distance between these two QPCs is $55\,\mu\mathrm{m}$. It is worth mentioning that the amplitudes of the resolved excitation are very small since the region where we apply the excitation is almost fully depleted.

We have tried to evaluate the velocity of this induced excitation. However, it is a bit more complicated than the case in which we injected the excitation using the ohmic contact. When we try to perform *in-situ* calibration, that is, to measure the time-of-flight of the 2D plasmon created by applying a voltage pulse to the QPC, we have measured a wave packet with similar time-of-flight (TOF) as the induced excitation propagating on the quasi-1D conductor.

We can estimate the TOF of the induced excitation considering the calibration for the 2D

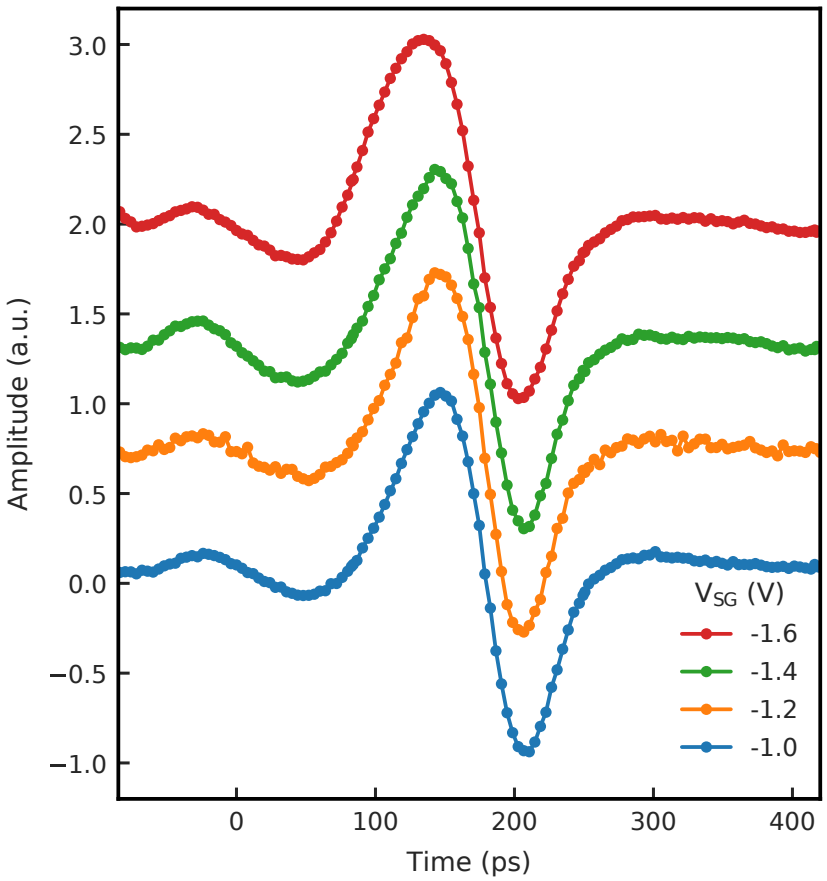

Figure G.1: Excitation induced via capacitive coupling (i). The curves are normalized and have been offset for clarity. The excitation is created at QPC_1 and time-resolved at QPC_3.

plasmon obtained by injecting the voltage pulse through the ohmic contact. To determine the arrival times in each QPC, we have taken the average time position between the peak and the dip presented in figure G.1. This average time is plotted in figure G.2. We plot the arrival time for different length and, as well, for different confinements V_{SG}. For the shortest distance, 15 µm, we have plotted the TOF only for small confinement voltages (up to $V_{SG} = -1.2\,V$), because the shape of the pulse gets very distorted for very negative confinement.

We have also plotted the estimated velocities in figure G.2. The average velocities were calculated by doing a linear fit of the time-of-flight in G.2**a**, in the same manner that we have done in chapter 4. The estimated velocities lie between the velocity of a plasmon formed in a single-channel (red line) and the Fermi velocity (black line). One could think that we are inducing a neutral excitation, which should propagate with the Fermi velocity.

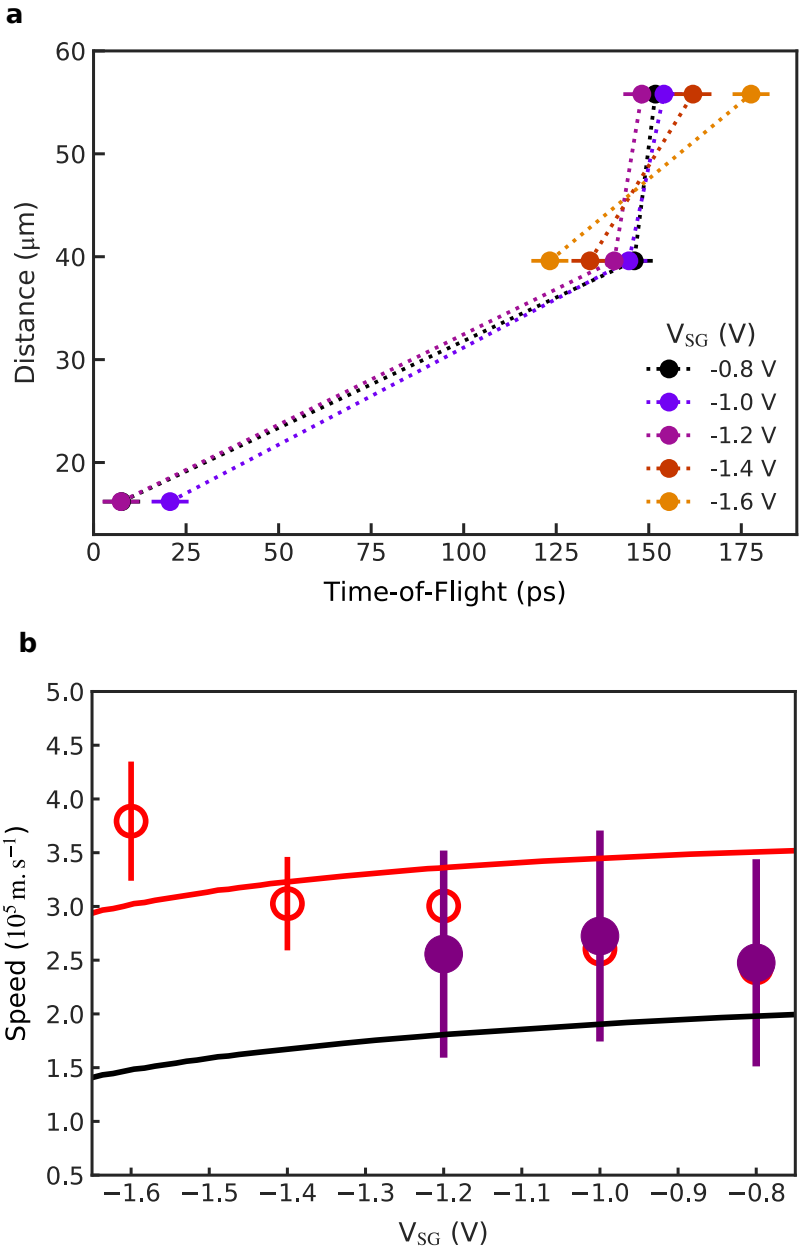

Figure G.2: Time-of-flight and velocity of induced excitation (i). **a,** Time-of-flight for different confinements V_{SG} and different distances. **b,** Velocity as a function of the confinement. The purple circles are the velocity using the QPC as a pump, calculated from **a**. The red circles correspond to the case in which we use the QPC as a barrier, fixed at the first plateau of conductance. The red curve corresponds to the self-consistent simulations for the plasmon funnelled into a single channel. The black line corresponds to the Fermi velocity, derived from the self-consistent simulations.

Let us now discuss a slightly different experiment. Once more, we are inducing the excitation using QPC, and not with the ohmic contact. However, this time, we do not apply a DC voltage to the QPC. By using this approach, what we obtain is a wave packet with the same shape as when we create the excitation using the ohmic contact.

However, as we increase the voltage that defines the confinement V_{SG}, the resolved pulse becomes deformed. The pulse has a similar shape as the case when we deplete the QPC with a DC voltage, as shown in figure G.3. The charge density close to the QPC is also affected when we increase the confinement at the quasi-1D conductor. At some point, we end up with a similar capacitance between the QPC and the quasi-1D conductor, to the case when we have just polarised the QPC. Also, when we increase the confinement, the resistance of the quasi-1D conductor increases, which also plays a role to change the RC constant of the differentiator.

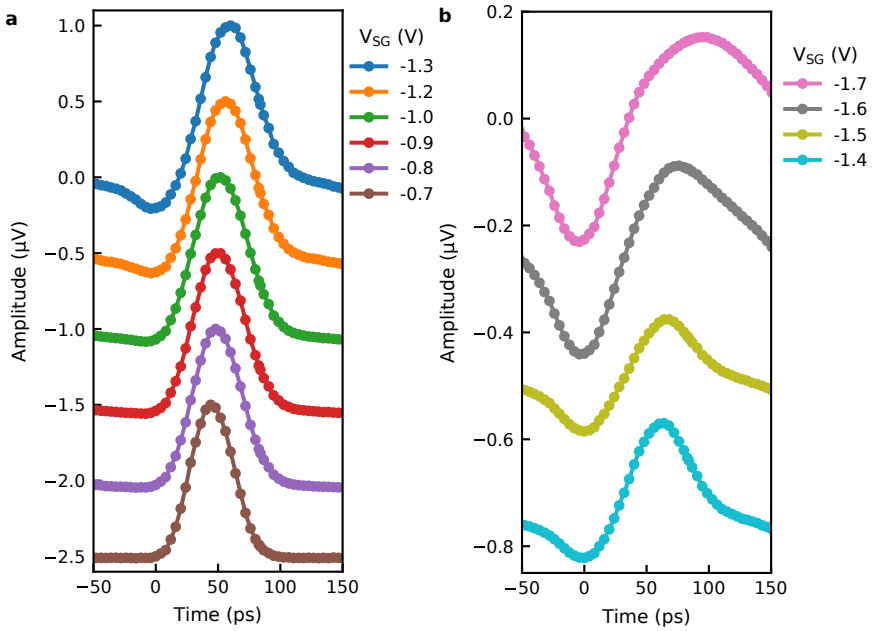

Figure G.3: Excitation induced via capacitive coupling (ii). a, The position of the peak appears at later times, as the confinement is increased (more negative V_{SG}). However, the pulse becomes deformed. **b,** Time-resolved traces for more negative confinements than in **a**. The pulses are offset for clarity. The excitation is induced at QPC_1 and resolved at QPC_3.

Once more, the *in-situ* calibration , that is, the time-of-flight measurements of the 2D plasmon created by applying a voltage pulse to the QPC, gives a time-resolved trace similar to the case when the QPC is polarised with a DC voltage that it is close to the pinch-off regime. For this situation, the resolved wave packet is similar to the data shown in figure G.3**b** when $V_{SG} = -1.5\,V$. To estimate the time-of-flight, we have used the time-of-flight of the 2D plasmon, measured when we inject the excitation via the ohmic contact. The estimated time-of-flights are shown in figure G.4, together with the calculated velocities.

To calculate the average velocity, we have traced a linear fit in the data of the distance versus time-of-flight in figure G.4 **a**. The slope of the fit corresponds to the velocity, as

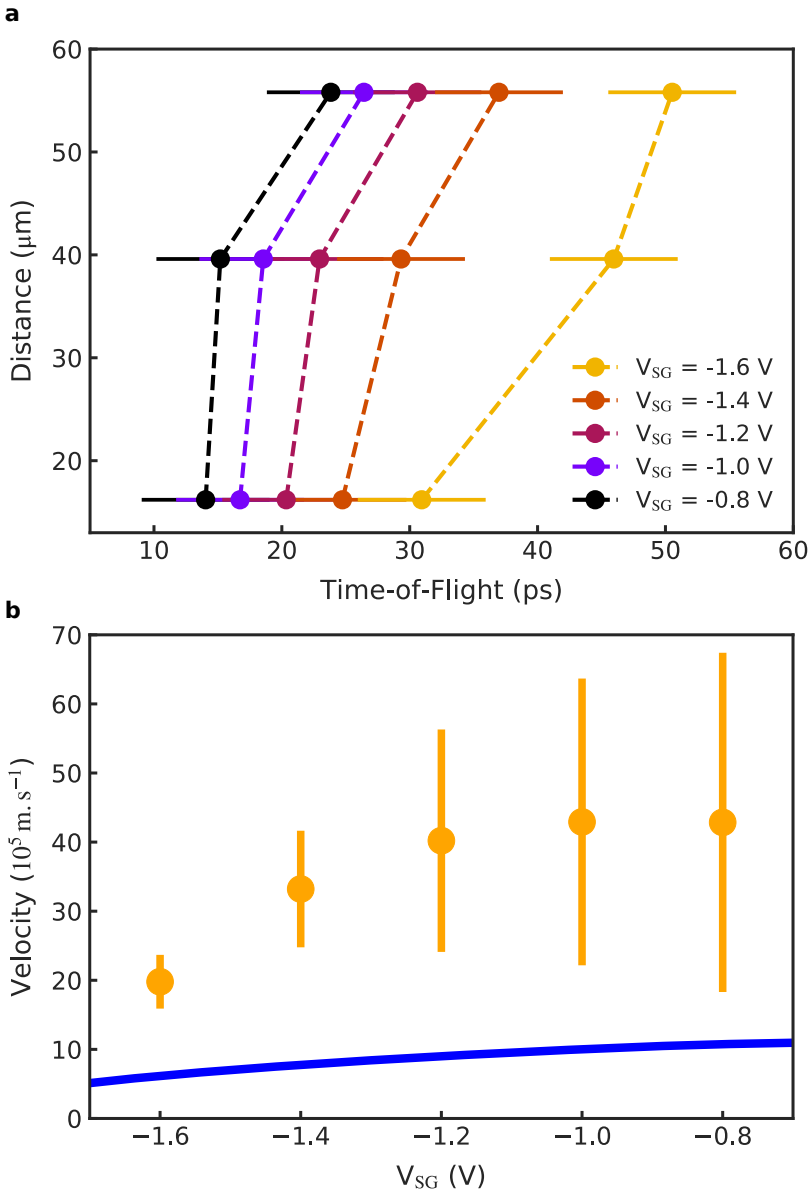

Figure G.4: Time-of-flight and velocity of induced excitation (ii). a, Time-of-flight for different confinements V_{SG} **b,** Velocity as a function of the confinement. The orange circles are the velocity using the QPC as a pump, calculated from **a**. The blue line is the plasmon velocity derived from the self-consistent simulations.

we have discussed in chapter 4. The estimated velocities vary between $20 \times 10^5\,\mathrm{m\,s^{-1}}$ and $40 \times 10^5\,\mathrm{m\,s^{-1}}$. The physical mechanism responsible for such high velocities is not clear at the moment.

We have also performed a different experiment, to see how the wave packet is affected with a local barrier. We have measured the time-resolved electron wave packet at QPC_3 when generating the pulse at QPC_1, polarising also QPC_2 to act as a QPC barrier. Like this, we can locally change the number of channels of conductance, exemplified in figure 4.11. The result is shown in figure G.5.

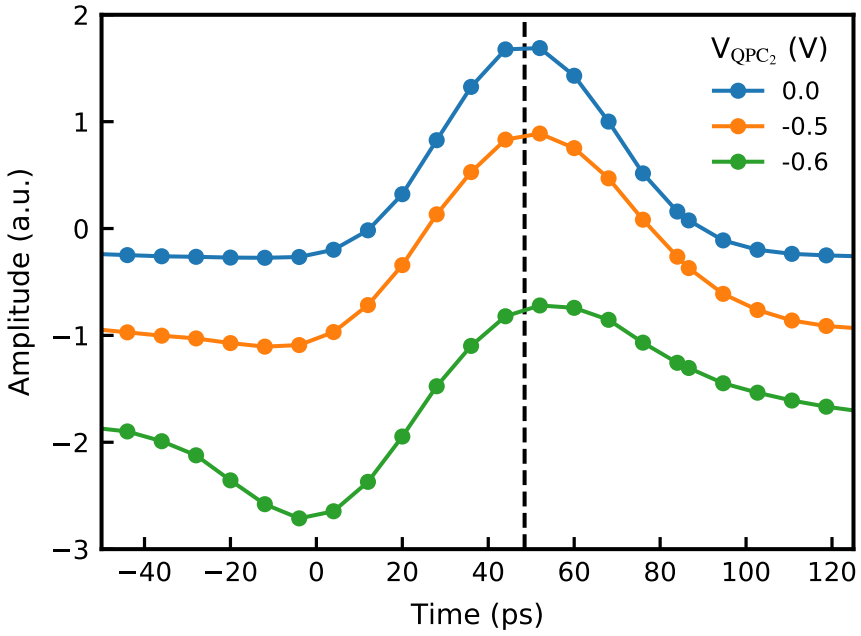

Figure G.5: Pulsing in QPC_1 and probing with QPC_3 having QPC_2 as a QPC barrier. Time-resolved trace of the excitation created at QPC_1 and measured at QPC_3. The wave packet gets deformed by polarising QPC_2. The curves were normalised and shifted for a better understanding. The dashed line corresponds to the peak position when QPC_2 is not polarised.

After polarising QPC_2, we observe a distortion at the pulse shape. The pulse presents the same behaviour as the time-resolved measurement when we apply the AC pulse to QPC_1 using a strong DC voltage, or when we squeeze the entire quasi-1D conductor with V_{SG}. The effect on our system is that by polarising QPC_2 we are increasing the resistance of the conductor. Therefore, we are changing the RC constant of the system, resulting in similar pulse shapes as when we have changed the capacitance underneath the pulsing QPC.

APPENDIX H

Impedance mismatch

In section 3.4.3, we have discussed the use of attenuators to mitigate injection of thermal noise and to limit the power that is sent into the dilution refrigerator. It is important to use large bandwidths attenuators to avoid the deformation of the transmitted signals. In our set-up, we have installed attenuators[1] which work from DC to 40 GHz.

Let us discuss the voltage drop in the attenuators and check its dependence with the connected impedance. For this purpose, we will consider the circuit of an attenuator. Figure H.1**a** shows a simplified schematic of an attenuator, which is known as the T-section due to its internal arrange of resistances. V_I and V_0 correspond to the input and output voltage at the attenuator. The resistances R_1 and R_2 are chosen in order to deliver the desired voltage drop. Moreover, in commercial attenuators, these values are typically designed to give an input and output impedance of 50 Ω. This value is selected to match the internal impedance of most RF instruments, which is also 50 Ω. We present a generic case of the use of an attenuator in figure H.1**b**, where on the left side there is a signal generator with an internal impedance Z_I. On the right side, the attenuator is connected to the impedance Z_0.

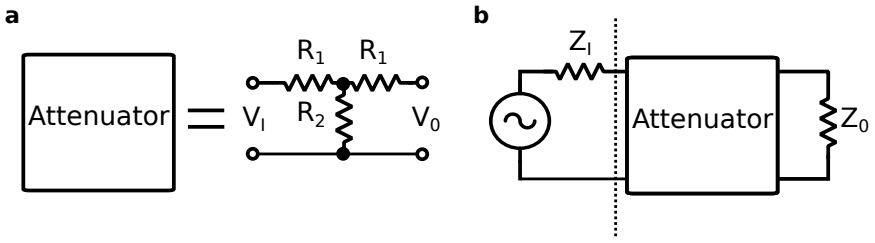

Figure H.1: Schematic of an T-section attenuator a, Schematic of an attenuator, this is known as the T-section attenuator. V_I and V_0 correspond to the input and output voltage at the attenuator. **b,** Circuit considering a signal generator with its internal impedance of 50 Ω (Z_I) connected to an attenuator. Then, the attenuator is connected to an output load Z_0.

In order to calculate the voltage reduction at attenuator, let us consider the circuit depicted in figure H.1. The resistor R_2 is in parallel with the of impedances $R_1 + Z_0$, and

1 XMA-4882-6040

we will define R_{eq1} this parallel resistance. Thus, R_{eq1} is equal to:

$$R_{eq1} = \frac{R_2 \times (R_1 + Z_0)}{R_2 + (R_1 + Z_0)}. \tag{H.1}$$

and the total impedance of the circuit, also taken into account the internal impedance of the generator is equal:

$$R_{eqtotal} = Z_I + R_1 + R_{eq1}. \tag{H.2}$$

To calculate the input voltage at the attenuator V_I, we use the voltage divider formula, which gives:

$$V_I = V_s . \frac{R_{eq1} + R_1}{R_{eqtotal}}, \tag{H.3}$$

where V_s is the generated voltage. Similarly, we find the voltage drop over the parallel resistance R_{eq1},

$$V_{Req1} = V_I . \frac{R_{eq1}}{R_1 + R_{eq1}}, \tag{H.4}$$

and in the same manner we determine the output voltage V_0:

$$V_0 = V_{Req1} \times \frac{Z_0}{R_1 + Z_0}. \tag{H.5}$$

The attenuation is determined as the ratio between the the ouput and input voltage, in this way:

$$\text{Attenuation} = 20. \log(\frac{V_0}{V_I}) \tag{H.6}$$

Now that we have defined the set of equations to calculate the attenuation let us take an example. Considering the impedances Z_I and Z_0 equal to 50 Ω, and using the values $R_1 = 40.91\,\Omega$ and $R_2 = 10.10\,\Omega$. Injecting these values to the set of equations H.1-H.6, one easily finds that the attenuation is of -20 dB, since we have taken the resistances R_1 and R_2 values expected for this attenuation. However, assuming a different output impedance Z_0, the effective attenuation changes. Z_0 is not 50 Ω in our sample, for example, the resistance of the ohmic contact at the injection side is approximately 1 kΩ. Putting this value in the set of equations H.1-H.6 one finds an attenuation of -14.5 dB.

To simulate the measured signal numerically in section 3.5, we have done the same calculation considering two attenuators in series, and assuming the resistance from the QPC to ground as 50 MΩ and values of R_1 and R_2 corresponding to the attenuation of 10 dB and 6 dB. We repeat this calculation for the ohmic contact, considering the resistance of 1 kΩ, and the values expected to obtain an attenuation of 20 dB that we have installed in our RF lines. Thus, we have demonstrated how the voltage drop in the attenuator changes, depending on the impedance load connected to its output.

APPENDIX I

Transmission of the DC lines

To characterise the transmission of filtered DC lines in our dilution refrigerator, we have used the vector network analyser R&S®ZVL6. This equipment has an internal impedance of 50 Ω. In figure I.1, we show the schematic of the equivalent circuit used. The voltage measured on the resistor R_2 can be calculated via the equivalent impedance of the resistor R_2 with the capacitor C_1 and then consider the voltage divider formed with R_1. Therefore, the expected transmission is equal to:

$$S_{21} = 20.\log_{10}\left(\frac{R_2}{\sqrt{(R_1+R_2)^2+(\omega.C_1.R_1.R_2)^2}}\right), \tag{I.1}$$

where $\omega = 2.\pi f$, and for our system R_1 is on the order of 1350 Ω.

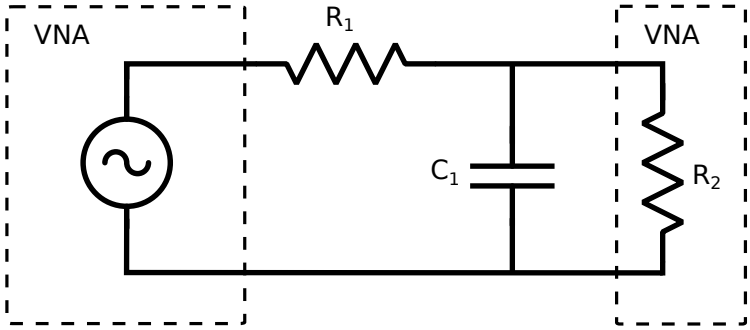

Figure I.1: Electronic circuit using VNA. The VNA is represented by the dashed retangles, where on the left there is the internal signal generator and on the right R_2 correspond to the 50 Ω impedance to ground. R_1 represents the impedance of the Constantan wire together with the resistor of the RC filter. C_1 is the capacitor connected to ground.

APPENDIX J

Transmission of the RF lines

The transmission of the RF lines was measured with the VNA Agilent technologies E8362C, which has a bandwidth of 20 GHz. We can measure the transmission of the lines at low temperatures, interconnecting two of these lines at the coldest part of the fridge. We show in figure J.1, the transmission S_{21}. To be able to predict the attenuation for each frequency inside this range, and also to extrapolate the transmission to higher frequencies, we have fitted these data with the equation J.1,

$$\frac{A}{1+\left(\frac{\nu}{B}\right)^{C}}, \tag{J.1}$$

where A, B and C are parameters which we extract from the fit and ν corresponds to the frequency applied.

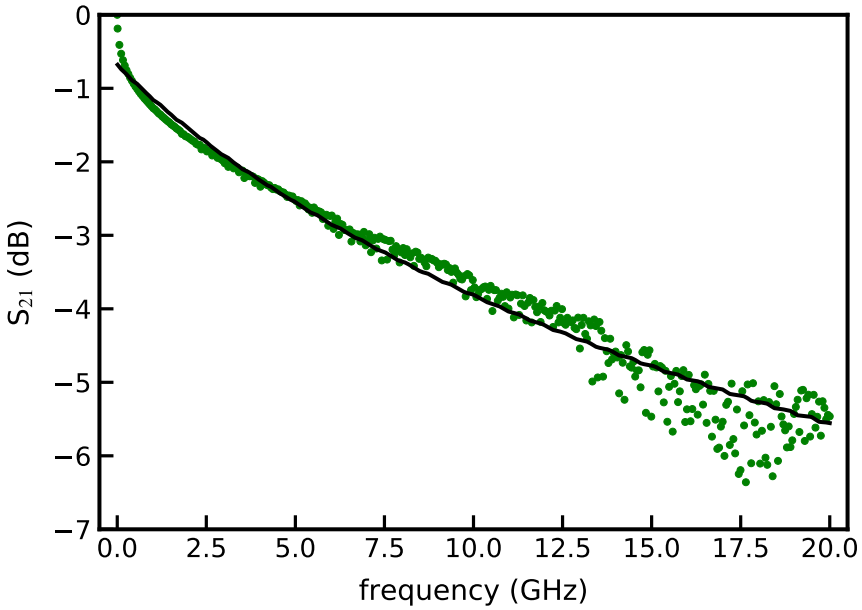

Figure J.1: Transmission of the RF lines at low-temperatures. The green dots correspond to the transmission of the RF lines measured with the lowest reachable temperature of 20 mK. The black line corresponds to the fit using equation J.1.

Bibliography

1. Weisstein, Eric W.: *Kelvin, Lord William Thomson (1824-1907)*. URL: http://scienceworld.wolfram.com/biography/Kelvin.html (visited on 10/19/2019) (cit. on p. 1).
2. GRAS, Philippe: *Santos-Dumont, le Brésilien volant*. URL: https://www.histoire-image.org/fr/etudes/santos-dumont-bresilien-volant (visited on 10/19/2019) (cit. on p. 1).
3. Contributors, Wikipedia: *Clément Ader*. URL: https://fr.wikipedia.org/wiki/Clement_Ader (visited on 10/19/2019) (cit. on p. 1).
4. Lightman, Alan: *The discoveries: Great Breakthroughs in 20th-Century Science*. Toronto, 2005 (cit. on p. 1).
5. Eisberg, Robert, Robert Resnick, and Judith Brown: *Quantum Physics of Atoms, Molecules, Solids, Nuclei, and Particles*. Vol. 2. New York, NY, Mar. 1985: p. 713 (cit. on p. 1).
6. Dirac, P. A. M.: 'The Quantum Theory of the Emission and Absorption of Radiation'. *Proceedings of the Royal Society A: Mathematical, Physical and Engineering Sciences* (1927), vol. 114(767): pp. 243–265 (cit. on p. 1).
7. Glauber, Roy J.: *Quantum Theory of Optical Coherence*. 2007: p. 656 (cit. on p. 1).
8. HANBURY BROWN, R. and R. Q. TWISS: 'A Test of a New Type of Stellar Interferometer on Sirius'. *Nature* (Nov. 1956), vol. 178(4541): pp. 1046–1048. URL: https://www.nature.com/articles/1781046a0 (cit. on p. 2).
9. Kimble, H. J., M. Dagenais, and L. Mandel: 'Photon antibunching in resonance fluorescence'. *Physical Review Letters* (1977), vol. 39(11): pp. 691–695 (cit. on p. 2).
10. Einstein, A., B. Podolsky, and N. Rosen: 'Can Quantum-Mechanical Description of Physical Reality Be Considered Complete?' *Physical Review* (May 1935), vol. 47(10): pp. 777–780. URL: https://journals.aps.org/pr/abstract/10.1103/PhysRev.47.777 (cit. on p. 2).
11. Bell, J. S.: 'On the Einstein Podolsky Rosen paradox'. *Physics Physique Fizika* (Nov. 1964), vol. 1(3): pp. 195–200. URL: https://link.aps.org/doi/10.1103/PhysicsPhysiqueFizika.1.195 (cit. on p. 2).

12. Aspect, Alain, Philippe Grangier, and Gérard Roger: 'Experimental Realization of Einstein-Podolsky-Rosen-Bohm Gedankenexperiment : A New Violation of Bell's Inequalities'. *Physical Review Letters* (July 1982), vol. 49(2): pp. 91–94. URL: https://link.aps.org/doi/10.1103/PhysRevLett.49.91 (cit. on p. 2).

13. Fox, Mark: 'Quantum Optics: An Introduction'. *Springer Handbook of Lasers and Optics* (2012), vol.: p. 400 (cit. on p. 2).

14. Solomon, P.M. and Hadis Morkoc: 'Modulation-doped GaAs/AlGaAs heterojunction field-effect transistors (MODFET's), ultrahigh-speed device for supercomputers'. *IEEE Transactions on Electron Devices* (Aug. 1984), vol. 31(8): pp. 1015–1027. URL: http://ieeexplore.ieee.org/document/1483939/ (cit. on p. 3).

15. Davies, John H, Ivan A Larkin, and E. V. Sukhorukov: 'Modeling the patterned electron gas: Electrostatics'. *Journal of Applied Physics* (1995), vol. 77(9): pp. 4504–4512 (cit. on p. 3).

16. Gabelli, Julien: 'Evidence of quantum coherence in dynamical electronic transport'. PhD thesis. Université Pierre et Marie Curie - Paris VI, 2006. URL: https://tel.archives-ouvertes.fr/tel-00011619 (cit. on p. 3).

17. Marguerite, Arthur: 'Two-particle interferometry for quantum signal processing'. PhD thesis. Université Pierre et Marie Curie - Paris VI, 2017. URL: http://www.theses.fr/2017PA066124 (cit. on p. 3).

18. Datta, Supriyo: *Electronic transport in mesoscopic systems*. 1999 (cit. on pp. 4, 6, 79).

19. Roulleau, Preden, F Portier, P Roche, A Cavanna, G Faini, U Gennser, and D Mailly: 'Direct measurement of the coherence length of edge states in the integer quantum hall regime'. *Physical Review Letters* (2008), vol. 100(12): pp. 6–9 (cit. on pp. 4, 6, 7).

20. Niimi, Y., Y. Baines, T. Capron, D. Mailly, F. Y. Lo, A. D. Wieck, T. Meunier, L. Saminadayar, and C. Bäuerle: 'Effect of disorder on the quantum coherence in mesoscopic wires'. *Physical Review Letters* (2009), vol. 102(22): pp. 1–4 (cit. on pp. 4, 6).

21. Niimi, Yasuhiro, Yannick Baines, Thibaut Capron, Dominique Mailly, Fang Yuh Lo, Andreas D. Wieck, Tristan Meunier, Laurent Saminadayar, and Christopher Bäuerle: 'Quantum coherence at low temperatures in mesoscopic systems: Effect of disorder'. *Physical Review B - Condensed Matter and Materials Physics* (2010), vol. 81(24) (cit. on pp. 4, 6).

22. Duprez, H, E Sivre, A Anthore, A Aassime, A Cavanna, A Ouerghi, U Gennser, and F Pierre: 'Macroscopic Electron Quantum Coherence in a Solid-State Circuit'. *Physical Review X* (May 2019), vol. 9(2): p. 21030. URL: https://journals.aps.org/prx/abstract/10.1103/PhysRevX.9.021030 (cit. on pp. 4, 6).

23. Störmer, H.L., R. Dingle, A.C. Gossard, W. Wiegmann, and M.D. Sturge: 'Two-dimensional electron gas at a semiconductor-semiconductor interface'. *Solid State Communications* (Mar. 1979), vol. 29(10): pp. 705–709. URL: https://linkinghub.elsevier.com/retrieve/pii/003810987991010X (cit. on p. 4).

24. Van Wees, B. J., H. Van Houten, C. W J Beenakker, J. G. Williamson, L. P. Kouwenhoven, D. Van Der Marel, and C. T. Foxon: 'Quantized conductance of point contacts in a two-dimensional electron gas'. *Physical Review Letters* (1988), vol. 60(9): pp. 848–850 (cit. on pp. 4, 5).

25. Wharam, D A, T J Thornton, R Newbury, M Pepper, H Ahmed, J E F Frost, D G Hasko, D C Peacock, D A Ritchie, and G A C Jones: 'One-dimensional transport and the quantisation of the ballistic resistance'. *Journal of Physics C: Solid State Physics* (2002), vol. 21(8): pp. L209–L214 (cit. on pp. 4, 5).

26. Clarke, W. R., M. Y. Simmons, and C. T. Liang: *Ballistic Transport in 1D GaAs/AlGaAs Heterostructures*. Vol. 1-6. September 2015. Elsevier Ltd., 2011: pp. 279–325. URL: http://dx.doi.org/10.1016/B978-0-12-803581-8.09401-7 (cit. on p. 4).

27. Büttiker, M, Y Imry, R Landauer, and S Pinhas: 'Generalized many-channel conductance formula with application to small rings'. *Physical Review B* (May 1985), vol. 31(10): pp. 6207–6215. URL: https://link.aps.org/doi/10.1103/PhysRevB.31.6207 (cit. on p. 4).

28. Schuster, R, E Buks, M Heiblum, D Mahalu, V Umansky, and Hadas Shtrikman: 'Phase measurement in a quantum dot via a double-slit interference experiment'. *Nature* (1997), vol. 385(6615): pp. 417–420 (cit. on p. 5).

29. Ji, Yang, Yunchul Chung, D Sprinzak, M Heiblum, D Mahalu, and Hadas Shtrikman: 'An electronic Mach-Zehnder interferometer'. *Nature* (Mar. 2003), vol. 422(6930): pp. 415–418. URL: http://www.nature.com/articles/nature01503 (cit. on pp. 5–7).

30. Yamamoto, Michihisa, Shintaro Takada, Christopher Bäuerle, Kenta Watanabe, Andreas D Wieck, and Seigo Tarucha: 'Electrical control of a solid-state flying qubit'. *Nature Nanotechnology* (2012), vol. 7(4): pp. 247–251. URL: https://www.nature.com/articles/nnano.2012.28 (cit. on pp. 5, 19, 20).

31. Bocquillon, E, V Freulon, J.- M Berroir, P Degiovanni, B Placais, A Cavanna, Y Jin, and G Feve: 'Coherence and Indistinguishability of Single Electrons Emitted by Independent Sources'. *Science* (Mar. 2013), vol. 339(6123): pp. 1054–1057. URL: http://www.sciencemag.org/cgi/doi/10.1126/science.1232572 (cit. on pp. 5, 10, 16, 27).

32. Klitzing, K. v., G. Dorda, and M. Pepper: 'New Method for High-Accuracy Determination of the Fine-Structure Constant Based on Quantized Hall Resistance'. *Physical Review Letters* (Aug. 1980), vol. 45(6): pp. 494–497. URL: https://link.aps.org/doi/10.1103/PhysRevLett.45.494 (cit. on p. 5).

33. Tsui, D. C., H. L. Stormer, and A. C. Gossard: 'Two-dimensional magneto-transport in the extreme quantum limit'. *Physical Review Letters* (1982), vol. 48(22): pp. 1559–1562 (cit. on p. 6).

34. Goerbig, M. O.: 'Quantum Hall Effects'. *AIP Conference Proceedings* (Sept. 2009), vol. 1482: pp. 335–339. URL: http://arxiv.org/abs/0909.1998 (cit. on p. 6).

35. Büttiker, M.: 'Absence of backscattering in the quantum Hall effect in multiprobe conductors'. *Physical Review B* (1988), vol. 38(14): pp. 9375–9389 (cit. on p. 6).

36. Armagnat, Pacôme: 'Physique quantique et éléctrostatique auto-cohérentes'. PhD thesis. Université Grenoble Alpes, 2019 (cit. on pp. 8, 32, 38, 39, 85).

37. Geerligs, L. J., V. F. Anderegg, P. A.M. Holweg, J. E. Mooij, H. Pothier, D. Esteve, C. Urbina, and M. H. Devoret: 'Frequency-locked turnstile device for single electrons'. *Physical Review Letters* (1990), vol. 64(22): pp. 2691–2694 (cit. on p. 8).

38. Pekola, Jukka P, Olli-Pentti Saira, Ville F Maisi, Antti Kemppinen, Mikko Möttönen, Yuri A Pashkin, and Dmitri V Averin: 'Single-electron current sources: Toward a refined definition of the ampere'. *Reviews of Modern Physics* (Oct. 2013), vol. 85(4): pp. 1421–1472. URL: https://link.aps.org/doi/10.1103/RevModPhys.85.1421 (cit. on p. 9).

39. Bureau International des Poids et Mesures: *The International System of Units (SI Units)*. STEDI Media, Paris, 2006. URL: http://stacks.iop.org/0508-3443/15/i=10/a=312?key=crossref.39ceefe323c2db4a891242baef0b1f08 (cit. on p. 9).

40. Blumenthal, M. D., B. Kaestner, L. Li, S. Giblin, T. J.B.M. Janssen, M. Pepper, D. Anderson, G. Jones, and D. A. Ritchie: 'Gigahertz quantized charge pumping'. *Nature Physics* (2007), vol. 3(5): pp. 343–347 (cit. on p. 9).

41. Giblin, S. P., M. Kataoka, J. D. Fletcher, P. See, T. J.B.M. Janssen, J. P. Griffiths, G. A.C. Jones, I. Farrer, and D. A. Ritchie: 'Towards a quantum representation of the ampere using single electron pumps'. *Nature Communications* (2012), vol. 3(May): pp. 930–936. URL: http://dx.doi.org/10.1038/ncomms1935 (cit. on pp. 9, 10).

42. Fletcher, J. D., M. Kataoka, S. P. Giblin, Sunghun Park, H. S. Sim, P. See, D. A. Ritchie, J. P. Griffiths, G. A.C. Jones, H. E. Beere, and T. J.B.M. Janssen: 'Stabilization of single-electron pumps by high magnetic fields'. *Physical Review B - Condensed Matter and Materials Physics* (2012), vol. 86(15): pp. 1–6 (cit. on p. 9).

43. Fletcher, J D, P See, H Howe, M Pepper, S P Giblin, J P Griffiths, G A C Jones, I Farrer, D A Ritchie, T J B M Janssen, and M Kataoka: 'Clock-controlled emission of single-electron wave packets in a solid-state circuit'. *Physical Review Letters* (2013), vol. 111(21): pp. 1–5 (cit. on pp. 9, 10, 15).

44. Yamahata, Gento, Stephen P. Giblin, Masaya Kataoka, Takeshi Karasawa, and Akira Fujiwara: 'High-accuracy current generation in the nanoampere regime from a silicon single-trap electron pump'. *Scientific Reports* (2017), vol. 7(March): pp. 3–10 (cit. on p. 10).

45. Rossi, Alessandro, Jevgeny Klochan, Janis Timoshenko, Fay E. Hudson, Mikko Möttönen, Sven Rogge, Andrew S. Dzurak, Vyacheslavs Kashcheyevs, and Giuseppe C. Tettamanzi: 'Gigahertz Single-Electron Pumping Mediated by Parasitic States'. *Nano Letters* (2018), vol. 18(7): pp. 4141–4147 (cit. on p. 10).

46. Ota, Tomoaki, Shunya Akiyama, Masayuki Hashisaka, Koji Muraki, and Toshimasa Fujisawa: 'Spectroscopic study on hot-electron transport in a quantum Hall edge channel'. *Physical Review B* (2019), vol. 99(8): pp. 1–8 (cit. on p. 10).

47. Ubbelohde, Niels, Frank Hohls, Vyacheslavs Kashcheyevs, Timo Wagner, Lukas Fricke, Bernd Kästner, Klaus Pierz, Hans W. Schumacher, and Rolf J. Haug: 'Partitioning of on-demand electron pairs'. *Nature Nanotechnology* (2015), vol. 10(1): pp. 46–49 (cit. on p. 10).

48. Feve, G, A Mahe, J.-M. Berroir, T Kontos, B Placais, D C Glattli, A Cavanna, B Etienne, and Y Jin: 'An On-Demand Coherent Single-Electron Source'. *Science* (May 2007), vol. 316(5828): pp. 1169–1172. URL: http://www.sciencemag.org/cgi/doi/10.1126/science.1141243 (cit. on pp. 10, 11).

49. Büttiker, M, H Thomas, and A Prêtre: 'Mesoscopic capacitors'. *Physics Letters A* (Sept. 1993), vol. 180(4-5): pp. 364–369. URL: https://linkinghub.elsevier.com/retrieve/pii/0375960193911939 (cit. on p. 10).

50. Bocquillon, E., F. D. Parmentier, C. Grenier, J.-M. Berroir, P. Degiovanni, D. C. Glattli, B. Plaçais, A. Cavanna, Y. Jin, and G. Fève: 'Electron Quantum Optics: Partitioning Electrons One by One'. *Physical Review Letters* (May 2012), vol. 108(19): p. 196803. URL: https://link.aps.org/doi/10.1103/PhysRevLett.108.196803 (cit. on p. 10).

51. Lima, M. M. de, F. Alsina, W. Seidel, and P. V. Santos: 'Focusing of surface-acoustic-wave fields on (100) GaAs surfaces'. *Journal of Applied Physics* (2003), vol. 94(12): p. 7848. URL: http://scitation.aip.org/content/aip/journal/jap/94/12/10.1063/1.1625419 (cit. on p. 11).

52. Bäuerle, Christopher, D Christian Glattli, Tristan Meunier, Fabien Portier, Patrice Roche, Preden Roulleau, Shintaro Takada, and Xavier Waintal: 'Coherent control of single electrons: a review of current progress'. *Reports on Progress in Physics* (May 2018), vol. 81(5): p. 056503. URL: https://iopscience.iop.org/article/10.1088/1361-6633/aaa98a (cit. on pp. 12, 17–19, 22, 111).

53. Shilton, J. M., V. I. Talyanskii, M. Pepper, D. A. Ritchie, J. E.F. Frost, C. J.B. Ford, C. G. Smith, and G. A.C. Jones: 'High-frequency single-electron transport in a quasi-one-dimensional GaAs channel induced by surface acoustic waves'. *Journal of Physics Condensed Matter* (1996), vol. 8(38) (cit. on p. 12).

54. Talyanskii, V. I., J. M. Shilton, M. Pepper, C. G. Smith, C. J. B. Ford, E. H. Linfield, D. A. Ritchie, and G. A. C. Jones: 'Single-electron transport in a one-dimensional channel by high-frequency surface acoustic waves'. *Physical Review B* (Dec. 1997), vol. 56(23): pp. 15180–15184. URL: https://link.aps.org/doi/10.1103/PhysRevB.56.15180 (cit. on p. 12).

55. Hermelin, Sylvain, Shintaro Takada, Michihisa Yamamoto, Seigo Tarucha, Andreas D. Wieck, Laurent Saminadayar, Christopher Bäuerle, and Tristan Meunier: 'Electrons surfing on a sound wave as a platform for quantum optics with flying electrons'. *Nature* (2011), vol. 477(7365): pp. 435–438 (cit. on p. 12).

56. McNeil, R. P.G., M. Kataoka, C. J.B. Ford, C. H.W. Barnes, D. Anderson, G. A.C. Jones, I. Farrer, and D. A. Ritchie: 'On-demand single-electron transfer between distant quantum dots'. *Nature* (2011), vol. 477(7365): pp. 439–442. URL: http://dx.doi.org/10.1038/nature10444 (cit. on p. 12).

57. Takada, Shintaro et al.: 'Sound-driven single-electron transfer in a circuit of coupled quantum rails'. *Nature Communications* (Dec. 2019), vol. 10(1): p. 4557. URL: http://www.nature.com/articles/s41467-019-12514-w (cit. on p. 12).

58. Bertrand, B., S. Hermelin, S. Takada, M. Yamamoto, S. Tarucha, A. Ludwig, A. D. Wieck, C. Bäuerle, and T. Meunier: 'Fast spin information transfer between distant quantum dots using individual electrons'. *Nature Nanotechnology* (Aug. 2016), vol. 11(8): pp. 672–676. URL: http://www.nature.com/articles/nnano.2016.82 (cit. on p. 12).

59. Jadot, Baptiste: 'Coherent long-range transport of entangled electron spin'. PhD thesis. Université Grenoble Alpes, 2020 (cit. on p. 12).

60. Bertrand, Benoit: 'Transport d'information de spin à l'échelle de l'électron unique'. PhD thesis. Université Grenoble Alpes, 2015. URL: https://tel.archives-ouvertes.fr/tel-01212493 (cit. on p. 12).

61. Levitov, Leonid S, Hyunwoo Lee, and Gordey B Lesovik: 'Electron counting statistics and coherent states of electric current'. *Journal of Mathematical Physics* (Oct. 1996), vol. 37(10): pp. 4845–4866. URL: http://aip.scitation.org/doi/10.1063/1.531672 (cit. on pp. 13, 83).

62. Ivanov, D, H Lee, and L Levitov: 'Coherent states of alternating current'. *Physical Review B - Condensed Matter and Materials Physics* (1997), vol. 56(11): pp. 6839–6850 (cit. on pp. 13, 83).

63. Keeling, J, I Klich, and L S Levitov: 'Minimal Excitation States of Electrons in One-Dimensional Wires'. *Physical Review Letters* (Sept. 2006), vol. 97(11): p. 116403. URL: https://link.aps.org/doi/10.1103/PhysRevLett.97.116403 (cit. on pp. 13, 15, 83).

64. Gaury, Benoit and Xavier Waintal: 'Dynamical control of interference using voltage pulses in the quantum regime'. *Nature Communications* (2014), vol. 5(May): pp. 1–8. URL: http://dx.doi.org/10.1038/ncomms4844 (cit. on pp. 13, 23, 108).

65. Roussel, Benjamin: 'Autopsy of a quantum electrical current'. PhD thesis. Université de Lyon, 2017. URL: https://tel.archives-ouvertes.fr/tel-01730943 (cit. on p. 13).

66. Dubois, J, T Jullien, F Portier, P Roche, A Cavanna, Y Jin, W Wegscheider, P Roulleau, and D C Glattli: 'Minimal-excitation states for electron quantum optics using levitons'. *Nature* (2013), vol. 502(7473): pp. 659–663 (cit. on pp. 13–16, 83).

67. Moskalets, M and M Büttiker: 'Floquet scattering theory of quantum pumps'. *Physical Review B* (Nov. 2002), vol. 66(20): p. 205320. URL: https://link.aps.org/doi/10.1103/PhysRevB.66.205320 (cit. on p. 14).

68. Glattli, D. Christian and Preden S. Roulleau: 'Levitons for electron quantum optics'. *Physica Status Solidi (B) Basic Research* (2017), vol. 254(3): pp. 1–11 (cit. on p. 14).

69. Dubois, J, T Jullien, C Grenier, P Degiovanni, P Roulleau, and D C Glattli: 'Integer and fractional charge Lorentzian voltage pulses analyzed in the framework of photon-assisted shot noise'. *Physical Review B - Condensed Matter and Materials Physics* (Aug. 2013), vol. 88(8): p. 085301. URL: https://link.aps.org/doi/10.1103/PhysRevB.88.085301 (cit. on p. 15).

70. Bisognin, R., A. Marguerite, B. Roussel, M. Kumar, C. Cabart, C. Chapdelaine, A. Mohammad-Djafari, J.-M. Berroir, E. Bocquillon, B. Plaçais, A. Cavanna, U. Gennser, Y. Jin, P. Degiovanni, and G. Fève: 'Quantum tomography of electrical currents'. *Nature Communications* (2019), vol. 10(1): p. 3379. URL: http://www.nature.com/articles/s41467-019-11369-5 (cit. on p. 15).

71. Schumacher, Benjamin: 'Quantum coding'. *Physical Review A* (1995), vol. 51(4): pp. 2738–2747 (cit. on p. 16).

72. Ionicioiu, Radu, Gehan Amaratunga, and Florin Udrea: 'Quantum computation with ballistic electrons'. *International Journal of Modern Physics B* (2001), vol. 15(2): pp. 125–133 (cit. on pp. 16, 17, 19).

73. Tsukada, N., A. D. Wieck, and K. Ploog: 'Proposal of novel electron wave coupled devices'. *Applied Physics Letters* (1990), vol. 56(25): pp. 2527–2529 (cit. on p. 17).

74. Eugster, Cristopher C., Jesús A. Del Alamo, Michael J. Rooks, and Michael R. Melloch: 'Split-gate dual-electron waveguide device'. *Applied Physics Letters* (1992), vol. 60(5): pp. 642–644 (cit. on p. 17).

75. Xu, Guangzhao, Min Yang, and Ping Jiang: 'A theoretical investigation on the quantum field effect directional coupler'. *Journal of Applied Physics* (1993), vol. 74(11): pp. 6747–6753 (cit. on p. 17).

76. Eugster, C. C., J. A. Del Alamo, M. J. Rooks, and M. R. Melloch: 'One-dimensional to one-dimensional tunnelling between electron waveguides'. *Applied Physics Letters* (1994), vol. 64(23): pp. 3157–3159 (cit. on p. 17).

77. Tsukada, N., M. Gotoda, and M. Nunoshita: 'Nonlinear electron-wave directional coupler'. *Physical Review B - Condensed Matter and Materials Physics* (1996), vol. 53(12): R7603–R7606 (cit. on p. 17).

78. Bautze, Tobias, Christoph Süssmeier, Shintaro Takada, Christoph Groth, Tristan Meunier, Michihisa Yamamoto, Seigo Tarucha, Xavier Waintal, and Christopher Bäuerle: 'Theoretical, numerical, and experimental study of a flying qubit electronic interferometer'. *Physical Review B - Condensed Matter and Materials Physics* (2014), vol. 89(12): pp. 1–9 (cit. on pp. 17, 18).

79. Rossignol, Benoît, Thomas Kloss, Pacôme Armagnat, and Xavier Waintal: 'Toward flying qubit spectroscopy'. *Physical Review B* (2018), vol. 98(20): pp. 1–5 (cit. on pp. 17, 18, 43, 113).

80. Bertoni, A., P. Bordone, R. Brunetti, C. Jacoboni, and S. Reggiani: 'Quantum logic gates based on coherent electron transport in quantum wires'. *Physical Review Letters* (2000), vol. 84(25): pp. 5912–5915 (cit. on pp. 18, 19).

81. Gaury, Benoit, Joseph Weston, Matthieu Santin, Manuel Houzet, Christoph Groth, and Xavier Waintal: 'Numerical simulations of time-resolved quantum electronics'. *Physics Reports* (2014), vol. 534(1): pp. 1–37. URL: http://dx.doi.org/10.1016/j.physrep.2013.09.001 (cit. on pp. 18, 108).

82. Barenco, A., C.H. Bennett, R. Cleve, D.P. DiVincenzo, N. Margolus, P.W. Shor, T. Sleator, J.A. Smolin, and H. Weinfurter: 'Elementary gates for quantum information'. *Phys. Rev. A* (1995), vol. 52(5): pp. 3457–3467 (cit. on p. 19).

83. Takada, S., C. Bäuerle, M. Yamamoto, K. Watanabe, S. Hermelin, T. Meunier, A. Alex, A. Weichselbaum, J. Von Delft, A. Ludwig, A. D. Wieck, and S. Tarucha: 'Transmission phase in the Kondo regime revealed in a two-path interferometer'. *Physical Review Letters* (2014), vol. 113(12): pp. 18–21 (cit. on p. 20).

84. Edlbauer, Hermann, Shintaro Takada, Grégoire Roussely, Michihisa Yamamoto, Seigo Tarucha, Arne Ludwig, Andreas D. Wieck, Tristan Meunier, and Christopher Baüerle: 'Non-universal transmission phase behaviour of a large quantum dot'. *Nature Communications* (2017), vol. 8(1): pp. 1–7. URL: http://dx.doi.org/10.1038/s41467-017-01685-z (cit. on p. 20).

85. Knill, E., R. Laflamme, and G. J. Milburn: 'A scheme for efficient quantum computation with linear optics'. *Nature* (2001), vol. 409(6816): pp. 46–52 (cit. on p. 21).

86. Potanina, Elina and Christian Flindt: 'Electron waiting times of a periodically driven single-electron turnstile'. *Physical Review B* (2017), vol. 96(4) (cit. on p. 21).

87. Burset, Pablo, Janne Kotilahti, Michael Moskalets, and Christian Flindt: 'Time-Domain Spectroscopy of Mesoscopic Conductors Using Voltage Pulses'. *Advanced Quantum Technologies* (2019), vol. 2(3-4): p. 1900014 (cit. on p. 21).

88. Barthel, C, D J Reilly, C M Marcus, M P Hanson, and A C Gossard: 'Rapid Single-Shot Measurement of a Singlet-Triplet Qubit'. *Phys. Rev. Lett.* (Oct. 2009), vol. 103(16): p. 160503. URL: http://link.aps.org/doi/10.1103/PhysRevLett.103.160503 (cit. on p. 21).

89. Dial, O E, M D Shulman, S P Harvey, H Bluhm, V Umansky, and A Yacoby: 'Charge Noise Spectroscopy Using Coherent Exchange Oscillations in a Singlet-Triplet Qubit'. *Phys. Rev. Lett.* (Apr. 2013), vol. 110(14): p. 146804. URL: http://link.aps.org/doi/10.1103/PhysRevLett.110.146804 (cit. on p. 21).

90. Thalineau, Romain, Andreas D Wieck, C. Bäuerle, and Tristan Meunier: 'Using a two-electron spin qubit to detect electrons flying above the Fermi sea'. *Arxiv* (2014), vol. 1: p. 1403.7770. URL: http://arxiv.org/abs/1403.7770 (cit. on pp. 21, 22).

91. Hanson, R, L P Kouwenhoven, J R Petta, S Tarucha, and L M K Vandersypen: 'Spins in few-electron quantum dots'. *Rev. Mod. Phys.* (Nov. 2007), vol. 79: p. 1455. URL: https://journals.aps.org/rmp/abstract/10.1103/RevModPhys.79.1217 (cit. on p. 21).

92. Thiney, Vivien: 'Detection of travelling electrons in the Quantum Hall effect regime with a singlet-triplet quantum bit detector'. PhD thesis. Université Grenoble Alpes, 2017. URL: https://tel.archives-ouvertes.fr/tel-01757271 (cit. on p. 22).

93. Auslaender, O. M., A. Yacoby, R. De Picciotto, K. W. Baldwin, L. N. Pfeiffer, and K. W. West: 'Tunneling spectroscopy of the elementary excitations in a one-dimensional wire'. *Science* (2002), vol. 295(5556): pp. 825–828 (cit. on pp. 23, 81).

94. Carpentier, D., C. Peça, and L. Balents: 'Momentum-resolved tunneling between Luttinger liquids'. *Physical Review B - Condensed Matter and Materials Physics* (2002), vol. 66(15): pp. 1–4 (cit. on p. 24).

95. Zulicke, U.: 'Ultrasmall Wires Get Excited'. *Science* (Feb. 2002), vol. 295(5556): pp. 810–811. URL: http://www.sciencemag.org/cgi/doi/10.1126/science.1069031 (cit. on p. 24).

96. Auslaender, Ophir M, Hadar Steinberg, Amir Yacoby, Yaroslav Tserkovnyak, Bertrand I Halperin, Rafael De Picciotto, Kirk W Baldwin, Loren N Pfeiffer, and Ken W West: 'Many-body dispersions in interacting ballistic quantum wires'. *Solid State Communications* (2004), vol. 131(9-10 SPEC. ISS.): pp. 657–663 (cit. on p. 25).

97. Auslaender, O M, H Steinberg, A Yacoby, Y Tserkovnyak, B I Halperin, K W Baldwin, L N Pfeiffer, and K W West: 'Spin-charge separation and localization in one dimension'. *Science* (2005), vol. 308(5718): pp. 88–92 (cit. on pp. 25, 27, 81).

98. Zhitenev, N B, R J Haug, K. V. Klitzing, and K Eberl: 'Time-resolved measurements of transport in edge channels'. *Physical Review Letters* (Oct. 1993), vol. 71(14): pp. 2292–2295. URL: https://link.aps.org/doi/10.1103/PhysRevLett.71.2292 (cit. on p. 25).

99. Ernst, G., R. J. Haug, J. Kuhl, K. Von Klitzing, and K. Eberl: 'Acoustic edge modes of the degenerate two-dimensional electron gas studied by time-resolved magnetotransport measurements'. *Physical Review Letters* (1996), vol. 77(20): pp. 4245–4248 (cit. on p. 25).

100. Sukhodub, G., F. Hohls, and R. J. Haug: 'Observation of an interedge magnetoplasmon mode in a degenerate two-dimensional electron gas'. *Physical Review Letters* (2004), vol. 93(19): pp. 2–5 (cit. on p. 25).

101. Kamata, Hiroshi, Takeshi Ota, and Toshimasa Fujisawa: 'Correlation measurement of time-dependent potentials in a semiconductor quantum point contact'. *Japanese Journal of Applied Physics* (2009), vol. 48 (cit. on p. 25).

102. Kamata, H, T Ota, K Muraki, and T Fujisawa: 'Voltage-controlled group velocity of edge magnetoplasmon in the quantum Hall regime'. *Physical Review B - Condensed Matter and Materials Physics* (2010), vol. 81(8): pp. 1–5 (cit. on pp. 25, 66, 83, 107).

103. Landau, L. D. and E. M. Lifshitz: *Course of theoretical Physics*. Vol. 9. 1981: pp. 1–27 (cit. on p. 26).

104. Deshpande, Vikram V., Marc Bockrath, Leonid I. Glazman, and Amir Yacoby: 'Electron liquids and solids in one dimension'. *Nature* (Mar. 2010), vol. 464(7286): pp. 209–216. URL: http://www.nature.com/articles/nature08918 (cit. on pp. 26, 27, 31, 86).

105. Haldane, F. D M: 'General Relation of Correlation Exponents and Spectral Properties of One-Dimensional Fermi Systems: Application to the Anisotropic S=1/2 Heisenberg Chain'. *Physical Review Letters* (Oct. 1980), vol. 45(16): pp. 1358–1362. URL: https://link.aps.org/doi/10.1103/PhysRevLett.45.1358 (cit. on p. 27).

106. Haldane, F. D.M.: ''Luttinger liquid theory' of one-dimensional quantum fluids. I. Properties of the Luttinger model and their extension to the general 1D interacting spinless fermi gas'. *Journal of physics C: Solid State Physics* (1981), vol. 14(19): pp. 2585–2609 (cit. on p. 27).

107. Delft, Jan von and Herbert Schoeller: 'Bosonization for beginners - refermionization for experts'. *Annalen der Physik* (Nov. 1998), vol. 7(4): pp. 225–305. URL: https://arxiv.org/abs/cond-mat/9805275ro (cit. on p. 27).

108. Giamarchi, Thierry: *Quantum Physics in One Dimension*. Vol. 37. 19. Oxford University Press, Dec. 2003: pp. 5275–5276. URL: http://www.oxfordscholarship.com/view/10.1093/acprof:oso/9780198525004.001.0001/acprof-9780198525004 (cit. on pp. 27, 86).

109. Matveev, K. A. and L. I. Glazman: 'Coulomb blockade of tunneling into a quasi-one-dimensional wire'. *Physical Review Letters* (Feb. 1993), vol. 70(7): pp. 990–993. URL: https://link.aps.org/doi/10.1103/PhysRevLett.70.990 (cit. on pp. 27, 31, 32, 38, 86, 105, 107).

110. Levkivskyi, Ivan P. and Eugene V. Sukhorukov: 'Dephasing in the electronic Mach-Zehnder interferometer at filling factor ν=2'. *Physical Review B - Condensed Matter and Materials Physics* (2008), vol. 78(4): pp. 1–13 (cit. on pp. 27, 82).

111. Hashisaka, M, N Hiyama, T Akiho, K Muraki, and T Fujisawa: 'Waveform measurement of charge- and spin-density wavepackets in a chiral Tomonaga-Luttinger liquid'. *Nature Physics* (2017), vol. 13(6): pp. 559–562 (cit. on pp. 27–30, 100, 123).

112. Bocquillon, E., V. Freulon, J. M. Berroir, P. Degiovanni, B. Plaçais, A. Cavanna, Y. Jin, and G. Fève: 'Separation of neutral and charge modes in one-dimensional chiral edge channels'. *Nature Communications* (2013), vol. 4(May) (cit. on p. 27).

113. Inoue, Hiroyuki, Anna Grivnin, Nissim Ofek, Izhar Neder, Moty Heiblum, Vladimir Umansky, and Diana Mahalu: 'Charge fractionalization in the integer quantum hall effect'. *Physical Review Letters* (2014), vol. 112(16): pp. 1–5 (cit. on p. 27).

114. Neder, Izhar: 'Fractionalization noise in edge channels of integer quantum hall states'. *Physical Review Letters* (2012), vol. 108(18): pp. 1–4 (cit. on p. 27).

115. Freulon, V., A. Marguerite, J. M. Berroir, B. Plaçais, A. Cavanna, Y. Jin, and G. Fève: 'Hong-Ou-Mandel experiment for temporal investigation of single-electron fractionalization'. *Nature Communications* (2015), vol. 6 (cit. on pp. 27, 28).

116. Matveev, K A and L I Glazman: 'Conductance and Coulomb blockade in a multi-mode quantum wire'. *Physica B: Physics of Condensed Matter* (1993), vol. 189(1-4): pp. 266–274 (cit. on pp. 32, 36, 86).

117. Coleman, Piers: *Introduction to Many-Body Physics*. 2015 (cit. on pp. 34, 79, 107).

118. Salinas, Silvio R. A.: *Introduction to Statistical Physics*. Graduate Texts in Contemporary Physics. New York, NY: Springer New York, 2001. URL: http://link.springer.com/10.1007/978-1-4757-3508-6 (cit. on p. 34).

119. Kloss, Thomas, Joseph Weston, and Xavier Waintal: 'Transient and Sharvin resistances of Luttinger liquids'. *Physical Review B* (2018), vol. 97(16) (cit. on pp. 34, 107).

120. Roussely, G., E. Arrighi, G. Georgiou, S. Takada, M. Schalk, M. Urdampilleta, A. Ludwig, A.D. Wieck, P. Armagnat, T. Kloss, X. Waintal, T. Meunier, and C. Bäuerle: 'Unveiling the bosonic nature of an ultrashort few-electron pulse'. *Nature Communications* (2018), vol. 9(1). URL: https://www.nature.com/articles/s41467-018-05203-7 (cit. on pp. 38, 39, 67, 78).

121. Pobell, Frank: *Matter and Methods at Low Temperatures*. Berlin, Heidelberg: Springer Berlin Heidelberg, 2007: pp. 1–6. URL: http://link.springer.com/10.1007/978-3-540-46360-3_1 (cit. on p. 41).

122. Wolff, Ingo: *Coplanar Microwave Integrated Circuits*. 2006: pp. 1–545 (cit. on p. 44).

123. Roussely, Gregoire: 'Time resolved measurements in a mesoscopic conductor'. PhD thesis. Université Grenoble Alpes, 2016. URL: https://tel.archives-ouvertes.fr/tel-01453263 (cit. on pp. 46, 48, 49, 51, 54, 65, 115).

124. Corporation, ROGERS: *RO3000®Series Circuit Materials*. URL: https://rogerscorp.com/en/advanced-connectivity-solutions/ro3000-series-laminates/ro3010-laminates (visited on 10/19/2019) (cit. on pp. 46, 53).

125. Mandal, Soumen, Tobias Bautze, Rémi Blinder, Tristan Meunier, Laurent Saminadayar, and Christopher Bäuerle: 'Efficient radio frequency filters for space constrained cryogenic setups'. *Review of Scientific Instruments* (Feb. 2011), vol. 82(2): p. 24704. URL: http://aip.scitation.org/doi/10.1063/1.3543736 (cit. on p. 48).

126. Dubois, Julie: 'Vers une source mésoscopique à n-électrons basée sur des pulses de tensions Lorentziens'. PhD thesis. Université Pierre et Marie Curie, 2013. URL: https://tel.archives-ouvertes.fr/tel-00828608 (cit. on p. 51).

127. Krautenbac, J.: *Technical Data SMA*. 2019. URL: https://www.rosenberger.com/0_documents/de/specs/com/32-000-000_TD.pdf (visited on 12/12/2019) (cit. on p. 51).

128. Johnson, J B: 'Thermal Agitation of Electricity in Conductors'. *Physical Review* (July 1928), vol. 32(1): pp. 97–109. URL: https://link.aps.org/doi/10.1103/PhysRev.32.97 (cit. on p. 51).

129. Nyquist, H: 'Thermal Agitation of Electric Charge in Conductors'. *Physical Review* (July 1928), vol. 32(1): pp. 110–113. URL: https://link.aps.org/doi/10.1103/PhysRev.32.110 (cit. on p. 51).

130. Rosenberger: *Mini-SMP*. URL: https://www.rosenberger.com/us_en/pdf/products/rf_coax_connectors/Mini-SMP.pdf (visited on 12/12/2019) (cit. on p. 52).

131. Jullien, Thibaut: 'Mesoscopic few-electron voltage pulse source'. (2014), vol. URL: https://tel.archives-ouvertes.fr/tel-01158785 (cit. on p. 56).

132. *RC Differentiator*. URL: https://www.electronics-tutorials.ws/rc/rc-differentiator.html (visited on 09/24/2019) (cit. on p. 63).

133. Datta, Supriyo: 'Electrical resistance: An atomistic view'. *Nanotechnology* (2004), vol. 15(7) (cit. on p. 63).

134. Wu, Jingbo, Alexander S Mayorov, Christopher D Wood, Divyang Mistry, Lianhe Li, Wilson Muchenje, Mark C Rosamond, Li Chen, Edmund H Linfield, A Giles Davies, and John E Cunningham: 'Excitation, detection and electrostatic manipulation of terahertz-frequency range plasmons in a two-dimensional electron system'. *Scientific Reports* (Dec. 2015), vol. 5(1): p. 15420. URL: http://www.nature.com/articles/srep15420 (cit. on pp. 71, 73).

135. Chaplik, A.V.: 'Absorption and emission of electromagnetic waves by two-dimensional plasmons'. *Surface Science Reports* (Dec. 1985), vol. 5(7): pp. 289–335. URL: https://linkinghub.elsevier.com/retrieve/pii/016757298590010X (cit. on p. 73).

136. Houten, H. van, B. J. van Wees, J. E. Mooij, C. W. J Beenakker, J. G. Williamson, and C. T. Foxon: 'Coherent Electron Focussing in a Two-Dimensional Electron Gas'. *Europhysics Letters (EPL)* (Apr. 1988), vol. 5(8): pp. 721–725. URL: http://stacks.iop.org/0295-5075/5/i=8/a=010?key=crossref.fac7654e205bdff277a333fa175bf4e9 (cit. on p. 81).

137. Mast, D. B., A. J. Dahm, and A. L. Fetter: 'Observation of Bulk and Edge Magnetoplasmons in a Two-Dimensional Electron Fluid'. *Physical Review Letters* (Apr. 1985), vol. 54(15): pp. 1706–1709. URL: https://link.aps.org/doi/10.1103/PhysRevLett.54.1706 (cit. on p. 82).

138. Glattli, D C, E Y Andrei, G Deville, J Poitrenaud, and F. I.B. Williams: 'Dynamical hall effect in a two-dimensional classical plasma'. *Physical Review Letters* (Apr. 1985), vol. 54(15): pp. 1710–1713. URL: https://link.aps.org/doi/10.1103/PhysRevLett.54.1710 (cit. on p. 82).

139. Ashoori, R. C., H. L. Stormer, L N Pfeiffer, K W Baldwin, and K West: 'Edge magnetoplasmons in the time domain'. *Physical Review B* (Feb. 1992), vol. 45(7): pp. 3894–3897. URL: https://link.aps.org/doi/10.1103/PhysRevB.45.3894 (cit. on p. 82).

140. Neder, I., M. Heiblum, Y. Levinson, D. Mahalu, and V. Umansky: 'Unexpected behavior in a two-path electron interferometer'. *Physical Review Letters* (2006), vol. 96(1): pp. 1–4 (cit. on p. 82).

141. Roulleau, Preden, F. Portier, D. C. Glattli, P. Roche, A. Cavanna, G. Faini, U. Gennser, and D. Mailly: 'Finite bias visibility of the electronic Mach-Zehnder interferometer'. *Physical Review B - Condensed Matter and Materials Physics* (2007), vol. 76(16): pp. 2–5 (cit. on p. 82).

142. Berg, E., Y. Oreg, E. A. Kim, and F. Von Oppen: 'Fractional charges on an integer quantum hall edge'. *Physical Review Letters* (2009), vol. 102(23): pp. 1–4 (cit. on p. 82).

143. Hashisaka, Masayuki, Hiroshi Kamata, Norio Kumada, Kazuhisa Washio, Ryuji Murata, Koji Muraki, and Toshimasa Fujisawa: 'Distributed-element circuit model of edge magnetoplasmon transport'. *Physical Review B - Condensed Matter and Materials Physics* (2013), vol. 88(23): pp. 1–12 (cit. on p. 83).

144. Kamata, H., N. Kumada, M. Hashisaka, K. Muraki, and T. Fujisawa: 'Fractionalized wave packets from an artificial Tomonaga–Luttinger liquid'. *Nature Nanotechnology* (Mar. 2014), vol. 9(3): pp. 177–181. URL: http://www.nature.com/articles/nnano.2013.312 (cit. on pp. 83, 123).

145. Groth, Christoph W., Michael Wimmer, Anton R. Akhmerov, and Xavier Waintal: 'Kwant: A software package for quantum transport'. *New Journal of Physics* (2014), vol. 16: pp. 1–40 (cit. on pp. 85, 108).

146. Freulon, V., A. Marguerite, J. M. Berroir, B. Plaçais, A. Cavanna, Y. Jin, and G. Fève: 'Hong-Ou-Mandel experiment for temporal investigation of single-electron fractionalization'. *Nature Communications* (2015), vol. 6 (cit. on p. 100).

147. Brasseur, Paul, Ngoc Han Tu, Yoshiaki Sekine, Koji Muraki, Masayuki Hashisaka, Toshimasa Fujisawa, and Norio Kumada: 'Charge fractionalization in artificial Tomonaga-Luttinger liquids with controlled interaction strength'. (2017), vol. 081101: pp. 1–4 (cit. on p. 123).

List of Figures

List of Tables

Acknowledgments

First of all, I would like to express my gratitude to my PhD advisor Christopher Bäuerle. Thank you for sharing your expertise in different subjects such as physics, cryogenics, cabling, skiing, among others. Since the beginning of my PhD, you have supported me, and this support has pushed me to overcome several challenges.

I am also very grateful to all the special people that I have met over the past three years. Among all these people, I must first mention Greg, who had fabricated the nice sample that gave me many results, and who guided me at the beginning of the experiment, even if it was for a short period. I must also mention Shintaro Takada, for the enlightening discussions and the advices about coding. I also have to mention Mathias Solana, who has taught me a lot about the french language and culture. I would like to thank Giorgos Georgiou for several fruitful discussions on physics and for sharing with me a bit of his expertise in nanofabrication. I would also like to thank Xavier Waintal and Pacôme Armagnat for the interesting meetings.

Un grand merci également à toutes les personnes du groupe pour la bonne ambiance. En spécial à: Pierre-André Mortemousque pour être là tôt le matin pour prendre un café et avec qui j'ai beaucoup appris; Matias Urdampilleta pour tous les échange sur la physique autour d'un verre et aussi pour motiver les gens à faire du sport; un merci aussi aux partenaires pour boire un verre et aussi pour le soutien émotionnel: Baptiste Jadot, Emmanuel Chanrion. Merci à tous du groupe pour le riche échange culturel et aussi sur la physique: Junliang Wang, David Niegemann, Bernhard Klemt, Cameron Spence, Hermann Edlbauer, Martin Nurizzo, Clément Geffroy, Vivien Thiney, Candice Thomas et Tristan Meunier. Les ensemble des expériences présentées dans ce manuscrit n'auraient jamais eu lieu sans le soutien technique dont on peut bénéficier à l'Institut Néel. Merci à Pierre Perrier pour tout le soutien avec la cryo et pour nombreux coups de main, merci aux membres du liquef Johan, Raphaël et Kevin pour m'avoir fournir 250 L d'hélium à chaque 5 jours sans faute pendant des années. Un grand merci à Christophe Guttin, Daniel Lepoittevin pour le soutien sur l'électronique, merci à l'équipe de nanofab: Bruno, Latifa, Gwénaëlle, Jeff et Thierry. Merci à l'équipe administrative, Florence, Otmane, Angélique, pour tout le soutien avec la paperasse et merci à Cécile qui m'avait appris sur les techniques de présentation et m'a également fait l'impression de ce manuscrit.

I must thank the people that have become my family in Grenoble: Jhonathas, Fernanda, Jêrome, Gabi, Alvaro, Eduardo, Evelina, Rahel, Charles. I also need to thank my family in Brazil, which I have not seen much during these years, but they were always present

to give me emotional support. Finally, I would like to thank my wife Gabriela for all the support she had given me over the years, especially when I decided to do a PhD abroad.